



Chair of Mining Engineering and Mineral Economics

Doctoral Thesis

Simulation of dynamic fracturing in rock  
like materials - Fines creation from  
branching-merging of blast loaded cracks  
in general and in cylindrical specimens

Armin Iravani, MSc.

January 2020

**AFFIDAVIT**

I declare on oath that I wrote this thesis independently, did not use other than the specified sources and aids, and did not otherwise use any unauthorized aids.

I declare that I have read, understood, and complied with the guidelines of the senate of the Montanuniversität Leoben for "Good Scientific Practice".

Furthermore, I declare that the electronic and printed version of the submitted thesis are identical, both, formally and with regard to content.

Date 07.01.2020



Signature Author  
Armin, Iravani



---

## Acknowledgements

This work has been financially supported by Austrian Science Fund (FWF): project P27594-N29 and Montanuniversität Leoben. We acknowledge the Vienna Scientific Cluster (VSC) for the provided computational resources. We also acknowledge the Project HPC-EUROPA3 (Grant No. INFRAIA-2016-1-730897), with the support of the European Community - Research Innovation Action under the H2020 program. In particular, we gratefully acknowledge the support of the CSC-IT Center for Science for the computer resources and technical support provided during the three months period of the HPC-EUROPA3 scholarship.

I am thankful to Dr. Peter Moser, head of the chair of Mining Engineering and Mineral Economics of Montanuniversität Leoben, who have provided me with an excellent academic time at this chair to pursue my career goals.

I would like to thank my mentor, Dr. Finn Ouchterlony, for all the conversations that we have had, both personal and professional. It has been a priceless experience for me to educate and grow up beside you. He has taught me scientific research, manner, patience, supportiveness, importance of empathy and also life in general, by his example. Having you as my mentor was accompanied with feelings of confidence.

I would like to thank Dr. Thomas Antretter, head of Institute of Mechanics of Montanuniversität Leoben, who have given me guidance and encouragement during the course of my PhD study. Especially your help at the beginning of my PhD study made this research progress in a successful way. I would like to thank you for providing me the admission to use the HPC server of the Institute of Mechanics.

I would like to thank Dr. Jan Åström. The experience that I had when working with you at CSC-IT Center for Science remains with me because it was one of a kind. Conversations with you all the time gave me eagerness and motivation for science. Clearly, this thesis could not have been so fruitful without your contributions and your generous and smart character. I would like to thank you for your support during my last 2 years of my PhD study.

I would also like to thank Ivan Kukulj, my colleague during this PhD study for our four years of cooperation.

Finally, I would like to thank my family and my dear friends especially Zahra and Firoze who have been a great support and also for the charming moments we have spent together.



---

## Abstract

Fine-fragments (or fines) are an unavoidable result of rock blasting and the subsequent comminution process. They are often less valuable than larger fragments or even unsellable and hence have economic and environmental impacts. Thus, understanding the source mechanisms forming the fines has high industrial and research interest.

Two mechanisms are responsible for the creation of the fines: compressive crushing-shearing and branching-merging of tensile cracks. In this work the focus is put on numerical modeling of blast-induced fragmentation and its mathematical formulation in order to investigate the role of branching-merging in blasting fragmentation and fines generation.

In the first part, two numerical methods, i.e. finite element method (FEM), Abaqus/Explicit, and discrete element method, HiDEM code, are used for simulating quasi-brittle material response to civil blast loads. The dynamic crack propagation, branching-merging and the resultant mass passing fraction (MPF) in lab-scale cylindrical specimens are analyzed. The 2D FEM simulations produce reasonable post-mortem end-face fracture patterns, while the HiDEM simulations produce 3D crack networks and MPF curves similar to experimental results.

The second part deals with 3D HiDEM modeling of lab-scale cylinders of magnetite mortar ( $\varnothing 140 \text{ mm} \times 280 \text{ mm}$ ). The computed Fragment Size Distributions (FSDs) in an s-n(s) description of fragmentation are compared with those of the experiments which are confined by a cylindrical layer of pre-stressed aggregate. An FSD function with three terms is proposed. Both the experimental and the numerical FSDs are composed of the three parts, i.e. fine-fragments, intermediate size fragments, each described by a separate fragmentation mechanism and ditto power-law exponent, and boulders. Here, the fines arise as a result of the crushing-shearing mechanism. The branching-mergings of tensile cracks are responsible for the creation of the intermediate size fragments. Major tensile cracks delineate the boulders.

Furthermore, the spatial location of the fines with respect to a blast-hole is studied using the HiDEM code. The absolute mass of the fines is calculated as a function of their distance to the blast-hole. The HiDEM results supported by experiments show that the major amount of fines is not created at or around the blast-hole as the Crush Zone Model assumes.

In the third part, 24 FSDs from controlled blasting tests, which were either unconfined or confined by momentum traps are reported. High-resolution HiDEM

---

simulations of a pressurized crack propagating in a heterogeneous brittle medium are performed, and the FSDs are computed. The pressurized crack is subjected to different external lateral stresses in tension and compression to mimic different scenarios that may arise in blasting tests. In the simulations, the power-law exponent of the size distribution in the fines region depends on the external stress states. That means, the fines power-law exponent at high compressive lateral stresses has a crushing-shearing origin of fragmentation, while at low compressive or tensile lateral stresses the exponent has a branching-merging origin of fragmentation. In the tests, the FSDs consist of two branching-merging terms in the fines and intermediate size fragments regions, and a boulders term, i.e. the previous crushing-shearing mechanism acting in the fines region is replaced by a second branching-merging one.

In conclusion, the main mechanism forming the fines is a function of external stresses or confinement conditions. At high external compressive stresses the majority of fines are formed by compressive crushing-shearing. The branching-merging, on the other hand, is the main mechanism at tensile and low compressive external stresses.

---

## Zusammenfassung

Feinstpartikel sind ein unvermeidbares Resultat des Spreng- sowie des nachfolgenden Zerkleinerungsprozesses. Meist erzielen sie aber einen geringeren Marktpreis oder sind sogar unverkäuflich und erzeugen daher wirtschaftliche und ökologische Folgewirkungen. Das Verständnis der Mechanismen, die zu diesen Feinanteilen führen, ist daher von hohem industriellen und wissenschaftlichen Interesse.

Für die Entstehung von Feinmaterial sind im Wesentlichen zwei Mechanismen verantwortlich: Zermahlen bzw. Abscheren unter Druck („crushing-shearing“) sowie das Verzweigen und die Vereinigung („branching-merging“) von Rissen unter Zug. In dieser Arbeit liegt der Schwerpunkt auf der mathematischen Beschreibung sowie der numerischen Modellierung von Fragmentierungsprozessen mit dem Ziel, die Rolle von branching-merging beim sprengtechnischen Zerkleinern und bei der Entstehung von Feinmaterial zu untersuchen.

Im ersten Teil werden zunächst mit der Finite Elemente Methode (FEM) (Abaqus/-Explicit), sowie der Diskreten Elemente Methode (DEM) (HiDEM) zwei numerische Methoden verwendet, um das quasi-spröde Verhalten des Materials beim Sprengen zu untersuchen. Speziell wird dabei die dynamische Rissausbreitung, das branching-merging Verhalten sowie die resultierenden Mass Passing Fraction (MPF) Kurven mit Hilfe von Laborversuchen an zylindrischen Proben analysiert. Die 2D-Simulationen produzieren dabei vernünftige post-mortem Strukturen an den Endflächen, wohingegen die HiDEM Simulationen 3D-Rissnetzwerke und MPF-Kurven produzieren, die den experimentellen Beobachtungen sehr ähnlich sind.

Der zweite Teil handelt von 3D HiDEM Simulationen der Laborversuche an zylindrischen Proben aus Magnetit Beton ( $\varnothing$  140 mm  $\times$  280 mm). Die berechneten und mit Hilfe von s-n(s) Kurven dargestellten Korngrößenverteilungen (KGV) werden mit Daten aus Experimenten verglichen, bei denen die Zylinder von einer vorgespannten Manschette umschlossen waren. Eine KGV-Funktion mit drei Komponenten wird vorgeschlagen. Sowohl experimentelle als auch numerische KGV bestehen aus: Feinmaterial, Übergangsmaterial (beide können mit eigenem Zerkleinerungsmechanismus und zugehörigen Exponenten beschrieben werden), sowie Blöcken. Dabei ist das Feinmaterial eine Folge von crushing-shearing, während das Übergangsmaterial aus branching-merging resultiert. Die größeren Blöcke entstehen nach dem Auftreten großer Zugrisse.

Des Weiteren wird die räumliche Verteilung des Feinmaterials um das Bohrloch mit Hilfe von HiDEM untersucht. Dabei wird die Masse der Feinfraktion als Funktion des Abstandes zum Bohrloch dargestellt. Die Berechnungen sowie die Experimente beweisen, dass der überwiegende Anteil der Feinfraktion nicht in der Nähe



---

des Bohrlochs entsteht (wie es das „Crush Zone Model“ nahelegen würde).

Im dritten Teil werden 24 KGV aus experimentellen Tests analysiert. Hochauflösende HiDEM Simulationen der Rissausbreitung werden in einem heterogenen, spröden Material durchgeführt und deren KGV dargestellt. Die zylindrischen Modelle werden unterschiedlichen externen Umfangsspannungen ausgesetzt, um verschiedene realitätsnahe Umgebungsszenarien nachzustellen. Dabei zeigt sich, dass der Exponent des Potenzgesetzes der KGV für die Feinfraktion von den externen Spannungen abhängt. Das heißt, dass bei hohem lateralen Druck crushing-shearing und bei geringem lateralen Druck oder Zug „branching-merging“ als Ursache identifiziert werden können.

Zusammenfassend kann gesagt werden, dass die Menge an Feinfraktion eine Funktion von externem Druck und den Einschlussbedingungen ist. Bei hohem äußeren Druck entsteht der Hauptanteil des Feinmaterials zufolge von „crushing-shearing“, wohingegen „branching-merging“ die Hauptursache für die Bildung der Feinanteile bei Vorherrschen von Zugspannungen oder geringem Druck darstellt.

# Contents

<b>1</b>	<b>Introduction</b>	<b>1</b>
1.1	Thesis organisation . . . . .	1
1.2	Literature review . . . . .	3
1.2.1	Experiments . . . . .	3
1.2.2	Fragmentation characteristics and prediction equations . . . . .	6
1.2.3	Numerical methods for simulating fracture and fragmentation . . . . .	8
1.3	Motivations and Objectives . . . . .	11
1.4	List of papers and contribution of the author to the papers . . . . .	13
<b>2</b>	<b>Theoretical background</b>	<b>17</b>
2.1	Constitutive theories to describe concrete behavior . . . . .	17
2.1.1	Concrete damage plasticity formulation [1] . . . . .	18
2.2	HiDEM formulation . . . . .	22
<b>3</b>	<b>Essential findings</b>	<b>25</b>
3.1	Paper I . . . . .	25
3.2	Paper II . . . . .	28
3.3	Paper III . . . . .	31
3.4	Paper IV . . . . .	32
3.5	Additional findings . . . . .	34
<b>4</b>	<b>Bibliography</b>	<b>39</b>
<b>5</b>	<b>Paper I:</b> Finite element modeling of blast induced fractures of cylinders of mortar and rock	<b>49</b>
<b>6</b>	<b>Paper II:</b> Origin of fines particle in blasting fragmentation: compressive crushing	<b>63</b>
<b>7</b>	<b>Paper III:</b> Tracing the origin of fines generated in blasting	<b>73</b>

<b>8</b>	<b>Paper IV:</b>	
	Origin of fines particle in blasting fragmentation: unstable tensile crack growth type	<b>85</b>
<b>9</b>	<b>Discussion</b>	<b>99</b>
<b>10</b>	<b>Summary and Conclusions</b>	<b>101</b>
<b>11</b>	<b>Outlook</b>	<b>107</b>
	<b>List of Figures</b>	<b>109</b>
<b>12</b>	<b>Appendices</b>	<b>113</b>
A	Abaqus/Explicit VUSDFLD . . . . .	113
B	Experimental MPFs . . . . .	117
C	Regression analysis . . . . .	125
D	Statistical significance analysis . . . . .	129
E	Fine- and intermediate fragment size range . . . . .	135

## List of symbols and abbreviations

$\alpha$	1) branching-merging power-law exponent 2) a dimensionless material constant in CDP
A	cross sectional areal of beam
A(x)	surface area of fragments generated per unit mass measured by Michaux [2]
b	undulation parameter in Swebrec <sup>©</sup> function
$\beta$	crushing power-law exponent
$\beta(\tilde{\varepsilon}^{pl})$	a function in CDP
$b_t$	attenuation factor
<b>C</b>	damping matrix
$\gamma$	a dimensionless material constant in CDP
C3D8R	three dimensional linear hexahedral stress elements with reduced integration points used in Abaqus/Explicit
CDP	Concrete Damage Plasticity
CIN3D8	three dimensional linear brick infinite elements used in Abaqus/Explicit
CZM	Crush Zone Model
d	damage parameter
$D_0^{el}$	initial undamaged elastic stiffness matrix in CDP
$d_c$	compressive damage parameter in CDP
$D^{el}$	degraded elastic stiffness matrix in CDP
DEM	Discrete Element Method
$d_t$	tensile damage parameter in CDP
$\Delta t$	time step
$\epsilon$	eccentricity in CDP
E	Young's modulus
$\dot{\boldsymbol{\varepsilon}}$	strain rate tensor
$\dot{\boldsymbol{\varepsilon}}^{el}$	elastic strain rate tensor
$\dot{\boldsymbol{\varepsilon}}^{pl}$	plastic strain rate tensor
$\tilde{\varepsilon}^{pl}$	equivalent plastic strain
$\tilde{\varepsilon}_c^{pl}$	compressive equivalent plastic strain
$\tilde{\varepsilon}_t^{pl}$	tensile equivalent plastic strain
$\hat{\boldsymbol{\varepsilon}}^{pl}$	tensor of the eigenvalues of the plastic strain rate tensor
$\hat{\varepsilon}_1, \hat{\varepsilon}_2, \hat{\varepsilon}_3$	eigenvalues of the plastic strain rate tensor
$\dot{\tilde{\varepsilon}}^{pl}$	equivalent plastic strain dot
$\dot{\tilde{\varepsilon}}_c^{pl}$	compressive equivalent plastic strain rate
$\dot{\tilde{\varepsilon}}_t^{pl}$	tensile equivalent plastic strain rate
$E_0$	initial undamaged elastic stiffness in uniaxial loading
$\varepsilon_c$	total compressive strain in uniaxial loading

EFEM	Embedded Finite Element Method
EoS	Equation of State
$\varepsilon_t$	total tensile strain in uniaxial loading
F	yield function in CDP
$f(s/s_1)$	an exponential function that acts on fragments larger than $s_1$
FEM	Finite Element Method
$F_i$	sum of other forces acting on particle $i$
$f_i$	field variable in CDP
FSD	Fragment Size Distribution
FWF	Austrian Science Fund
G	1) flow potential in CDP 2) shear modulus
HiDEM	Helsinki Discrete Element Model code released under GNU GPL V3.0.
HJC	Holmquist-Johnson-Cook constitutive material model
I	moment of inertia of the cross section of a rectangular beam with respect to its either of symmetry axes $x$ or $y$
$I_c$	moment of inertia of the cross section of a rectangular beam with respect to its center point
JH-1	Johanson-Holmquist-1 constitutive material model
JH-2	Johanson-Holmquist-2 constitutive material model
JHB	Johnson-Holmquist-Beissel constitutive material model
<b>K</b>	stiffness matrix
$K_c$	a constant that controls shape of yield function in CDP
KGV	Korngrößenverteilung [in English: Fragment Size Distribution]
$L$	length of beam
$\dot{\lambda}$	a nonnegative plastic multiplier in CDP
<b>M</b>	mass matrix
MM	Magnetite Mortar
MPF	Mass Passing Fraction
MT	Momentum traps
MUL	Montanuniversität Leoben
$\nu$	Poisson's ratio
$n(s)$	number of fragments of size $s$
$N(x)$	cumulative number of fragments retained on sieve in Michaux [2] data
NBC	Natural Breakage Characteristic
NIB	No Identified Boulders
$n_b(s)$	size distribution for boulders
$n_{bm}(s)$	size distribution of the number of fragments of size $s$ formed in a branching-

	merging process
$n_{cr}(s)$	size distribution of the number of fragments of size $s$ formed in a crushing-shearing process
$\bar{p}$	effective hydrostatic pressure
$p(t)$	pressure as a function of time used in FEM and DEM simulations
$p(v)$	pressure as a function of blast-hole volume
$P(x)$	relative mass amount passing in Swebrec <sup>®</sup> function
$p_0$	a constant value to regulate lateral external stresses
$P_{app}$	an internal pressure load applied on the crack flanks
PETN	pentaerythritol tetranitrate
$P_{peak}$	peak pressure
$\psi$	dilation angle
$\bar{q}$	Mises equivalent effective stress
$\rho c$	specific acoustic impedance of host rock
$\rho'c'$	specific acoustic impedance of boundary material
$\ddot{\mathbf{r}}_i, \dot{\mathbf{r}}_i, \mathbf{r}_i$	acceleration, velocity and position vectors of particle $i$
$\mathbf{r}_{ij}$	position vectors for all particles $j$ that are connected to particle $i$
$\bar{\boldsymbol{\sigma}}$	effective stress tensor
$\hat{\boldsymbol{\sigma}}$	a tensor containing the eigenvalues of the effective stress tensor in CDP
$\bar{\mathbf{S}}$	deviatoric part of the effective stress tensor
$\boldsymbol{\sigma}$	Cauchy stress tensor
$\bar{\sigma}_c$	effective compressive cohesion stress
$\hat{\sigma}_i$	principal stresses with $i = 1, 2, 3$
$s$	dimensionless parameter expresses number of DEM particles forming a fragment
$s_1$	size limit of fragment size
$s_b$	characteristic size of boulders
$s_f$	transition size between the fines and the intermediate size fragments
$s_i$	transition size between the intermediate size fragments and the boulders
SPH	Smooth Particle Hydrodynamics
$\sigma_{t0}$	uniaxial tensile stress at failure
$t$	time
$\tau$	a general power-law exponent of size distribution
TCM	Two-Component Model
VOD	Velocity of Detonation
$w_c, w_t$	weight factors controlling the recovery of the tensile and compressive stiffness values in CDP
$x$	1) sieving mesh-size

	2) measure of mesh size or limits of mesh interval (bin width); usually upper or lower limit or arithmetic mean of these in [2]
$x_{50}$	the median fragment size (50% passing size)
$x_d$	distance to blast-hole
XFEM	Extended Finite Element Method
$x_{\max}$	1) largest-possible fragment 2) upper fragment limit in Swebrec <sup>©</sup> function

## Glossary of Terms

blast test	one blasting case with a defined blast setup.
blast set	a series of blast tests where usually one parameter, i.e. load level, confinement, etc., is varying between them
code	computer program in general.
discontinuity	displacement- or strain discontinuity in XFEM or EFEM formulations stands for cracks or failures in the material domain.
fine-fragments	1) small fragments that are usually less valuable. 2) in $s - n(s)$ formulation: the fragments which are forming the first term of the equations.
model	1) a code with defined geometry, material properties and initial and boundary conditions; i.e. code ready to run 2) assembly of elements that define the geometry being studied.
momentum traps	a confinement setup that is designed such that upon transmission of stress waves from the blasted medium into the confinement segments, the segments move away from the blasted medium to avoid reflection of stress waves on the outer boundary.
quasi-brittle material	failure in these materials are caused by brittle fracture rather than plastic yield.
simulation	running the code for a specific model.
stiff confinement	a mantle or an outer boundary condition which confines the volume of interest with a layer of pre-stressed aggregate.
universal exponent of branching-merging	repeatable exponent under different boundary and initial conditions, while the mechanism, i.e. branching-merging, stays the same.



This page intentionally left blank.

# 1 Introduction

## 1.1 Thesis organisation

The thesis starts with a review on experimental research of blast induced fracture and fragmentation. Further in this part, fragmentation characteristics and prediction equations, and the numerical methods suitable for simulating brittle dynamic fracture and fragmentation are reviewed. The motivation section names current fragmentation prediction equations describing the theories on the source of blast-induced fine-fragments followed by the research tasks of the thesis.

The following chapter provides the theoretical backgrounds of the numerical tools that are used in this study. Initially, the theoretical backgrounds of the constitutive theory that is used to describe the behavior of concrete which is implemented in Abaqus/Explicit and then the formulation of the discrete element method (HiDEM code) are provided.

The main part of the thesis is presented as a compilation of a number of peer reviewed research articles which have been completed during the PhD program at the chair of Mining Engineering and Mineral Economics of Montanuniversität Leoben (MUL) and funded by an Austrian Science Fund (FWF) research project: P27594-N29.

The first paper investigates the blast-induced damage and fragmentation of mortar cylinders using two numerical methods: Finite and Discrete Element Methods (FEM and DEM), respectively. They are Abaqus/Explicit coupled with a damage plasticity constitutive material model and the HiDEM discrete element code. Here, the pros and cons of these numerical methods for simulating the blast-induced damage and fragmentation are demonstrated. In FEM a disk and in HiDEM a cylindrical specimen are subjected to a blast load that is applied at their centrally located blast-hole. The FEM results are qualitatively compared with the post-mortem end-face fracture patterns of our own experimental results [3] at three explosive loading levels. Next, in HiDEM the resultant Mass Passing Fraction (MPF) curves are qualitatively compared to those of the experiments and in general with Swebrec<sup>©</sup> function like ones.

The second paper treats the transformation of the MPFs of some lab-scale blasted cylinders of magnetite mortar into the  $s - n(s)$  Fragment Size Distribution (FSD). The  $s - n(s)$  representation simplifies the mathematical description of the whole size range of the FSDs. The  $n(s)$  equation consists of three terms describing in turn

the fine-fragments, the intermediate size ones, and the boulders. The results from HiDEM simulations are reported and compared with the experimental results.

The third paper reviews two well-known theories on the source of fine-fragments, i.e. the Crush Zone Model (CZM) and its development, the star-shape model. HiDEM simulations of the lab-scale cylindrical specimen at three explosive loading levels are carried out. The simulation results are supported by experimental data, and they demonstrate some contradictions in the existing theories concerning the source of fine-fragments.

The fourth paper modifies the fine-fragments region of the  $n(s)$  equation introduced in the second paper to describe the FSDs of a series of blasted cylinders. The experiments were made either unconfined or confined by momentum traps (MT). Twenty eight experimental results which were either obtained at MUL [3] or from the literature are analyzed. High resolution HiDEM simulations of dynamic crack propagation in a brittle medium are made and the resultant FSDs are compared with the experimental results.

## 1.2 Literature review

### 1.2.1 Experiments

Much experimental work has been carried out to enhance the knowledge of the blast induced fracture and fragmentation. Here we summarize the work done by Svahn [4], Michaux [2, 5], Banadaki [6], and Chi [7] among others.

Svahn [4] blasted three cylinders ( $\varnothing$  300 mm  $\times$  600 mm) whose inner material was given three different colors in the radial direction by adding iron oxide pigment to the mortar, i.e.  $\varnothing_{\text{outer}} = 120$  mm, 200 mm and 300 mm for black, yellow and green. The colored layers were concentric and the core black layer was centrally charged, see the inset of Fig. 1.1.

The resultant mass passing distributions gave a whole range of fragment sizes for the core layer with the same general character as those for the outer layers. The results had no tendency either for the core material to consist only of the fine-fragments or for the outer layers to contain no fine-fragments, see Fig. 1.1. All three regions produced a whole range of fragment sizes. The core layer contained even fewer fragments smaller than 2 mm in absolute terms than the other layers together, see Fig. 1.1.

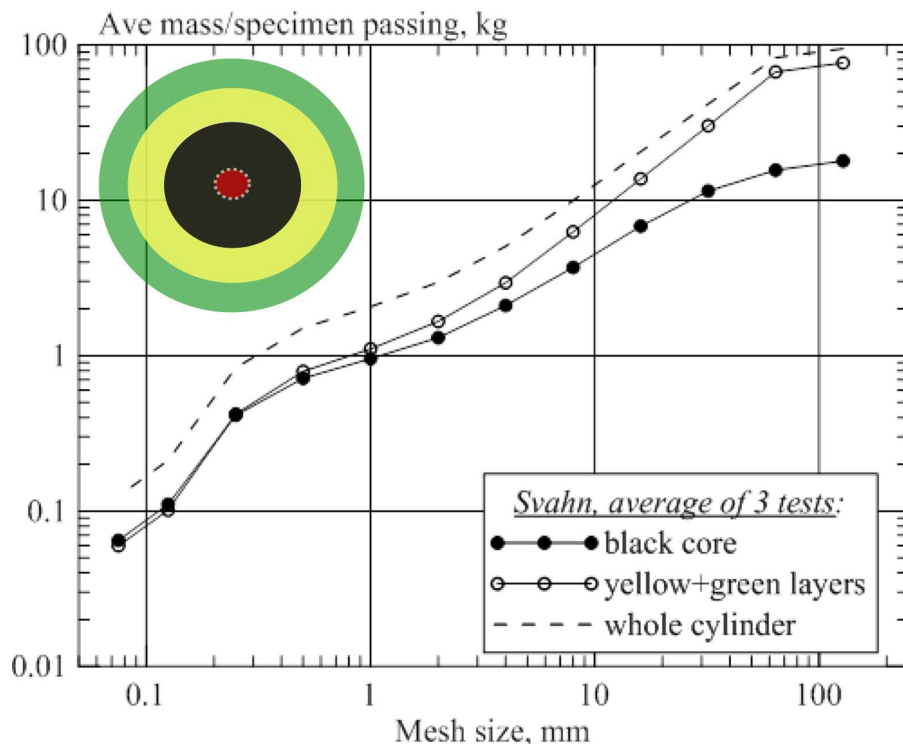


**Figure 1.1:** Average mass passing distribution curves for three blasted cylinders of Svahn [4], comparing black core with the sum of the two outer layers.  $\varnothing_{\text{outer}} = 120$  mm, 200 mm and 300 mm for black, yellow and green. The figure is taken from [8]. The inset of the figure illustrates the multilayered setup of the blasted cylinders.

Michaux [2] blasted 85 unconfined samples of lumps and cylinders. The cylinders were made of grout and the lumps were made of four different rock types: granodiorite, monzonite, phyllite and banded iron ore. Three explosives with different velocity of detonation (VOD) and specific charge were used.

The resulting fragmentation was collected and sieved down to  $38\ \mu\text{m}$ . The  $x$ ,  $y$  and  $z$  dimensions of each fragment were measured manually for fragments larger than  $6.3\ \text{mm}$ . For fragments smaller than  $6.3\ \text{mm}$  down to  $38\ \mu\text{m}$  Michaux used image analysis and a “ $z$  dimension prediction code” to quantify the dimensions. The density, average fragment volume and mass, surface area, and number of fragments in each sieve size fraction were then estimated.

He [2, 5] plotted his data in several ways; e.g. as inverted energy register curves [9], as  $x - \text{MPF}(x)$  curves, as the surface area generated per unit mass  $A(x)$  ( $\text{m}^2/\text{kg}$ ), as cumulative number of fragments retained on each sieve size fraction  $N(x)$ , etc.

The  $x - A(x)$  data sets were plotted in a log-normal scale for all the 85 blast tests. Here  $x$  denotes the arithmetic mean value of the lower and the upper limits of each sieve size fraction bins ( $m$ ). The curves had poly-line character with three different slopes. The two kinks connecting the three regions were at  $100\ \mu\text{m}$  and  $1\ \text{mm}$ , see Fig. 1.2(a).

The  $x - N(x)$  data sets were plotted in a log-log scale [5]. They were plotted for three samples each from a different material, namely granodiorite, phyllite and grout. In these plots, three fixed regions of  $38\ \mu\text{m} \leq x < 0.106\ \text{mm}$ ,  $0.106\ \text{mm} \leq x < 37.5\ \text{mm}$  and  $x \geq 37.5\ \text{mm}$  were defined, see Fig. 1.2(b).

The different regions of  $x - A(x)$  and  $x - N(x)$  curves were postulated to correspond to different fragmentation mechanisms [2, 5]. In both the data representation methods, the slopes of each region varied somewhat with the material and the test type.

Banadaki [6] studied blast-induced fracture in Laurentian and Barre granite. He measured their mechanical properties, i.e. static and dynamic elastic and strength values. The blast samples were either cubic or cylindrical in shape. He used three types of detonating cord with different strength values of  $1.2\ \text{g/m}$ ,  $3\ \text{g/m}$  and  $5.3\ \text{g/m}$ .

Using dye impregnation, the crack patterns were identified at three planes along the axis of the cylinders. The cracks longer than  $2.5\ \text{mm}$  were manually mapped. Then, the crack density values were calculated at three cylindrical concentric zones around the blast-hole such that the total length of the cracks in each zone was divided by the corresponding surface area of the zone. He [6] showed that the

average density of the cracks (longer than 2.5 mm) at the three depths for the core layer is larger than for the other two layers.

Chi [7] blasted 26 lab-scale cylinders and cubes of granite. He studied pressure and attenuation of blast-induced shock waves and fragmentation and fractures around a blast-hole.

The pressure and attenuation of shock waves were measured at four different distances in the axial direction from the explosive charge. He [7] described the relation between the measured peak pressures ( $P_{\text{peak}}$ ) and the corresponding distances to the explosive charges ( $x_d$ ) by an exponential function  $P_{\text{peak}} = A \exp(-b_t x_d)$  [10] with the attenuation of  $b_t = 0.04$ .

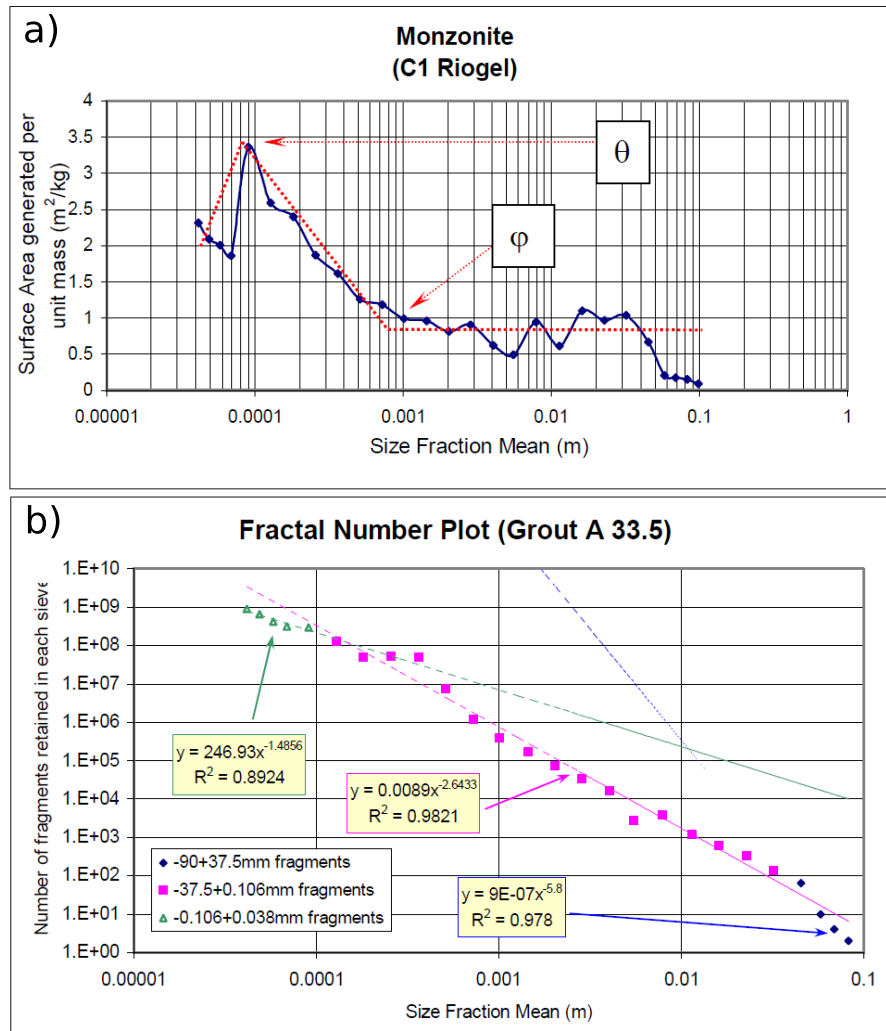


**Figure 1.2:** Michaux [2] plots of  $x - A(x)$  and  $x - N(x)$ . a) The plot of  $x - A(x)$  in a log-normal scale, the fragments sub-population of monzonite has three regions with different gradients. The thresholds are indicated with  $\theta \sim 100 \mu\text{m}$  and  $\phi \sim 1 \text{ mm}$ . b) The plot of  $x - N(x)$  in a log-log scale, the grout data set has three regions with different gradients. The size ranges are fixed and are indicated in the figure.

Different explosive specific charges, decoupling ratios and three different confining conditions were used to study fragmentation and fracture around blast-holes. The outer boundary confinements were either free, a ring filled with gravel or filled with cement grout. In the experiments blasted with small-weight charges, the number of radial cracks in the cylinders confined by gravel was higher than that of the cylinders confined by cement grout. Chi [7] also noted that both the length and the opening of cracks were also larger in the cylinders confined by gravel. The unconfined cylinders blasted with large-weight charges were fragmented into small pieces while the cylinders confined by cement fill were broken into large fragments in addition to small size fragments.

He [7] also used strain gauges and digital image correlation analysis to correlate the fracture patterns observed on each of the blasted specimen to the location of the maximum concentration of strain. He noted that the maximum concentration of strain obtained from the digital image correlation analysis corresponded well to the position of the dominant cracks and the fracture patterns. Furthermore, he added that the dominant cracks were initiated from or around the outer surface rather than close to blast-hole.

### 1.2.2 Fragmentation characteristics and prediction equations

In fragmentation, a particular material body breaks into smaller pieces. This may occur at any length scale such as asteroid collisions, geological and industrial applications, and atomic scale. Fragmentation is the basis for industrial processes such as mining and mineral recovery, where initially the rock containing the minerals is broken into smaller pieces to achieve e.g. transportable material fragments. The fragments are then further broken in the subsequent crushing and milling steps to the desired sizes suitable for the processing units where the valuable minerals are separated from the waste rock materials. The fragments that are too large or too small become economic and environmental liabilities. Therefore, reducing these liabilities are an important objective in such industries. One way to achieve this, is by recognizing the responsible dynamic fragmentation mechanisms forming the fine-fragments. Recently, many researches have focused on understanding the fragmentation characteristics.

One of the first and the most important characteristics of the fragmentation is that the FSDs in number-frequency [11] representation, i.e.  $s - n(s)$ , has a power-law behavior [12, 13, 14, 15, 16, 17] which is sometimes combined with exponential cut-offs. It was shown that there is a threshold in the amount of imparted energy to the material body where the transition from damage to fragmentation occurs [18, 19, 20]. At low levels of imparted energy, the size distribution has two distinct

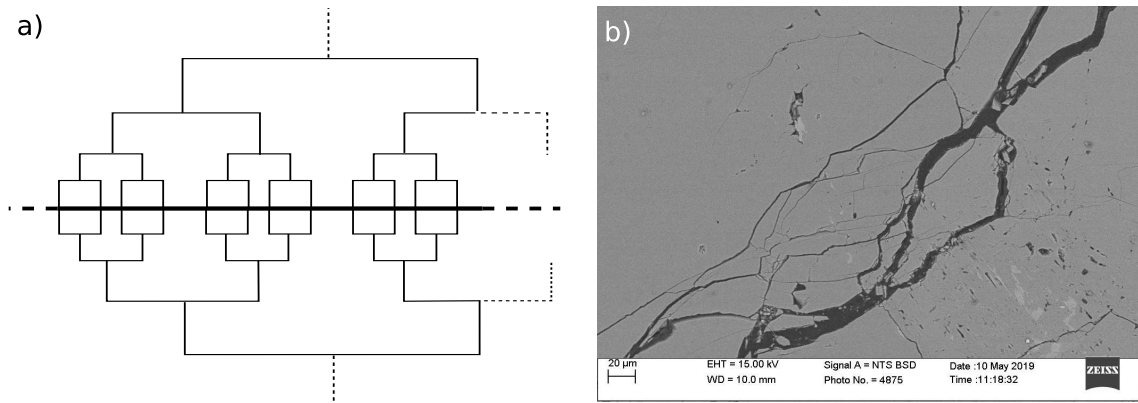


**Figure 1.3:** a) Schematic representation of a 2D crack branching and merging fragments formation on both sides of a propagating crack. Thick line in the middle is the main crack and the thin lines are side branches [15]. b) A branching and merging mechanism and the resultant fragmentation in granite blasted with 20 g/m of PETN. The figure is taken by scanning electron microscope [3].

parts which are separated with a gap, i.e. one consisting of a few very large fragments and one for a few small fragments having a fast decaying power-law distribution [20]. In blasting, this type of fragment size distribution is called dust and boulders [21]. As the imparted energy increases, the gap gradually disappears and a continuous distribution forms [20], see e.g. Fig. 4 in [20].

At this critical point, the continuous distribution has two parts with different characteristics. The first part, i.e. roughly the range of small fragments, has a power-law distribution with an exponential cut-off [12, 13, 14, 15, 17, 19, 22]. Åström et al. [13, 15] studied the branching-merging of unstable crack tips in brittle materials and associated a universal power-law exponent in the size distribution to this term, Fig. 1.3. Kun et al. [22] reported a higher value for the exponent valid for crushing-shearing than that for the branching-merging. Equation 1.1 shows such a function where  $\tau$  is the power-law exponent of the size distribution and  $f(s/s_1)$  is an exponential function that acts on the fragments with size  $s$  when  $s > s_1$ .

$$n(s) \propto s^{-\tau} f(s/s_1), \quad (1.1)$$

The second part, i.e. the size distribution for large fragments, has been represented by an exponential cut-off of the power-law, Eq. 1.2 below, [12, 15, 23] or a two-parameter Weibull distribution [18].

$$n(s) \propto \exp\left(\frac{-s}{s_0}\right), \quad (1.2)$$

Aggregate products are, on the other hand, often defined in terms of their MPF distribution. The MPF(x) is defined as the fraction of mass for a collection of



fragments that passes through sieves with different mesh-sizes  $x$ . That is, for a mesh-size  $x = 0$ ,  $\text{MPF}(x = 0.0)$ , and  $\text{MPF}(x > x_{\max}) = 1.0$  or 100%, where  $x_{\max} \sim$  largest-possible-fragment.

Several fragmentation prediction equations have been developed to correlate the blasting configuration with the final mass passing fraction such as the Kuz-Ram model, the Crush Zone Model (CZM) [24] and the Two-Component Model (TCM) [25] which is a development of the CZM. These models, however, have weaknesses when describing the experimental MPF curves [8]. In practice, the MPFs of blasted and crushed rocks are quite well described by the 3- or 5-parameter Swebrec<sup>©</sup> functions [26]. They read,

$$P(x) = 1/[1 + f(x)], \quad (1.3)$$

where  $f(x)$  of the 3- and 5-parameter Swebrec<sup>©</sup> function respectively read,

$$f(x) = [\ln(\frac{x_{\max}}{x})/\ln(\frac{x_{\max}}{x_{50}})]^b, \quad (1.4)$$

$$f(x) = a[\ln(\frac{x_{\max}}{x})/\ln(\frac{x_{\max}}{x_{50}})]^b + (1 - a)[(\frac{x_{\max}}{x}) - 1/(\frac{x_{\max}}{x_{50}}) - 1]^c, \quad (1.5)$$

$P(x)$  denotes the relative mass amount passing a rectangular mesh of size  $x$ . The 3-parameter version contains parameters  $x_{50}$ ,  $x_{\max}$  and  $b$  which are the median fragment size (50% passing size), the upper fragment limit, and the curve undulation parameter, respectively. The 5-parameter version contains also parameters  $a$  and  $c$  giving a Gates-Gaudin-Schuhman type or a power-law function with exponent of 1 when the mesh size approaches zero,  $x \rightarrow 0$ . Experience says that the coefficient of determination  $r^2 > 0.995$  in 95% of the cases tested [26, 27, 28]. In these fragment size distribution functions, however, unlike in the  $s - n(s)$  description of fragmentation the parameters are not correlated to any specific fragmentation mechanisms.

### 1.2.3 Numerical methods for simulating fracture and fragmentation

By the advancement of computation power and numerical tools, many researchers have started to investigate dynamic brittle fracture and fragmentation through numerical methods. There are two common types of methods; one based on a continuum mechanics formulation i.e. the Finite Element Method (FEM), and the other one based on discrete particles, i.e. the Discrete Element Method (DEM) and

Smooth Particle Hydrodynamics (SPH) [29].

### Continuous methods

Simulation of crack propagation in classical FEM has limitations. The limitations arise because the material in FEM is fundamentally considered as a continuum. Therefore, once the continuity of the displacement field is broken due to crack nucleation or propagation, re-meshing is a necessity to not only distinguish generated surfaces but also to update the boundary conditions [30].

Application of damage- or fracture mechanics concepts have overcome this issue. The former belongs to the category of continuous descriptions and describes fracture as a process of strain accumulation and damage growth. The latter belongs to the category of discontinuous descriptions, and explicitly introduces displacement discontinuities along the flanks of propagating cracks.

The two FEM classes, the Extended and Embedded Finite Element Methods (XFEM and EFEM) allow the crack (discontinuity) to propagate through individual finite elements. To do so, an additional set of parameters is introduced to describe the discontinuity within the finite elements. The main difference between XFEM and EFEM is how these new parameters are introduced. XFEM increases the total number of global degrees of freedom [31]. Alternatively, EFEM stores the additional degrees of freedom locally on the element level to avoid increasing the total size of system [31]. These classes are, however, limited in their application once the dynamics of several cracks existing in one system have to be simultaneously calculated [29, 32].

Constitutive models based on damage mechanics are more suitable when a system contains several cracks/failures, see e.g. [32, 33]. These models define the correlation between the damaged and undamaged medium using a damage variable  $d$  or  $D$ . This can be made using one or several scalar variables [34, 35] or using a tensor of different orders [34, 36, 37]. The damage models are often coupled with elastic constitutive models [38, 39, 40, 41] or with plasticity [42, 43, 44, 45, 46, 47].

Depending on the mechanical properties of the material, the choice of a damage criterion may change [48]. Brittle and quasi-brittle materials, i.e. concrete and rock-like materials, require different damage thresholds in tension and compression. This is related to the fact that damage can be active or inactive. In tensile failure, material stiffness degrades due to nucleation and propagation of microcracks, voids, etc. However, upon load reversal the tensile crack closes and consequently compressive stiffness recovers to carry load in compression [48]. A similar stiffness recovery from compression to tension does not occur.

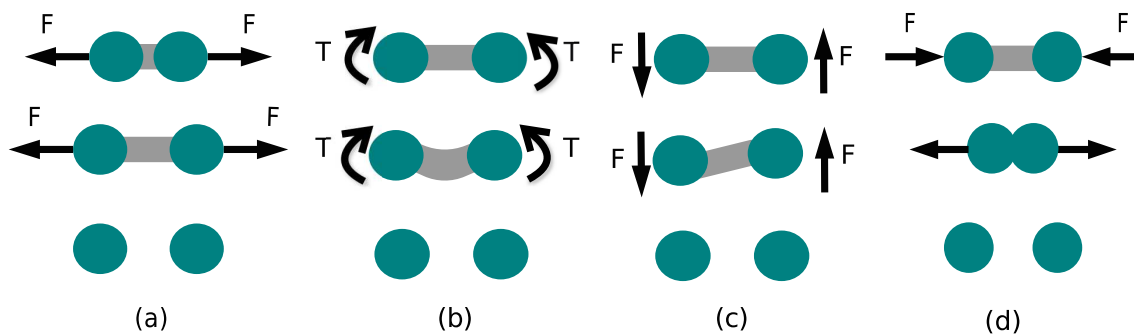


**Figure 1.4:** Failure mechanisms due to a) tension, b) bending, c) shearing, and d) compression, particles come into contact experiencing repulsive force.

The damage models have been used extensively to study the induced damage and dynamic crack propagation in concrete and rock-like materials [49, 50, 51] at high loading rates [6, 32, 33, 52] and to study the influence of different boundary conditions on the resultant fracture pattern [53].

### Discontinuous methods

The numerical methods based on continuum mechanics encounter limitations when a large number of discontinuities in a system exist. They are, however, progressing towards more sophisticated analysis of the propagation of discontinuities [32]. An alternative approach to study the dynamic brittle fracture is a particle-based formulation such as DEM and SPH.

In DEM the material is represented as an assembly of independent rigid particles connected with each other within a predefined distance. The interactions between the particles may be described by contact laws, i.e. elastic laws coupled with Coulomb friction [54], Van der Waals forces [55], linear and Hertz contact models which are applied in three dimensional particle flow code (PFC3D), etc.; or by using elastic strings or beams [56, 57]. Beams in 3D can account for tension, compression, shearing, bending, and torsion of the contacts, see Fig. 1.4. They can also have geometrical features, i.e. length and cross-sectional area. Due to the discrete nature of each particle, the discontinuities nucleate and propagate by breakage of the beams.

The DEM has been used in a variety of problems investigating fracture and fragmentation such as simulation of fracture and fragmentation induced by blast loads [58, 59, 60], or induced by high loading rate impacts [20, 61, 62, 63, 64]; simulation of single crack propagation in uniaxial tension and compression and mixed-mode loading [65, 66]; and simulation of fracturing and calving of glaciers [56, 67, 68]. Coupled DEM-FEM [57, 69] and DEM-SPH [70] methods have also been developed to analyze the dynamics of crack propagation and blast-induced fractures.

In rock mechanics and related mining research, DEM codes are being used for simulating geometrical configurations such as lab-scale cubes and cylinders [27, 4], bench blasts [51, 71], tunnel rounds [69], and sub-level caving rounds [72]. Simulation of full scale blasting requires a coarse discretization of the geometries to achieve results in an acceptable amount of calculation time. Hence, recognizing different source mechanisms creating the fine-fragments at full-scale becomes virtually impossible.

### 1.3 Motivations and Objectives

The amount of mineral fine-fragments that are produced has practical and economic consequences in the production of raw materials, especially for the sustainability of raw material resources. In the European Union project Less Fines [73] the volume of the waste fine-fragments is estimated to be 400-500 million tons annually in Europe alone. Blasting and downstream crushing and milling are the major sources of fine-fragments of rock [73]. The fine-fragments are essentially related to the amount of input energy [74]. Most of the fracture area created resides in the fine-fragments and this area determines the energy consumed [9]. A better knowledge of how the fine-fragments are generated could help to improve blasting and crushing practices by suppressing the amount of fine-fragments at the source rather than dealing with them afterward.

One existing theory on the source of fine-fragments, the CZM, assumes that fine-fragments originate from an annular compressive failure zone around a blast-hole [24], see Fig. 1.5(a). The MPF of the CZM consists of two non-overlapping Rosin-Rammler components, one for the coarse material and one for the fine material of the crushed zone. The CZM may be interpreted so that the fragment size is almost (solely) defined by the distance to a blast-hole. Alternatively, in the TCM the connection between the distance and the fragment size is more diffuse [25]. The TCM [25] defines the shear failure along the in situ joints and blast-induced cracks as another important source of fine-fragments [75].

Additions to the CZM by Onederra et al. [76] assume that the fine-fragments originate from a circular compressive failure zone around a blast-hole, as well as from crushed and sheared material bounded by major blast-induced radial cracks. The radial cracks are assumed to be evenly distributed around a blast-hole, to be planar, and also to continue along the length of the explosive charge. This constitutes the star-shaped crush zone model, see Fig. 1.5(b).

Another yet plausible mechanism by which most of the fine-fragments are generated involves dynamic crack branching and merging [8]. Hence, the objective of

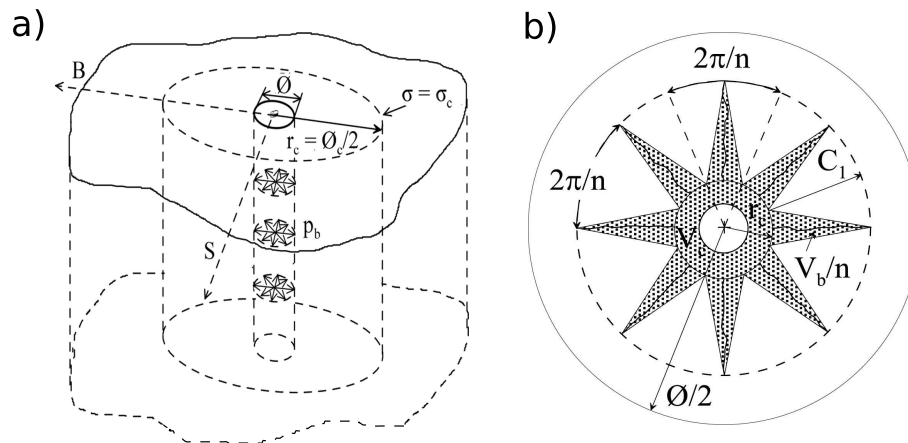


**Figure 1.5:** Schematic view of a) CZM [24], b) star shape model [76]. Figures are taken from [77]

this thesis is to use numerical methods and simulations to gain insight into the role of branching-merging in blast fragmentation. This leads to the following tasks:

1. To create a three-dimensional numerical model that describes the fracturing behavior of quasi-brittle materials, i.e. concrete or rock-like materials, when subjected to a civil blast load.
2. To compute the FSDs of the numerical models, especially for the fine-fragments.
3. To compare the computed FSDs with the results from the experiments carried out as a part of the FWF project [3] and from the literature.
4. To provide a scientific explanation of how these fine-fragments are generated.

The research tasks are answered in the four papers I-IV on which this thesis is built. Figure 1.6 shows the relation between each paper and the research tasks. Figure 1.7 shows how the papers are connected with each other.

## 1.4 List of papers and contribution of the author to the papers

### Paper I

A. Iravani, I. Kukulj, F. Ouchterlony, T. Antretter, and J. A. Åström, Modelling blast fragmentation of cylinders of mortar and rock, in *Proceedings of 12th International Symposium for Rock Fragmentation by Blasting, Luleå, Sweden*, edited by H. Schunnesson & D. Johansson, (Luleå University of Technology, Luleå), 597 (2018).

### Paper II

A. Iravani, J. A. Åström, and F. Ouchterlony, *Physical Origin of the Fine-Particle Problem in Blasting Fragmentation*, Phys. Rev. Applied 10, 034001 (2018).

### Paper III

I. Kukulj, A. Iravani, and F. Ouchterlony, *Using Small-scale Blast Tests and Numerical Modelling to Trace the Origin of Fines Generated in Blasting*, BHM Berg- und Huettenmaennische Monatshefte 163 (10), 427 (2018).

### Paper IV

A. Iravani, F. Ouchterlony, I. Kukulj, and J. A. Åström, *Generation of fine fragments during dynamic propagation of pressurized cracks*, Phys. Rev. E, accepted.

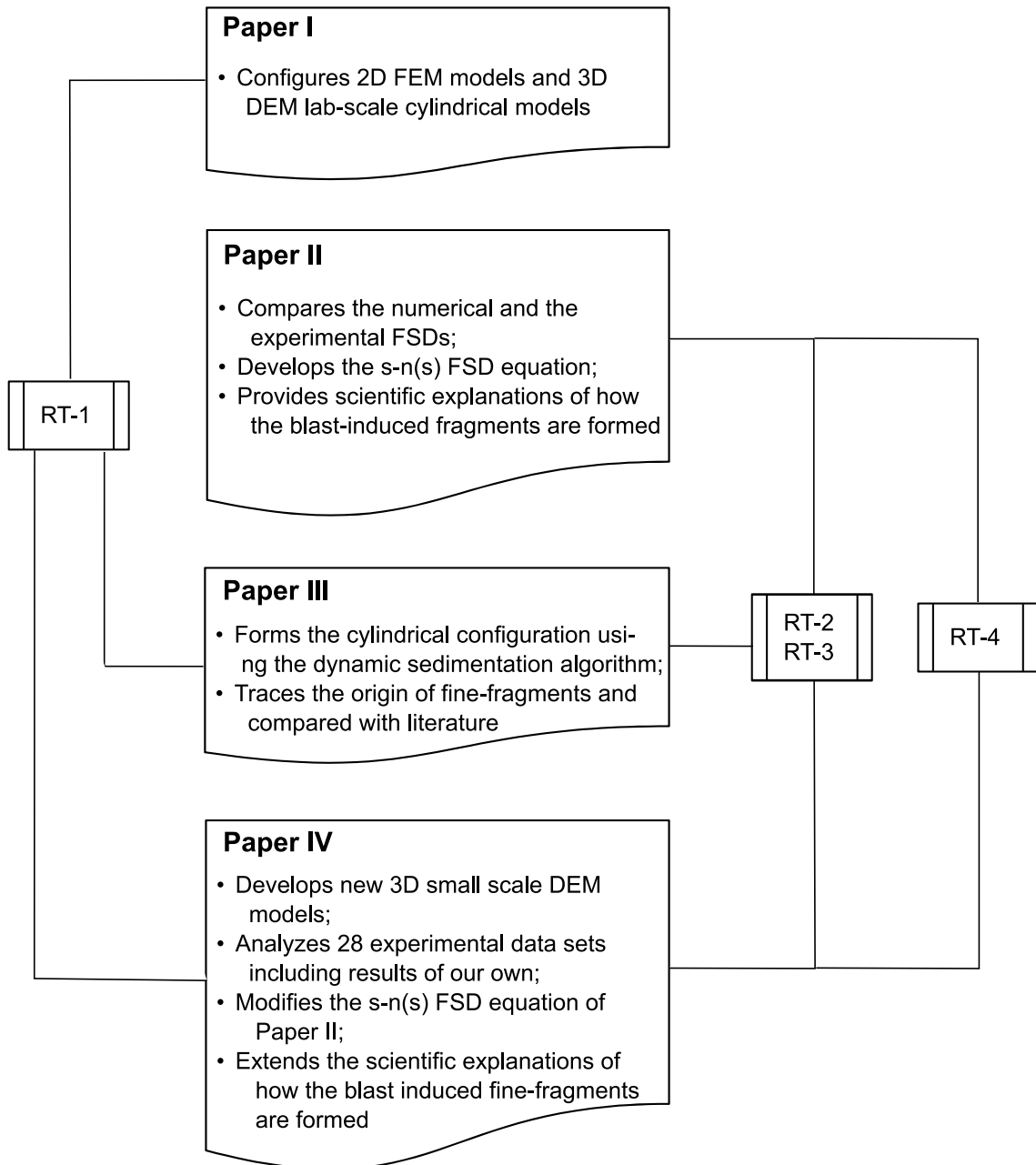


**Figure 1.6:** The relationships between research tasks (RT) and the appended papers

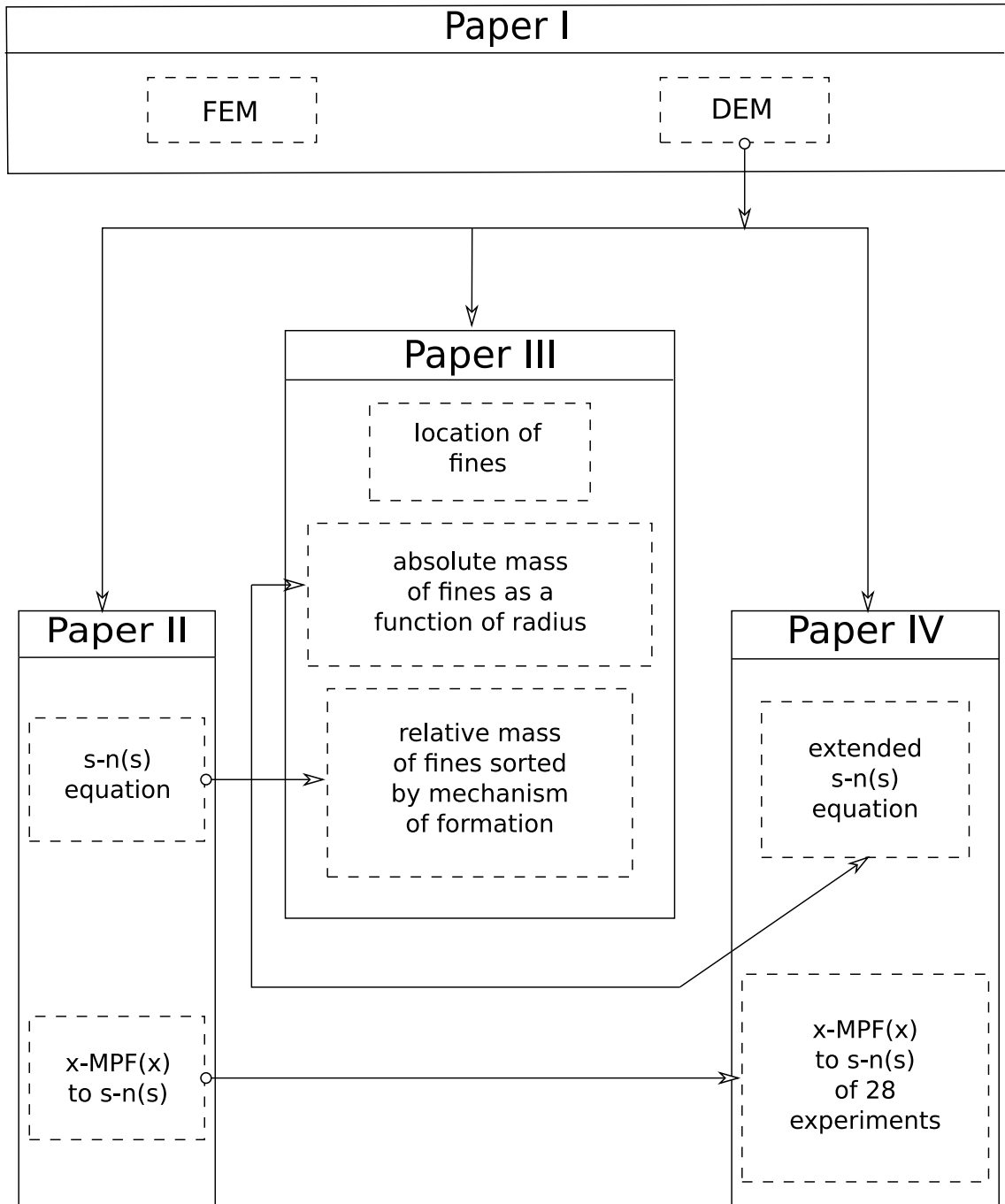


**Figure 1.7:** The relationships between the contents of the appended papers



This page intentionally left blank.

## 2 Theoretical background

### 2.1 Constitutive theories to describe concrete behavior

The experimentally measured stress-strain curve of concrete during cyclic loading has an unloading slope, it shows softening behavior, see Fig. 2.1(a)-(b) [78, 79]. Elastic-damage and elastic-plastic constitutive material models cannot describe this behavior of concrete thoroughly [80].

An elastic damage model cannot capture irreversible strains, Fig. 2.1(c), and an elastic-plastic model has unloading curves that follow the elastic slope, Fig. 2.1(d).

An elastic-plastic damage constitutive theory overcomes these issues. In this constitutive model, the damage part accounts for both the softening behavior and the decrease of the elastic modulus. The irreversible strains are captured by the plasticity formulation, Fig. 2.1(e).

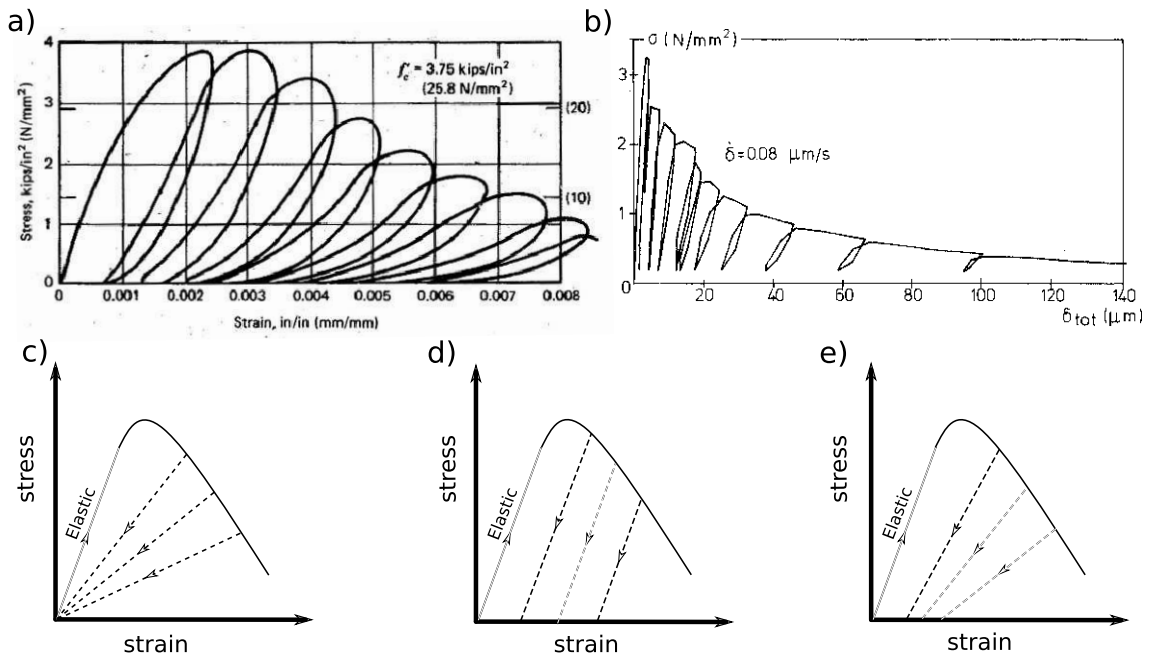


**Figure 2.1:** a) Compressive stress-strain loading-unloading curves for a concrete cylinder with high-intensity repeated compressive loading, the figure is taken from [78]; b) Tensile stress-strain curve in a post-peak cyclic test, the figure is taken from [79]; Schematic representation of the loading-unloading behavior in c) an elastic-damage constitutive model, d) an elastic-plastic constitutive model, and e) an elastic-plastic damage constitutive model.

### 2.1.1 Concrete damage plasticity formulation [1]

The constitutive theory aims to capture the effect of the irreversible damage associated with the failure mechanisms in concrete. It is based on the work of Hillerborg et al. [81], Lubliner et al. [42] and Lee and Fenves [45]. The model uses an additive strain rate decomposition for the rate-independent model ( $\dot{\boldsymbol{\varepsilon}} = \dot{\boldsymbol{\varepsilon}}^{el} + \dot{\boldsymbol{\varepsilon}}^{pl}$ ). The stress-strain relations are governed by scalar damaged elasticity,

$$\boldsymbol{\sigma} = (1 - d)\bar{\boldsymbol{\sigma}}, \quad (2.1)$$

$$\bar{\boldsymbol{\sigma}} \stackrel{\text{def}}{=} \mathbf{D}_0^{el} : (\boldsymbol{\varepsilon} - \boldsymbol{\varepsilon}^{pl}) \quad (2.2)$$

where  $d$  is the scalar damage variable,  $\mathbf{D}_0^{el}$  is the initial undamaged elastic stiffness,  $\bar{\boldsymbol{\sigma}}$  is the effective stress and  $\boldsymbol{\sigma}$  is the Cauchy stress.

The equivalent plastic strain ( $\varepsilon^{pl}$ ) is used as the hardening variable. It controls the evolution of the yield surface and the degradation of the elastic stiffness. The hardening variable is decomposed in two components of tensile and compressive equivalent plastic strain values ( $\tilde{\varepsilon}_t^{pl}$ ,  $\tilde{\varepsilon}_c^{pl}$ ). Damaged states in tension and compression ( $d_t$  and  $d_c$ , respectively) are characterized independently by these two hardening variables and other field variables  $f_i$ ,

$$d_t = d_t(\tilde{\varepsilon}_t^{pl}, f_i); \quad 0 \leq d_t \leq 1, \quad (2.3)$$

$$d_c = d_c(\tilde{\varepsilon}_c^{pl}, f_i); \quad 0 \leq d_c \leq 1 \quad (2.4)$$

The evolution of the hardening variables are expressed as rate expressions of equivalent tensile and compressive plastic strain ( $\dot{\tilde{\varepsilon}}_t^{pl}$ ,  $\dot{\tilde{\varepsilon}}_c^{pl}$ ). The evolution equation for general multiaxial stress conditions can be expressed in the following matrix form,

$$\dot{\boldsymbol{\varepsilon}}^{pl} = \begin{bmatrix} \dot{\tilde{\varepsilon}}_t^{pl} \\ \dot{\tilde{\varepsilon}}_c^{pl} \end{bmatrix} = \hat{\mathbf{h}}(\hat{\boldsymbol{\sigma}}, \tilde{\boldsymbol{\varepsilon}}^{pl}) \cdot \hat{\boldsymbol{\varepsilon}}^{pl}, \quad (2.5)$$

where the tensor  $\hat{\boldsymbol{\sigma}}$  contains the eigenvalues of  $\bar{\boldsymbol{\sigma}}$ , and  $\hat{\boldsymbol{\varepsilon}}^{pl}$  is a tensor containing the eigenvalues of the plastic strain rate tensor such as,

$$\hat{\boldsymbol{\varepsilon}}^{pl} = \begin{bmatrix} \hat{\varepsilon}_1 \\ \hat{\varepsilon}_2 \\ \hat{\varepsilon}_3 \end{bmatrix} \quad (2.6)$$

and  $\hat{\mathbf{h}}(\hat{\boldsymbol{\sigma}}, \hat{\boldsymbol{\varepsilon}}^{pl})$  is a tensor containing stress weight factor,  $r(\hat{\boldsymbol{\sigma}})$ . If the eigenvalues of the plastic strain rate tensor are ordered such that  $\hat{\varepsilon}_1 \geq \hat{\varepsilon}_2 \geq \hat{\varepsilon}_3$ , then for general multiaxial stress conditions

$$\hat{\mathbf{h}}(\hat{\boldsymbol{\sigma}}, \hat{\boldsymbol{\varepsilon}}^{pl}) = \begin{bmatrix} r(\hat{\boldsymbol{\sigma}}) & 0 & 0 \\ 0 & 0 & -(1 - r(\hat{\boldsymbol{\sigma}})) \end{bmatrix}, \quad (2.7)$$

with

$$r(\hat{\boldsymbol{\sigma}}) \stackrel{\text{def}}{=} \frac{\sum_{i=1}^3 \langle \hat{\sigma}_i \rangle}{\sum_{i=1}^3 |\hat{\sigma}_i|} \quad (2.8)$$

where  $\hat{\sigma}_i$  ( $i = 1, 2, 3$ ) are the principal stresses. The Macauley bracket  $\langle . \rangle$  is defined by  $\langle x \rangle = (1/2)(|x| + x)$ .

In multiaxial condition, the elastic stiffness degradation is isotropic and characterized by a single scalar variable,  $d$ , such that,

$$\mathbf{D}^{el} = (1 - d)\mathbf{D}_0^{el}; \quad 0 \leq d \leq 1 \quad (2.9)$$

For general multiaxial stress conditions the consistency of the scalar degradation variable  $d$  with the tensile and compressive damage parameters  $d_t$  and  $d_c$  is met by,

$$(1 - d) = (1 - s_t d_c)(1 - s_c d_t), \quad 0 \leq s_t \leq 1, \quad 0 \leq s_c \leq 1 \quad (2.10)$$

with

$$s_t = 1 - w_t r(\hat{\boldsymbol{\sigma}}), \quad 0 \leq w_t \leq 1, \quad (2.11)$$

$$s_c = 1 - w_c (1 - r(\hat{\boldsymbol{\sigma}})), \quad 0 \leq w_c \leq 1, \quad (2.12)$$

where parameters  $w_t$  and  $w_c$  are weight factors which control the recovery of the tensile and compressive stiffness values upon load reversal. The values for the weight

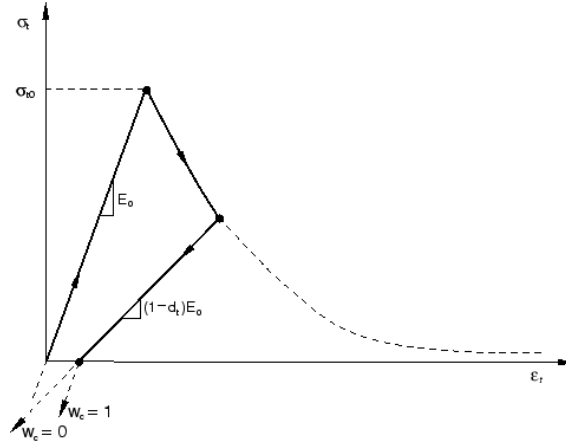


**Figure 2.2:** Influence of the  $w_c$  weight factor which controls the recovery of the tensile and compressive stiffness upon load reversal. Figure is taken from [1].

factors  $w_t = 0$  and  $w_c = 1$  correspond to no stiffness recovery and full stiffness recovery in tension and compression, respectively. Figure 2.2 illustrates the influence of the value for  $w_c$  weight factor upon load reversal. In uniaxial loading, the elastic stiffness is different between tension and compression,

$$\sigma_t = (1 - d_t)E_0(\varepsilon_t - \tilde{\varepsilon}_t^{pl}), \quad (2.13)$$

$$\sigma_c = (1 - d_c)E_0(\varepsilon_c - \tilde{\varepsilon}_c^{pl}), \quad (2.14)$$

where  $E_0$  is the initial undamaged elastic stiffness in uni-axial loading. The yield function [42, 45] of this constitutive theory is,

$$F(\bar{\boldsymbol{\sigma}}, \tilde{\boldsymbol{\varepsilon}}^{pl}) = \frac{1}{1 - \alpha} \left( \bar{q} - 3\alpha\bar{p} + \beta(\tilde{\boldsymbol{\varepsilon}}^{pl} < \hat{\boldsymbol{\sigma}}_{max} > -\gamma < -\hat{\boldsymbol{\sigma}}_{max} >) \right) - \bar{\sigma}_c(\tilde{\boldsymbol{\varepsilon}}_c^{pl}) \leq 0, \quad (2.15)$$

where  $\alpha$  and  $\gamma$  are dimensionless material constants,  $\bar{p} = -\frac{1}{3}\bar{\boldsymbol{\sigma}} : \mathbf{I}$  is the effective hydrostatic pressure,  $\bar{q} = \sqrt{\frac{3}{2}\bar{\boldsymbol{S}} : \bar{\boldsymbol{S}}}$  is the Mises equivalent effective stress with  $\bar{\boldsymbol{S}} = \bar{p}\mathbf{I} + \bar{\boldsymbol{\sigma}}$  as the deviatoric part of the effective stress tensor  $\bar{\boldsymbol{\sigma}}$ , and  $\bar{\sigma}_c$  is the effective compressive cohesion stress. The value for  $\alpha$ ,  $\gamma$ , and  $\beta(\tilde{\boldsymbol{\varepsilon}}^{pl})$  can be determined as,

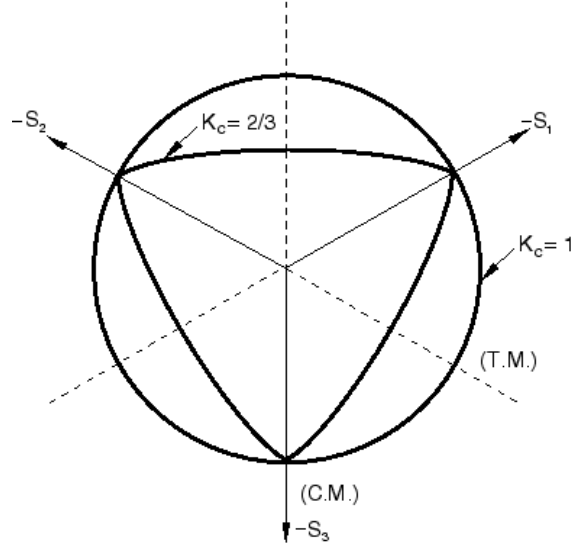


**Figure 2.3:** Shape of yield function in the deviatoric plane with different values of  $K_c$ . Figure is taken from [1].

$$\alpha = \frac{\sigma_{b0} - \sigma_{c0}}{2\sigma_{b0} - \sigma_{c0}}, \quad (2.16)$$

$$\gamma = \frac{3(1 - K_c)}{2K_c - 1}, \quad (2.17)$$

$$\beta(\tilde{\boldsymbol{\epsilon}}^{pl}) = \frac{\bar{\sigma}_c(\tilde{\boldsymbol{\epsilon}}_c^{pl})}{\bar{\sigma}_t(\tilde{\boldsymbol{\epsilon}}_t^{pl})}(1 - \alpha) - (1 + \alpha), \quad (2.18)$$

$\sigma_{b0}$  and  $\sigma_{c0}$  are the biaxial and the uniaxial compressive stress at failure, respectively. The value  $K_c$  controls the shape of the yield function.  $K_c = \frac{2}{3}$  is typical for concrete, Fig. 2.3. The plastic flow is governed by a flow potential  $G$ , i.e. here a Drucker-Prager hyperbolic function, according to the flow rule,

$$\dot{\boldsymbol{\epsilon}}^{pl} = \dot{\lambda} \frac{\partial G(\bar{\boldsymbol{\sigma}})}{\partial \bar{\boldsymbol{\sigma}}} \quad (2.19)$$

where  $G$  is,

$$G = \sqrt{(\epsilon\sigma_{t0} \tan \psi)^2 + \bar{q}^2} - \bar{p} \tan \psi \quad (2.20)$$

where  $\dot{\lambda}$  is the nonnegative plastic multiplier,  $\sigma_{t0}$  is the uniaxial tensile stress at failure,  $\epsilon$  is the eccentricity which defines the rate at which the function reaches asymptote (the flow potential tends to a straight line as the eccentricity tends to zero), and  $\psi$  is the dilation angle measured in the  $p$ - $q$  plane at high confining pressure.

Finally, the elastic-plastic response is described in terms of the effective stresses and the hardening variables,

$$\bar{\boldsymbol{\sigma}} = \mathbf{D}_0^{el} : (\boldsymbol{\varepsilon} - \boldsymbol{\varepsilon}^{pl}) \in \{\bar{\boldsymbol{\sigma}} | F(\bar{\boldsymbol{\sigma}}, \tilde{\boldsymbol{\varepsilon}}^{pl}) \leq 0\}, \quad (2.21)$$

$$\hat{\boldsymbol{\varepsilon}}^{pl} = \mathbf{h}(\bar{\boldsymbol{\sigma}}, \tilde{\boldsymbol{\varepsilon}}^{pl}) \cdot \dot{\boldsymbol{\varepsilon}}^{pl}, \quad (2.22)$$

$$\dot{\boldsymbol{\varepsilon}}^{pl} = \dot{\lambda} \frac{\partial G(\bar{\boldsymbol{\sigma}})}{\partial \bar{\boldsymbol{\sigma}}} \quad (2.23)$$

where  $\dot{\lambda}$  and  $F$  obey the Kuhn-Tucker conditions,

$$\dot{\lambda} F = 0; \quad \dot{\lambda} \geq 0; \quad F \leq 0 \quad (2.24)$$

If  $F(\bar{\boldsymbol{\sigma}}, \tilde{\boldsymbol{\varepsilon}}^{pl}) \leq 0$ , i.e. the damage criterion is not met, then according to Eq. 2.24  $\dot{\lambda} = 0$ , this yields  $\dot{\boldsymbol{\varepsilon}}^{pl} = 0$  which means no plastic flow occurs and therefore no damage occurs. On the other hand, if  $\dot{\lambda} > 0$  then further damage takes place. According to Eq. 2.24,  $F(\bar{\boldsymbol{\sigma}}, \tilde{\boldsymbol{\varepsilon}}^{pl}) = 0$  yields to a new damage threshold.

## 2.2 HiDEM formulation

In HiDEM, the spatial location of particles (mass points) are initially read and the connection between them is defined. The particles are connected via mass-less beams. At the beginning of a simulation, initial and boundary conditions are set. The displacement of the particles are computed using Newton's equation of motion [82, 56],

$$\mathbf{M}\ddot{\mathbf{r}}_i + \mathbf{C}\dot{\mathbf{r}}_i + \sum_j \mathbf{K}\mathbf{r}_{ij} = \mathbf{F}_i, \quad (2.25)$$

where  $\mathbf{M}$  is a mass matrix,  $\ddot{\mathbf{r}}_i$ ,  $\dot{\mathbf{r}}_i$ ,  $\mathbf{r}_i$  are the acceleration, velocity and position vectors of particle  $i$  including rotations.  $\mathbf{r}_{ij}$  are the position vectors for all particles  $j$  that are connected to particle  $i$ .  $\mathbf{C}$  is a damping matrix,  $\mathbf{K}$  is the stiffness matrix and  $\mathbf{F}_i$  is the sum of other forces acting on particle  $i$ . This is implemented in a time-discretized form in the HiDEM code [83, 82, 56],

$$\left[ \frac{\mathbf{M}}{\Delta t^2} + \frac{\mathbf{C}}{2\Delta t} \right] \mathbf{r}(t + \Delta t) = \left[ \frac{2\mathbf{M}}{\Delta t^2} - \mathbf{K} \right] \mathbf{r}(t) - \left[ \frac{\mathbf{M}}{\Delta t^2} - \frac{\mathbf{C}}{2\Delta t} \right] \mathbf{r}(t - \Delta t) + \mathbf{F}_i, \quad (2.26)$$

where  $t$  is the time and  $\Delta t$  is the time step.

Two particles are connected via Euler-Bernoulli beam. A beam bounded by two particles can be deformed either by translational motions or the rotations. The stiffness matrix  $\mathbf{K}$  for a single beam between two particles is [82],

$$\mathbf{K} = \begin{bmatrix} \alpha & 0 & 0 & 0 & 0 & 0 & -\alpha & 0 & 0 & 0 & 0 & 0 \\ 0 & \beta & 0 & 0 & 0 & \gamma & 0 & -\beta & 0 & 0 & 0 & \gamma \\ 0 & 0 & \beta & 0 & -\gamma & 0 & 0 & 0 & -\beta & 0 & -\gamma & 0 \\ 0 & 0 & 0 & \zeta & 0 & 0 & 0 & 0 & 0 & -\zeta & 0 & 0 \\ 0 & 0 & -\gamma & 0 & \eta & 0 & 0 & 0 & \gamma & 0 & \omega & 0 \\ 0 & \gamma & 0 & 0 & 0 & \eta & 0 & -\gamma & 0 & 0 & 0 & \omega \\ -\alpha & 0 & 0 & 0 & 0 & 0 & \alpha & 0 & 0 & 0 & 0 & 0 \\ 0 & -\beta & 0 & 0 & 0 & -\gamma & 0 & \beta & 0 & 0 & 0 & -\gamma \\ 0 & 0 & -\beta & 0 & \gamma & 0 & 0 & 0 & \beta & 0 & \gamma & 0 \\ 0 & 0 & 0 & -\zeta & 0 & 0 & 0 & 0 & 0 & \zeta & 0 & 0 \\ 0 & 0 & -\gamma & 0 & \omega & 0 & 0 & 0 & \gamma & 0 & \eta & 0 \\ 0 & \gamma & 0 & 0 & 0 & \omega & 0 & -\gamma & 0 & 0 & 0 & \eta \end{bmatrix} \quad (2.27)$$

with  $\alpha = EA/L$ ,  $\beta = 12EI/L^3$ ,  $\gamma = 6EI/L^2$ ,  $\zeta = GI_c/L$ ,  $\eta = 4EI/L$ ,  $\omega = 2EI/L$ .  $E$  is Young's Modulus,  $A$  is the cross sectional area of beam,  $L$  is the length of beam,  $I = bh^3/12$  is the moment of inertia of the cross section of beam with respect to its either of symmetry axes  $x$  or  $y$  (rectangular shape with width of  $b$  and height of  $h$ , here we have  $b=h$ ),  $I_c = (1/12)bh(b^2 + h^2)$  is the moment of inertia of the cross section of the beam with respect to its center point, and  $G$  is the shear modulus  $G = 1/2(1 + \nu)$ . The vector containing nodal displacements and rotations corresponding to the stiffness matrix  $\mathbf{K}$  is



$$\mathbf{r} = \begin{bmatrix} x_1 \\ y_1 \\ z_1 \\ \theta_{x1} \\ \theta_{y1} \\ \theta_{z1} \\ x_2 \\ y_2 \\ z_2 \\ \theta_{x2} \\ \theta_{y2} \\ \theta_{z2} \end{bmatrix} \quad (2.28)$$

For a model that contains a large number of particles, the stiffness matrix  $\mathbf{K}$  and the vector containing nodal displacements and rotations  $\mathbf{r}$  expand to contain all the degrees of freedom in the model.

### 3 Essential findings

#### 3.1 Paper I

In this paper initially blast-induced dynamic crack propagation, branching and merging in mortar are investigated using a FEM code with explicit time integration, namely Abaqus/Explicit [1]. The FE model is a cylindrical disk ( $\varnothing 140$  mm  $\times$  1 mm) with a centralized blast-hole, see Fig. 3.1(a). It is discretized with three dimensional linear hexahedral stress elements with reduced integration points, labeled “C3D8R” elements.

The blast-hole is loaded at three pressure levels equivalent to our own experimental setup [3], i.e. 6 g/m, 12 g/m, and 20 g/m of pentaerythritol tetranitrate (PETN) cords. The explosive pressure load is described by a pressure-time history function [84] which is applied radially on the blast-hole wall, see Fig. 3.1(b) and Eqs. 1-3 in Paper I.

On the outer boundary (cylinder periphery), a quiet boundary condition is defined using 3D infinite elements (CIN3D8), Fig. 3.1(a). This allows the incident shock wave that is propagating towards the outer boundary (cylinder periphery) to pass through the boundary without reflecting back into the model. As a result, the formation of spalling cracks due to the reflected tensile waves at the outer boundary is prevented. This allows us to investigate the crack propagation, branching and merging. Otherwise, the stress waves that reach the outer boundary reflect as tensile waves developing rings of tensile damage preventing the propagating cracks

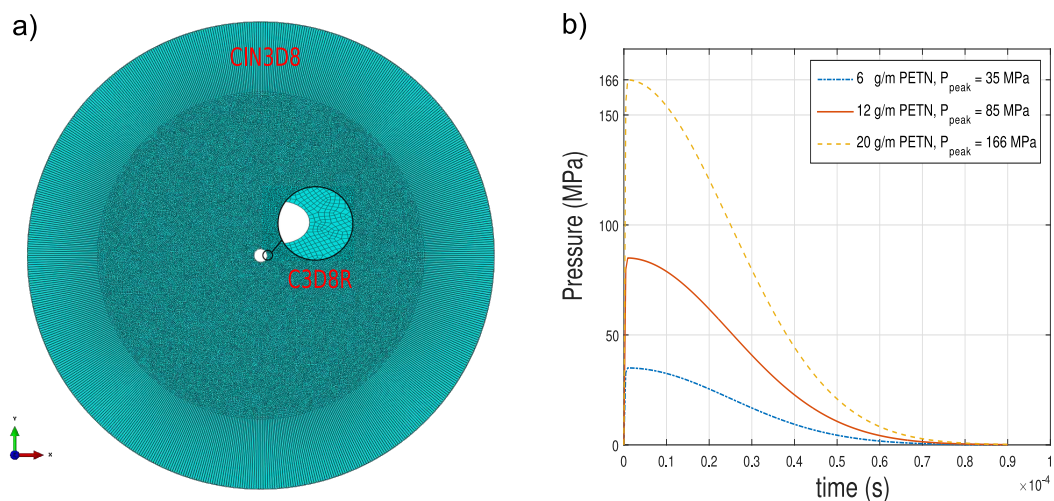


**Figure 3.1:** a) Top view of the FE model discretized using the C3D8R stress elements and a quiet boundary condition formed using the 3D infinite elements (CIN3D8) b) Pressure-time explosive loading history with three peak pressures of 35 MPa, 85 MPa, and 166 MPa used in the FE models.

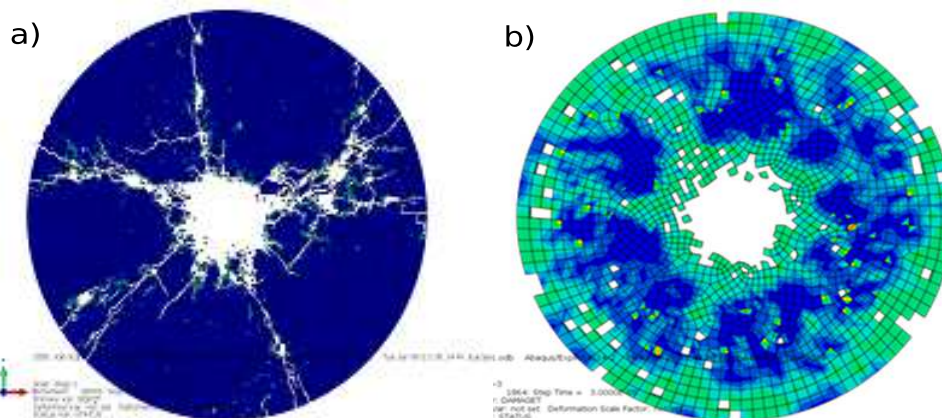


**Figure 3.2:** The fracture patterns developed a) with the application of the quiet boundary condition, b) free boundary condition.

originating around the blast-hole from being distinguishable, see e.g. Fig. 3.2. In the experimental setup [3] the MT is used at the outer boundary to prevent the reflection of the stress waves into the blasted medium, see Figure 2 in [85].

The built-in damage-plasticity constitutive material model in Abaqus/Explicit is used, namely Concrete Damage Plasticity (CDP), see Sec. 2.1.1. It lacks an Equation of State (EoS) for the pressure-volume relation that includes the nonlinear effects of compaction, see e.g. the works which have been completed by Holmquist, Johnson and their colleagues such as the HJC, JH-1, JHB, and the JH-2 constitutive material models [86, 87, 88, 89]. The EoS is a basic component in constitutive material models used to analyze highly dynamical processes.

To compensate for this lack in our constitutive material model, the FE model is calibrated by the use of linear and quadratic bulk viscosity parameters which introduce damping associated with the volumetric straining, see Fig. 3.3; Rayleigh damping coefficients; mass scaling to scale the mass of small finite elements that are controlling or reducing the stable time increment; and an element-by-element stable time increment estimate which is determined using the current dilatational wave speed in each element [1].

In addition to the 2D FE models, lab-scale size 3D models of the cylinder ( $\varnothing 140$  mm  $\times$  280 mm) are simulated. In these, similar instabilities as in the 2D models appear; in addition, they show unrealistic spiral shaped crack growth patterns. The material model calibration become extremely difficult and time consuming. Therefore, here the application of the FE models is limited to 2D. The 3D modeling is addressed using a discrete element method (HiDEM code).

Next, three-dimensional discrete element models of cylinders of mortar ( $\varnothing 140$  mm  $\times$  200 mm) are made. The simulations are made at the same three peak pressure

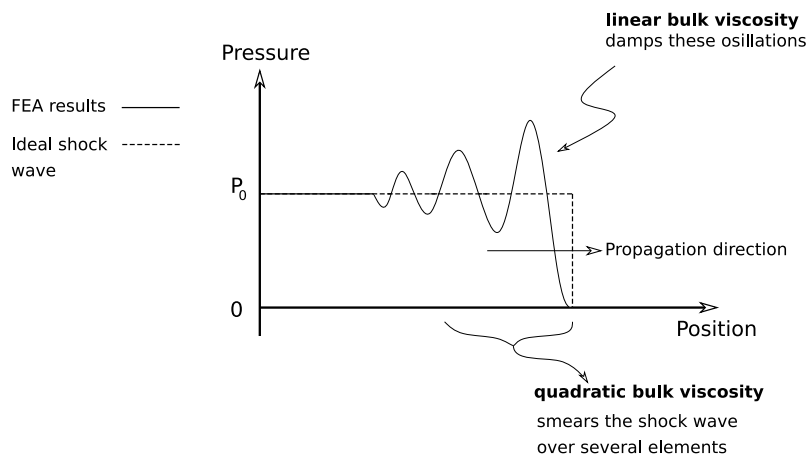


**Figure 3.3:** Propagation of a shock wave through a one-dimensional mesh [1]

levels as for the FE models. The blast load is a pressure-time history which is applied radially on the blast-hole wall for a duration of  $1 \mu\text{s}$ . In addition a simplified post-peak pressure drives all the particles outwards with a constant pressure. The detonation front has a VOD of  $6000 \text{ m/s}$ . A Face Centered Cubic (FCC) lattice structure is used to arrange the  $3\text{-mm}$  diameter particles in the cylindrical shape with the desired dimensions, and an elastic material constitutive model is used. At the outer boundary a quiet boundary condition using the velocity damping configuration is implemented.

In the FE models, the diameter of the crushed zone and the severely fractured zone and the crack network at the three explosive load levels are studied and reported in Tables 4 and 5 of Paper I. It is demonstrated that these quantities increase in magnitude by increasing the peak pressure level. Next, the resultant fracture patterns at the three load levels have been qualitatively compared with the end-face fracture patterns from in-house tests made in the same project (FWF research project: P27594-N29) [3]. It is shown that the FE models give realistic post-mortem end-face fracture patterns, see Fig. 3.4.

For the 3D HiDEM models, the MPF curves are evaluated. A fragment is defined by the number of connected particles it contains and the screen size of the fragment is that of a volume equivalent sphere. The resultant MPF curves have a Swebrec<sup>®</sup> function like distribution, and they show the Natural Breakage Characteristic (NBC) behavior postulated by Steiner [9] for the three consecutive increasing loading levels, see Fig. 10 in Paper I.

In addition, 3D internal crack networks of the three blasted cylinders are analyzed as a function of the explosive load level, see Fig. 8 in Paper I. It is shown that by increasing the peak pressure level the number of the radial cracks, branchings and mergings increase. The 3D crack networks show, however, a preferential direction of

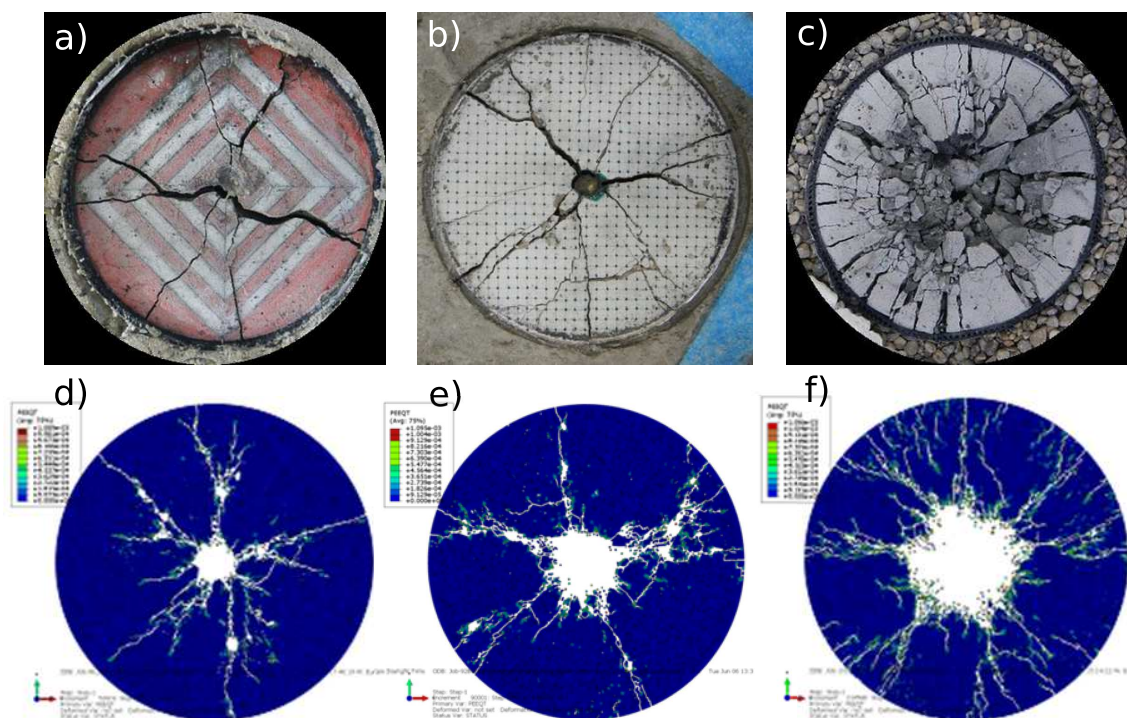


**Figure 3.4:** Experimental end-face fracture patterns of blasted mortar cylinders [3, 85] with PETN cords of a) 6 g/m, b) 12 g/m, and c) 20 g/m. The FE simulation results of the 2D disks blasted with the explosive load levels equivalent to e) 6 g/m of PETN, e) 12 g/m of PETN and f) 20 g/m of PETN. The deleted elements in the simulation results of Figs. (d)-(f) are shown in white.

crack propagation. This is probably associated with the FCC lattice structure used to build the cylinders.

### 3.2 Paper II

In this paper, the HiDEM code is used to simulate the blast-induced FSDs of lab-scale cylinders ( $\varnothing$  140 mm  $\times$  280 mm) with a centralized blast-hole. The simulations have been performed at five different charge concentrations, i.e. 3 g/m, 5 g/m, 10 g/m, 20 g/m, and 40 g/m of PETN cord. The post-peak amplitude in the pressure-time explosive loading function have to be calibrated to mimic the experimental results, as shown in Fig. 3(b) of Paper II.

The 3-mm diameter particles are arranged in a FCC lattice structure, see Fig. 3.5(a). An elastic material constitutive model is used. The simulation results are then compared to the experiments which were carried out at Luleå University of Technology [27] with an identical geometrical size and explosive load levels. In the experiments, the cylinders were confined by a cylindrical layer of pre-stressed aggregate, Fig. 3.5(b).

The resultant experimental FSDs are found to consist of three parts based on

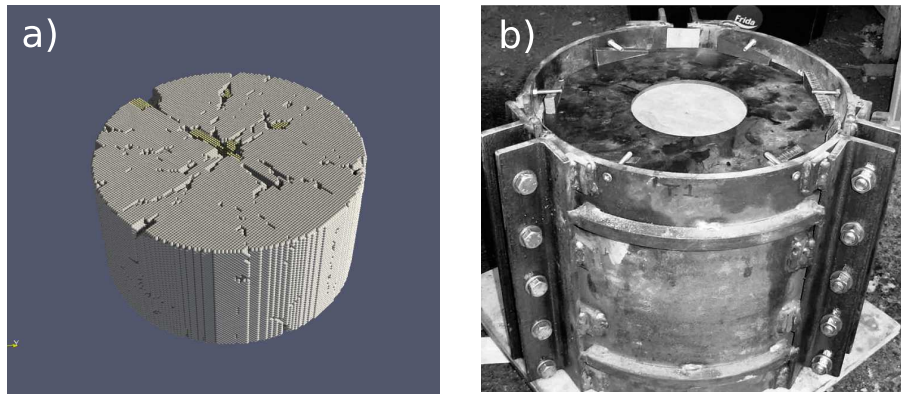


**Figure 3.5:** a) The HiDEM cylinder used in Paper II which is blasted with the explosive load level equivalent to 6 g/m of PETN, particles are arranged in a FCC lattice structure. b) The so-called stiff test set-up with a layer of pre-stressed aggregate around the outer periphery of the cylinder as the confining condition [90]. The pre-stressed level is determined by the torque used to tighten the bolts.

the slope of the  $s - n(s)$  curve in log-log space, i.e. fine-fragments, intermediate size fragments and boulders, see Fig. 3.6 below and also Fig. 2(b) in Paper II. An  $s - n(s)$  FSD equation is developed that describes the first two FSD parts by two power-law terms and an exponential cut-off for the second term. The third part of the FSD is described by a single exponential cut-off. The whole FSD, or the number of fragments in a size interval  $ds$  reads,

$$n(s)ds = C_1 s^{-\beta} ds + C_2 s^{-\alpha} \exp\left(-\frac{s}{C_3}\right) ds + n_b(s) ds, \quad (3.1)$$

where  $s$  is a dimensionless parameter that expresses the number of DEM parti-

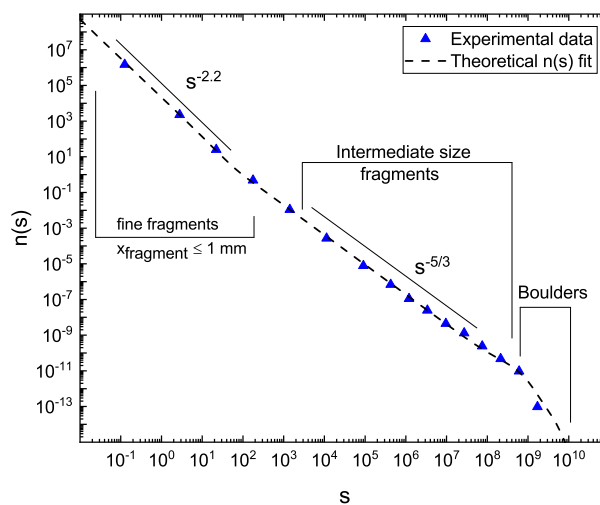


**Figure 3.6:** Fragment size distribution in  $s - n(s)$  space. Triangular data points represent the experimental data [27]. The data are fitted in log-log space using Eq. 3.1 and represented by the dashed line. The three regions of the FSD are marked.

cles forming a fragment, and  $n(s)$  defines number of fragments of size  $s$ . The first term expresses the number of fragments in a size interval  $ds$  formed in a crushing-shearing process, i.e.  $n_{\text{crush}}(s)ds = C_1 s^{-\beta} ds$ . The value for  $\beta \sim 1.8 - 3.5$  [15] can be determined from grinding experiments. This is discussed in the Results section of Paper II. Sometimes there appears also a large-size cut-off to this term which can be approximated by multiplying this term with an exponential function.

The second term expresses the number of fragments in a size interval  $ds$  formed in a branching-merging like process, i.e.  $n_{\text{bm}}(s)ds = C_2 s^{-\alpha} \exp(-s/C_3) ds$  [15, 17, 91]. This process is inherently universal and leads to a characteristic FSD with a power-law exponent  $\alpha = (2D - 1)/D$ , where  $D$  is the dimension (i.e.  $D = 1, 2, 3$  for rods, membranes, and bulk objects, respectively) [15, 17, 91]. For three dimensional objects  $\alpha = 5/3$ , which is very nearly the case for the intermediate range of the experimental FSDs in Fig. 3.6.  $C_3$  defines the initial point of the size range of the boulders.

The third term,  $n_b(s) \sim \exp(-s/s_b)$  is the size distribution for boulders, and  $s_b$  is the characteristic size of the boulders governed by the density of induced tensile cracks.  $C_1, C_2, C_3$  and  $\beta$  are non-universal constants, i.e. their values change from test to test.

The values of the power-law exponents, i.e.  $\beta$  and  $\alpha$ , indicate the responsible fragmentation mechanisms. In this article, it is established that for the stiff blasting setups, Fig. 3.5(b), the majority of the fine-fragments are generated as a result of compressive crushing-shearing. The intermediate-size fragments are formed due to unstable tensile crack propagation, branching and merging. And finally, the largest fragments or the boulders are formed by seemingly intact volumes between the major tensile cracks.

The HiDEM models used in this article overestimate the amount of fine-fragments formed by crushing-shearing compared with the experiments, see Figs. 2(a) and 3(a) in Paper II. This is caused by the resolution of the discretization. Figure 2(b) in Paper II displays a more useful comparison: as this figure demonstrates, the crushing part of  $s - n(s)$  data extend to the kink at about  $s \sim 20-30$  for both the experimental and the numerical data. Since the grain size in the numerical model is  $x_{\text{grain}} = 3$  mm, and in the experimental model  $x_{\text{grain}} \sim 0.1$  mm, this means that the mass fraction for crushing is much larger for the numerical data, and it indicates that numbers of grains rather than fragments' mass govern crushing.

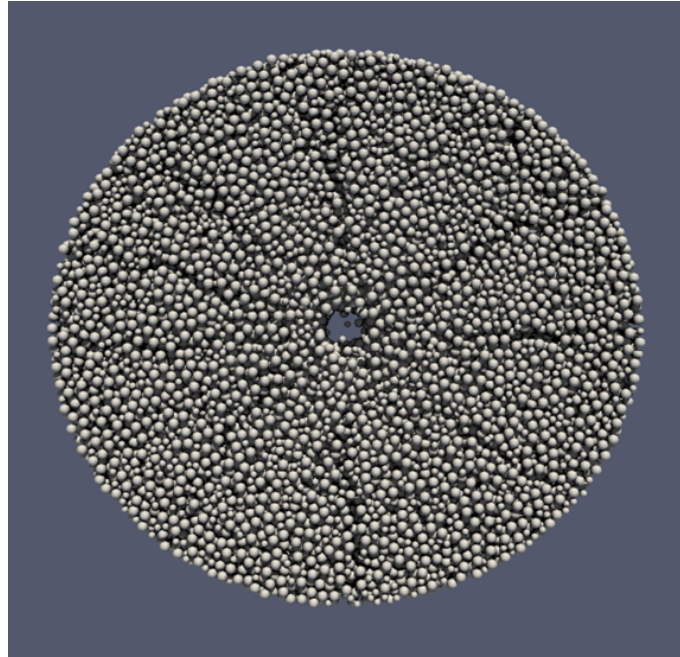


**Figure 3.7:** End-face fracture pattern of the HiDEM cylinder which is generated using the dynamic deposition algorithm.

### 3.3 Paper III

In this paper, we trace the origin of fine-fragments as a function of their distance to the blast-hole. The blast-induced FSDs of the lab-scale cylinders ( $\varnothing$  140 mm  $\times$  280 mm) with a centralized blast-hole are computed with HiDEM. The simulations are performed at three different explosive load levels equivalent to the PETN cord with the charge concentrations of 6 g/m, 12 g/m, and 20 g/m. The detonation front has a VOD of 7300 m/s. At the outer boundary a quiet boundary condition is used.

In Paper I, it was shown that the 3D crack networks have a preferential direction of crack propagation when the FCC lattice structure is used to create the desired geometrical configuration. A disordered structure that does not create preferential directions of crack growth would seem more appropriate for the materials like granite and magnetic mortar. This can be achieved by using a deposition algorithm for the creation of the geometry. In deposition, the geometrical domain is filled with the spherical particles. Each particle falls downwards until it collides with already existing particles or the pre-defined walls. The translation of the particles is determined based on the dynamics of the problem.

In this paper, Paper III, a dynamic deposition algorithm was programmed and it is used to generate cylinders consisting of 256091 spherical particles of 2 mm and 3 mm diameter. The reason for choosing a combination of 2 mm and 3 mm diameter is to induce more inhomogeneity in the material structure. The particles are randomly positioned within the cylindrical domain. This has solved the problem



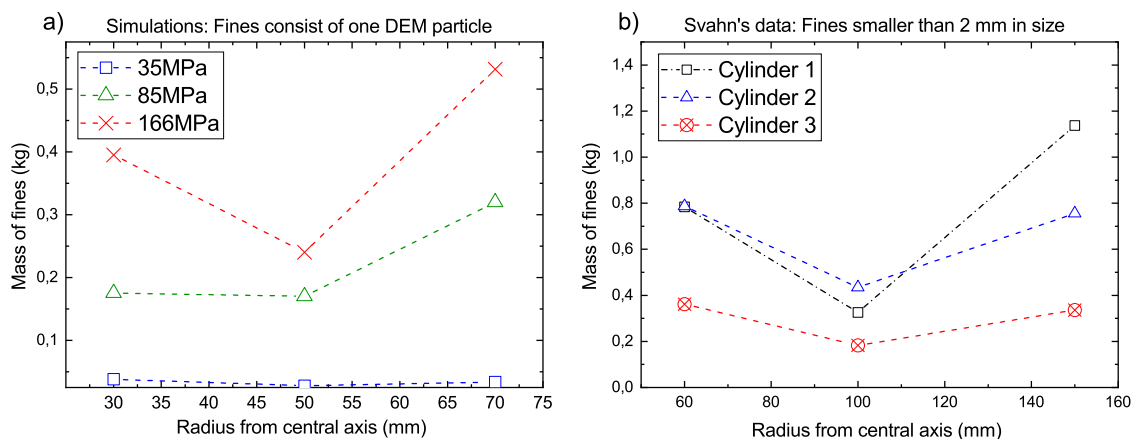


**Figure 3.8:** a) HiDEM simulation results, absolute mass of fine-fragments, i.e. fragments formed by one DEM particle, at three concentric cylinders with outer radii of  $r_{\text{outer}} = 30$  mm, 50 mm, and 70 mm. Three cylinders blasted at three explosive load levels of 35 MPa, 85 MPa and 166 MPa equivalent to 6 g/m, 12 g/m and 20 g/m of PETN cord, b) Svahn [4] experimental data of the fine fragments smaller than 2 mm at three concentric layers of black  $r_{\text{outer}} < 60$  mm, yellow  $r_{\text{outer}} < 100$  mm and green  $r_{\text{outer}} < 150$  mm for three blasted cylinders with 40 g/m of PETN.

of the preferential direction of crack propagation, see Fig. 3.7.

The resultant MPF curves have a dust-and-boulders characteristic [21] for the first two loading levels, see Fig. 14 in Paper III. The overestimation of the fine-fragments formed by the crushing mechanism addressed in Paper II still persists. The absolute masses of the fine-fragments are then computed at three concentric cylinders with outer radii of  $r_{\text{outer}} = 30$  mm, 50 mm, and 70 mm. The inner radii of the cylinders are  $r_{\text{inner}} = 5$  mm, 30 mm and 50 mm.

The simulation results show that the closest layer to the blast-hole contains fewer fine-fragments in absolute term than the sum of the fine-fragments of the other two layers, see Fig. 3.8(a). See Table-2 in Paper III for the calculated percentage mass fraction of fragments formed by crushing, branching-merging and the mass contained in the boulders. This agrees qualitatively with Svahn's results [4], see Fig. 3.8(b).

### 3.4 Paper IV

Even the DEM models with particles of diameters of 2 mm and 3 mm used in Paper II and Paper III were found to be too coarse to analyze the resultant fine-fragments FSDs in greater detail. Hence, recognizing different source mechanisms that create the fine-fragments become virtually impossible.

In this paper twenty-eight sets of experimental FSDs for lab-scale cylindrical specimen are analyzed [3, 27, 92]. Four of them are confined with a cylindrical layer of pre-stressed aggregate, i.e. the stiff confinement shown in Fig. 3.5(b), and the remaining twenty-four cylinders are either unconfined or confined by MT. In

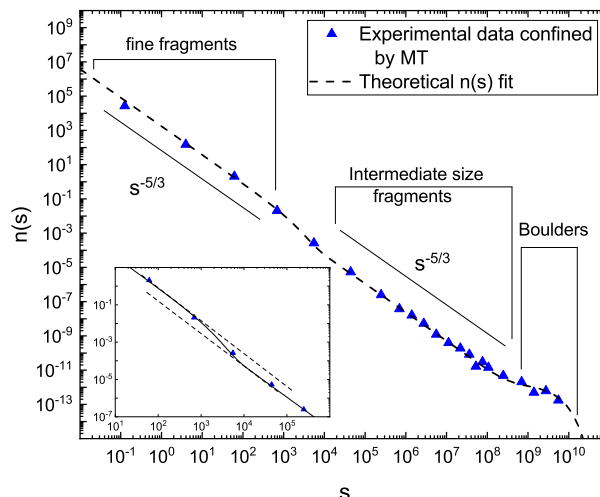


**Figure 3.9:** Triangular data points represent the experimental data in  $s - n(s)$  form. In this experiment (E1: 20 g/m), the cylinder is confined by MT [3]. The data are fitted in log-log space using Eq. 3.2 and represented by the dashed line. The three regions of the FSD are marked. The inset shows the offset connecting the fine-fragments region to intermediate size one. The two extended dashed lines shown in the inset are for better illustration of the offset.

Paper IV, Table-1 lists the experimental data sets analyzed and their configurations. Appendix B below lists the corresponding MPF data.

The experimental FSDs of the unconfined cylinders or those confined by the MT had to be changed somewhat from Eq. 3.1 above, because not only the intermediate size fragments but also the fine-fragments had the branching-merging type of size distributions with the power-law exponent of  $\alpha \sim 5/3$ , see Fig. 3.9 and also Fig. 1(b) in Paper IV. Hence, the first term, the crushing term in Eq. 3.1 above, is replaced by a second branching-merging term,

$$n(s)ds = C_1 s^{-\alpha} \exp\left(-\frac{s}{s_f}\right)ds + C_2 s^{-\alpha} \exp\left(-\frac{s}{s_i}\right)ds + C_3 \exp\left(-\frac{s}{s_b}\right)ds, \quad (3.2)$$

where the first term describes the size distribution of the fine-fragments and the second term describes the size distribution of the intermediate size fragments in an interval  $ds$  both formed by the branching-merging like mechanism since  $\alpha \sim 5/3$ .  $C_1, C_2$  and  $C_3$  are constants that determine the relative weight of the different fragment size regions.  $s_f$  is the transition size between the fines and the intermediate size fragments and  $s_i$  is the transition size between the intermediate size fragments and the boulders.

The fine- and the intermediate fragments size regions of the FSD are parallel with a power-law exponent of  $-5/3$  but separated by a vertical offset which was found to

be statistically significant for the sieving data that identified fragments even smaller than  $40\ \mu\text{m}$ . The location of the vertical offset varies between different blast sets, see Appendix E below. Appendix C and D below and Tables II-III in Paper IV list the statistical analysis for all the experiments listed in Table-I of Paper IV.

With HiDEM, we simulate small scale cubes of size  $3\ \text{mm} \times 3\ \text{mm} \times 3\ \text{mm}$  and  $6\ \text{mm} \times 6\ \text{mm} \times 6\ \text{mm}$  with a pre-defined pressurized edge crack in order to study the conditions for which fine-fragments are created due to branching and merging, see Fig. 4(a) and (b) in Paper IV. The smaller size cube is discretized with particles of size  $0.1\ \text{mm}$  and the larger cube with  $0.05\ \text{mm}$ ,  $0.08\ \text{mm}$ ,  $0.1\ \text{mm}$ , and  $0.2\ \text{mm}$ . The dynamic deposition algorithm is used to generate the geometrical configuration. We focus on the dynamics of a pressurized propagating edge-crack subjected to different lateral external stresses, both in tensile and in compressive direction, and the resultant FSDs, see  $P_{\text{conf}}$  in Fig. 3.10. A total of nine different lateral external stress levels are used.

At tensile or low compressive external stresses the FSD of the fine-fragments follows a branching-merging type of size distribution just like the sieved fragments from the experiments that are unconfined or confined by MT, i.e., the exponent of the size distribution is close to  $-5/3$ , see Table-IV and Fig. 5(a) and (b) in Paper IV.

Figure 5(d) in Paper IV shows the FSD for the large cube with the four different particle sizes. The exponential cut-off for the fines, independent of the particle size, appears at  $s_f \sim 10$ . This means a smaller fragment volume for the cube discretized with smaller particles compared to the larger ones. This shows that the fragment volume at the cross-over between fines and intermediate size scales with the grain size  $D_{\text{particle}}^3$ .

In addition, a simulation of a cube was made using the FCC lattice structure at zero lateral external stress level, i.e.  $P_{\text{conf}} = 0\ \text{MPa}$ . The resultant FSD, unlike the other cubes formed by the deposition algorithm, had in the fine-fragment region a crushing-shearing exponent of approximately  $-2.5$ .

### 3.5 Additional findings

We have extended the simulation results of the cube presented in Paper IV by introducing stress waves moving parallel to the direction of crack propagation, see  $P_{\text{fc}}$  and  $P_{\text{rc}}$  in Fig. 3.10.

Blasting cylindrical holes creates a compressive shock wave traveling outward in the radial direction. As the blast-hole expands outward, it will then induce tension in

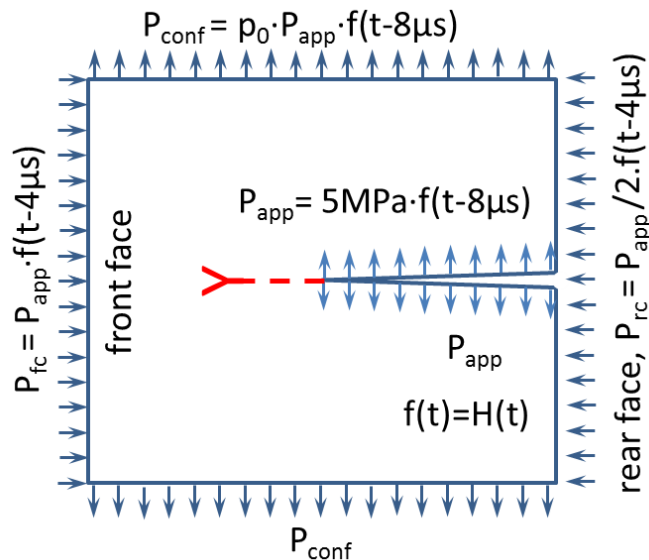


**Figure 3.10:** 2D schematic representation of the cube and the defined boundary conditions.

the tangential direction. The stress waves emanating from the blast-hole will sooner or later face a boundary or an interface between two dissimilar materials. Here, the specific acoustic impedance of the host rock, e.g.  $\rho c$ , and the boundary material, e.g.  $\rho'c'$ , plus the angle of wave incidence define the stress wave's interaction at the boundary such as transformation, transmission, reflection and refraction [93].

An effect of an outer periphery boundary confined by a higher impedance material, i.e.  $\rho c < \rho'c'$ , is a reflected, returning compressive wave, a lower impedance interface generates a returning tensile wave.

The former is simulated by adding a delayed compressive stress wave with an amplitude equal to the  $P_{\text{app}} = 5 \text{ MPa}$  on the small cube's front surface at  $4 \mu\text{s}$ , see  $P_{\text{fc}}$  in Fig. 3.10. Then the resultant fragmentation is computed at nine external stress levels given in Table-IV of Paper IV.

The effect of the returning compressive wave is to widen the crack path and to induce more crushing fines. One trivial reason is the sliding of the crack surfaces upon each other and forming more fine fragments through shear deformation. This occurs when the external compressive stresses are at a level to hold the two crack flanks together. However, when the external stresses are tensile or mildly compressive, the crushing effect of the returning compressive wave weakens. Consequently, the fine-fragment region of the FSDs barely changes.

In our simulations, the first significant change in the power-law exponent of the fine-fragment region emerges at  $P_{\text{conf}} = -0.1 P_{\text{app}}$  and it increases until where at  $P_{\text{conf}} = -0.2 P_{\text{app}}$  the power-law exponent takes the crushing value of -2.5

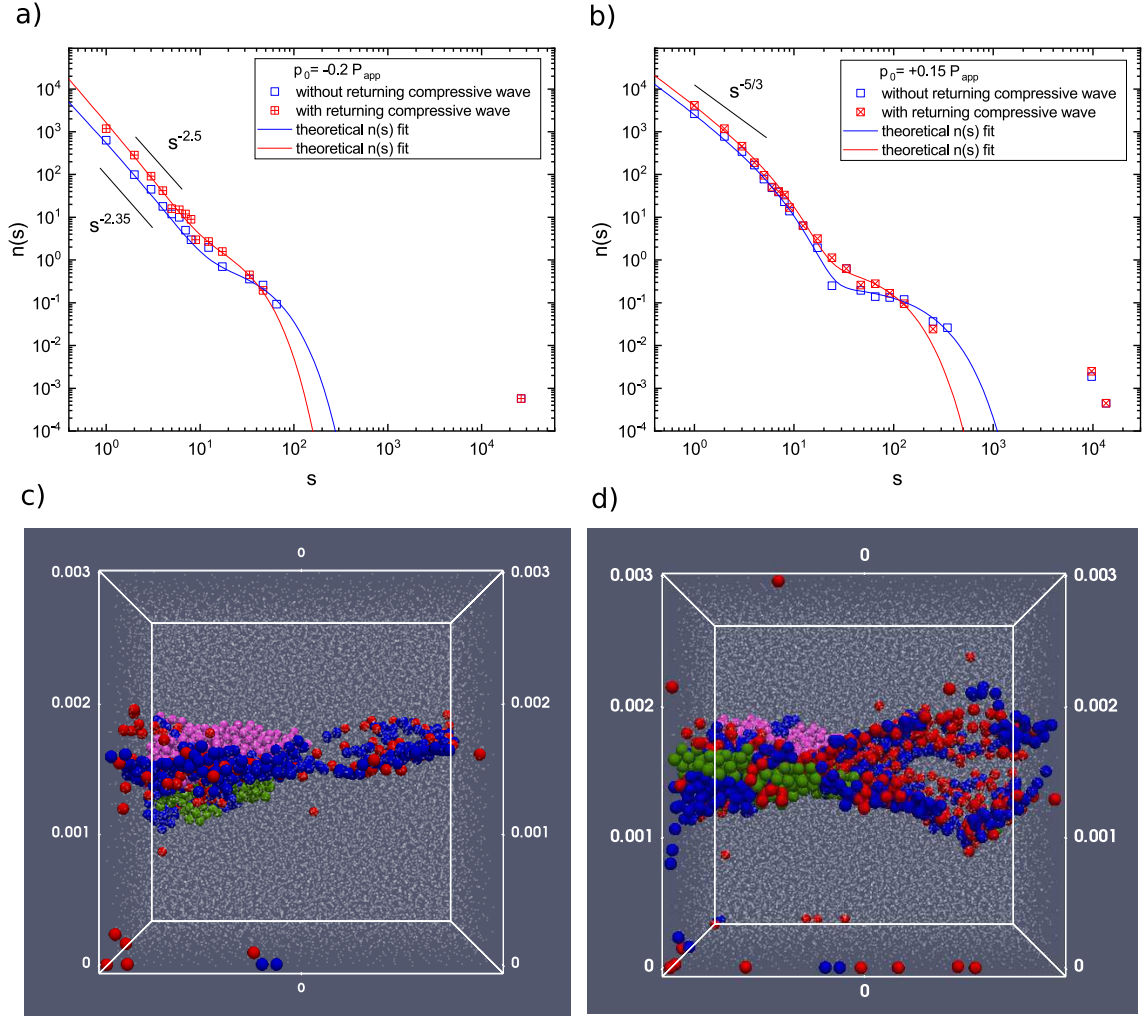


**Figure 3.11:** The FSDs of the dynamic crack propagation in the cube with a returning compressive stress wave a) for  $P_{\text{conf}} = -0.2 P_{\text{app}}$  and b) for  $P_{\text{conf}} = +0.15 P_{\text{app}}$ ; and for comparison, that of the cube at the same boundary conditions without the returning compressive stress wave in blue. The corresponding theoretical  $n(s)$  fits are shown by lines with the same color as the symbols. The lines with slope  $-5/3$ ,  $-2.5$  and  $-2.35$  are shown for comparison. The final fracture patterns for  $P_{\text{conf}} = -0.1 P_{\text{app}}$  in c) without the returning compressive stress wave and in d) the same with the returning compressive stress wave. The cube's particles are shown with white points for visibility of fragmentation. Red: single particle fragments, blue: fragments containing two particles, green: fragments containing 3 to 10 particles, pink: fragments containing 11 to 100 particles.

which means higher degree of crushing, see Fig. 3.11(a). For the cubes with  $P_{\text{conf}} \geq -0.1 P_{\text{app}}$  the FSDs show slight variations compared to the ones without the returning compressive wave, see Fig. 3.11(b) for  $P_{\text{conf}} = +0.15 P_{\text{app}}$ .

A possible consequence for the unstably propagating crack is to branch under the influence of the returning compressive wave. This may occur when the anisotropic biaxial compressive stress state surrounding the propagating crack tip become sufficiently large that shearing remains the only possibility for crack growth [94]. Figures 3.11(c)-(d) compare the crack development when  $P_{\text{conf}} = -0.1 P_{\text{app}}$ .

Another source for the bifurcation of a propagating crack is a returning tensile

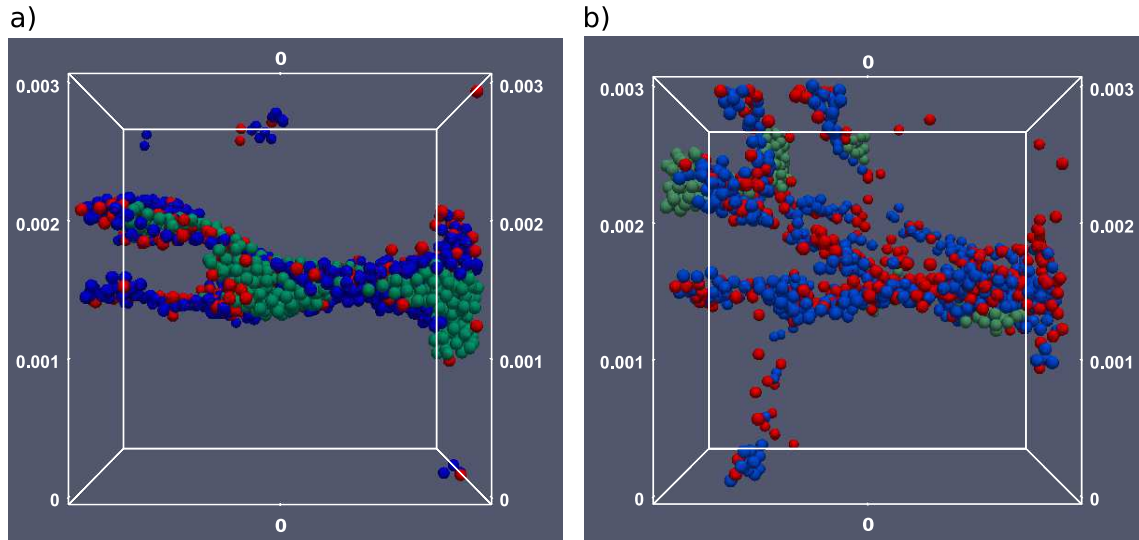


**Figure 3.12:** The final fracture patterns for  $P_{\text{conf}} = +0.05P_{\text{app}}$  in a) the cube without the returning tensile stress wave and in d) the same cube but with the returning tensile stress wave. Red: single particle fragments, blue: fragments containing two particles, green: fragments containing 3 to 10 particles.

wave from a free surface boundary. In most blasting experiments the outer periphery confinement has a lower impedance, which results in a returning tensile wave. This is simulated by adding a compressive stress on the rear face acting for a duration of  $0.5 \mu\text{s}$  after  $t = 4 \mu\text{s}$ , see  $P_{\text{rc}}$  in Fig. 3.10. The amplitude of the wave is chosen at a level to avoid spalling fractures near the frontal face. The returning tensile wave induces higher velocity of crack propagation and this could be a reason for the branching of the propagating crack. We have observed this in the cubes with  $P_{\text{conf}} = 0$  and  $P_{\text{conf}} = +0.05 P_{\text{app}}$ , see Fig. 3.12.

This page intentionally left blank.

## 4 Bibliography

- [1] Simulia, Dassault Systèmes Simulia Corp., Providence, RI, USA, *Abaqus Theory Manual, version 6.14*, 2014.
- [2] S. P. Michaux, *Analysis of fines generation in blasting*. PhD thesis, The University of Queensland, Julius Kruttschnitt Mineral Research Centre, Brisbane, Australia, 2005.
- [3] I. Kukolj, *Influence of dynamic fracture mechanisms during rock blasting on generation of fines*. PhD thesis, Montanuniversität Leoben, Department of Mineral Resources Engineering, Leoben, Austria, 2020. In preparation.
- [4] V. Svahn, “Generation of fines in bench blasting,” Lic. thesis, Chalmers University of Technology, Department of Geology, Göteborg, Sweden, 2003.
- [5] S. P. Michaux, “Sub-populations and patterns in blast induced fine fragmentation,” *Minerals Engineering*, vol. 22, no. 7-8, pp. 576–586, 2009.
- [6] M. M. D. Banadaki, *Stress-wave induced fracture in rock due to explosive action*. PhD thesis, University of Toronto, Department of Civil Engineering, Toronto, Canada, 2010.
- [7] L. Chi, *Shock compression and fractures in laboratory rock blasting*. PhD thesis, Norwegian University of Science and Technology, Department of Arctic Technology, Longyearbyen, Norway, 2018.
- [8] F. Ouchterlony and P. Moser, “On the branching-merging mechanism during dynamic crack growth as a major source of fines in rock blasting,” in *Proceedings of the 10th International Symposium on Rock Fragmentation by Blasting (Frag-Blast 10)* (P. K. Singh and A. Sinha, eds.), pp. 65–75, CRC Press, Balkema, 2012.
- [9] H. Steiner, “The significance of the Rittinger-equation in present-day comminution technology,” in *XVII International Mineral Proceeding Congress*, pp. 177–188, 1991.
- [10] W. A. Hustrulid, *Blasting principles for open pit mining: general design concepts*. Balkema, 1999.
- [11] D. E. Grady and M. E. Kipp, “Geometric statistics and dynamic fragmentation,” *Journal of Applied Physics*, vol. 58, no. 3, pp. 1210–1222, 1985.
- [12] J. A. Åström, F. Ouchterlony, R. Linna, and J. Timonen, “Universal dynamic fragmentation in D dimensions,” *Physical Review Letters*, vol. 92, no. 24, p. 245506, 2004.



- [13] J. A. Åström, R. P. Linna, J. Timonen, P. F. Møller, and L. Oddershede, “Exponential and power-law mass distributions in brittle fragmentation,” *Physical Review E*, vol. 70, no. 2, p. 026104, 2004.
- [14] R. Linna, J. A. Åström, and J. Timonen, “Dimensional effects in dynamic fragmentation of brittle materials,” *Physical Review E*, vol. 72, no. 1, p. 015601, 2005.
- [15] J. A. Åström, “Statistical models of brittle fragmentation,” *Advances in Physics*, vol. 55, no. 3-4, pp. 247–278, 2006.
- [16] H. J. Herrmann, F. K. Wittel, and F. Kun, “Fragmentation,” *Physica A: Statistical Mechanics and its Applications*, vol. 371, no. 1, pp. 59–66, 2006.
- [17] P. Kekäläinen, J. A. Åström, and J. Timonen, “Solution for the fragment-size distribution in a crack-branching model of fragmentation,” *Physical Review E*, vol. 76, no. 2, p. 026112, 2007.
- [18] H. Carmona, F. K. Wittel, F. Kun, and H. J. Herrmann, “Fragmentation processes in impact of spheres,” *Physical Review E*, vol. 77, no. 5, p. 051302, 2008.
- [19] G. Timár, F. Kun, H. Carmona, and H. Herrmann, “Scaling laws for impact fragmentation of spherical solids,” *Physical Review E*, vol. 86, no. 1, p. 016113, 2012.
- [20] G. Pál, I. Varga, and F. Kun, “Emergence of energy dependence in the fragmentation of heterogeneous materials,” *Physical Review E*, vol. 90, no. 6, p. 062811, 2014.
- [21] J. Franklin, J. Kemeny, and K. Girdner, “Evolution of measuring systems: A review,” in *Measurement of Blast Fragmentation (Fragblast 5)* (J. Franklin and T. Katsabanis, eds.), vol. 304, pp. 47–52, Balkema, Rotterdam, 1996.
- [22] F. Kun, I. Varga, S. Lennartz-Sassinek, and I. G. Main, “Approach to failure in porous granular materials under compression,” *Physical Review E*, vol. 88, no. 6, p. 062207, 2013.
- [23] F. K. Wittel, F. Kun, H. Herrmann, and B. Kröplin, “Breakup of shells under explosion and impact,” *Physical Review E*, vol. 71, no. 1, p. 016108, 2005.
- [24] D. Thornton, S. Kanchibotla, and I. Brunton, “Modelling the impact of rock-mass and blast design variation on blast fragmentation,” *Fragblast*, vol. 6, no. 2, pp. 169–188, 2002.
- [25] N. Djordjevic, “A two-component model of blast fragmentation,” in *Proceedings of the 6th International Symposium on Rock Fragmentation by Blasting*, pp. 213–219, The Southern African Institute of Mining and Metallurgy (SAIMM), Johannesburg, 1999.

- [26] F. Ouchterlony, “The Swebrec<sup>©</sup> function: linking fragmentation by blasting and crushing,” *Mining Technology*, vol. 114, no. 1, pp. 29–44, 2005.
- [27] D. Johansson, “Fragmentation and waste rock compaction in small-scale confined blasting,” Lic. thesis, Luleå University of Technology, Department of Civil, Mining and Environmental Engineering, Luleå, Sweden, 2008.
- [28] J. A. Sanchidrián, F. Ouchterlony, P. Segarra, and P. Moser, “Size distribution functions for rock fragments,” *International Journal of Rock Mechanics and Mining Sciences*, vol. 71, pp. 381–394, 2014.
- [29] S. Levy, *Exploring the physics behind dynamic fragmentation through parallel simulations*. PhD thesis, Swiss Federal Institute of Technology Lausanne (EPFL), School of Architecture, Civil and Environmental Engineering, Lausanne, Switzerland, 2010.
- [30] J. N. Reddy, *An introduction to the finite element method*. New York, USA: McGraw-Hill, 1993.
- [31] A. Raina and C. Linder, “Modeling crack micro-branching using finite elements with embedded strong discontinuities,” in *Proceedings of Applied Mathematics and Mechanics* (C. Wieners, ed.), vol. 10, pp. 681–684, Wiley Online Library, 2010.
- [32] N. A. Nordendale, *Modeling and simulation of brittle armors under impact and blast effects*. PhD thesis, Vanderbilt University, Department of Civil Engineering, Nashville, Tennessee, USA, 2013.
- [33] R. M. Brannon and S. Leelavanichkul, “Survey of four damage models for concrete,” *Sandia National Laboratories*, vol. 32, no. 1, pp. 1–80, 2009.
- [34] J. C. Simo and J. Ju, “Strain- and stress-based continuum damage models—I. formulation,” *International Journal of Solids and Structures*, vol. 23, no. 7, pp. 821–840, 1987.
- [35] R. Faria and J. Oliver, *A rate dependent plastic-damage constitutive model for large scale computations in concrete structures*. Barcelona, Spain: Barcelona Centro Internacional de Métodos Numéricos en Ingeniería, 1993.
- [36] R. Talreja, “A continuum mechanics characterization of damage in composite materials,” *Proceedings of the Royal Society of London. A. Mathematical and Physical Sciences*, vol. 399, no. 1817, pp. 195–216, 1985.
- [37] J. Chaboche, “Continuum damage mechanics,” *Journal of Applied Mechanics*, vol. 55, no. 1, pp. 59–64, 1988.
- [38] J. Mazars and G. Pijaudier-Cabot, “Continuum damage theory—application to concrete,” *Journal of Engineering Mechanics*, vol. 115, no. 2, pp. 345–365, 1989.

- [39] V. Lubarda, D. Krajcinovic, and S. Mastilovic, “Damage model for brittle elastic solids with unequal tensile and compressive strengths,” *Engineering Fracture Mechanics*, vol. 49, no. 5, pp. 681–697, 1994.
- [40] M. Cervera, J. Oliver, and R. Faria, “Seismic evaluation of concrete dams via continuum damage models,” *Earthquake Engineering & Structural Dynamics*, vol. 24, no. 9, pp. 1225–1245, 1995.
- [41] R. Faria, J. Oliver, and M. Cervera, “Modeling material failure in concrete structures under cyclic actions,” *Journal of Structural Engineering*, vol. 130, no. 12, pp. 1997–2005, 2004.
- [42] J. Lubliner, J. Oliver, S. Oller, and E. Oñate, “A plastic-damage model for concrete,” *International Journal of Solids and Structures*, vol. 25, no. 3, pp. 299–326, 1989.
- [43] S. Yazdani and H. Schreyer, “Combined plasticity and damage mechanics model for plain concrete,” *Journal of Engineering Mechanics*, vol. 116, no. 7, pp. 1435–1450, 1990.
- [44] M. di Prisco and J. Mazars, “Crush-crack: a non-local damage model for concrete,” *Mechanics of Cohesive-frictional Materials: An International Journal on Experiments, Modelling and Computation of Materials and Structures*, vol. 1, no. 4, pp. 321–347, 1996.
- [45] J. Lee and G. L. Fenves, “Plastic-damage model for cyclic loading of concrete structures,” *Journal of Engineering Mechanics*, vol. 124, no. 8, pp. 892–900, 1998.
- [46] R. Faria, J. Oliver, and M. C. Ruiz, *On isotropic scalar damage models for the numerical analysis of concrete structures*. Barcelona, Spain: Barcelona Centro Internacional de Métodos Numéricos en Ingeniería, 2000.
- [47] E. Hansen, K. Willam, and I. Carol, “A two-surface anisotropic damage/plasticity model for plain concrete,” in *Proceedings of Framcos-4 Conference Paris, Fracture Mechanics of Concrete Structures* (R. de Borst, ed.), pp. 549–556, Balkema, Lisse, 2001.
- [48] L. Pelà, *Continuum damage model for nonlinear analysis of masonry structures*. PhD thesis, Università degli Studi di Ferrara, Department of Engineering, Ferrara, Italy, 2009.
- [49] P. Grassl, D. Xenos, U. Nyström, R. Rempling, and K. Gylltoft, “CDPM2: A damage-plasticity approach to modelling the failure of concrete,” *International Journal of Solids and Structures*, vol. 50, no. 24, pp. 3805–3816, 2013.
- [50] N. Ziad, *Elasto-plastic and damage modeling of reinforced concrete*. PhD thesis, Louisiana State University, Department of Civil & Environmental Engineering,

- Baton Rouge, Louisiana, USA, 2008.
- [51] C. Yi, J. Sjöberg, D. Johansson, and N. Petropoulos, “A numerical study of the impact of short delays on rock fragmentation,” *International Journal of Rock Mechanics and Mining Sciences*, vol. 100, pp. 250–254, 2017.
  - [52] Z. Zhu, B. Mohanty, and H. Xie, “Numerical investigation of blasting-induced crack initiation and propagation in rocks,” *International Journal of Rock Mechanics and Mining Sciences*, vol. 44, no. 3, pp. 412–424, 2007.
  - [53] G. Ma and X. An, “Numerical simulation of blasting-induced rock fractures,” *International Journal of Rock Mechanics and Mining Sciences*, vol. 45, no. 6, pp. 966–975, 2008.
  - [54] L. Hedjazi, C. Martin, S. Guessasma, G. Della Valle, and R. Dendievel, “Application of the discrete element method to crack propagation and crack branching in a vitreous dense biopolymer material,” *International Journal of Solids and Structures*, vol. 49, no. 13, pp. 1893–1899, 2012.
  - [55] A. Balakrishnan, P. Pizette, and C. Martin, “Discrete simulation of the consolidation of nano-sized aggregated powders,” *AIP Conference Proceedings*, vol. 1145, no. 1, pp. 105–108, 2009.
  - [56] J. A. Åström, T. Riikilä, T. Tallinen, T. Zwinger, D. Benn, J. C. Moore, and J. Timonen, “A particle based simulation model for glacier dynamics,” *The Cryosphere*, vol. 7, no. 5, pp. 1591–1602, 2013.
  - [57] H. A. Carmona, F. K. Wittel, and F. Kun, “From fracture to fragmentation: Discrete element modeling,” *The European Physical Journal Special Topics*, vol. 223, no. 11, pp. 2369–2382, 2014.
  - [58] F. Donze, J. Bouchez, and S. Magnier, “Modeling fractures in rock blasting,” *International Journal of Rock Mechanics and Mining Sciences*, vol. 34, no. 8, pp. 1153–1163, 1997.
  - [59] C. Yi and D. Johansson, “Discrete element modelling of blast fragmentation of a mortar cylinder,” in *International Symposium on Rock Fragmentation by Blasting (Fragblast 11)*, pp. 793–798, The Australasian Institute of Mining and Metallurgy, Carlton Victoria, 2015.
  - [60] Z. Han, D. Weatherley, and R. Puscasu, “Application of discrete element method to model crack propagation,” in *13th ISRM International Congress of Rock Mechanics*, (Montreal, Canada), International Society for Rock Mechanics, 2015.
  - [61] F. K. Wittel, H. A. Carmona, F. Kun, and H. J. Herrmann, “Mechanisms in impact fragmentation,” *International Journal of Fracture*, vol. 154, pp. 105–117, 2008.

- [62] Y. Wang and F. Alonso-Marroquín, “DEM simulation of comminution: Fragmentation and size distribution,” *AIP Conference Proceedings*, vol. 1145, no. 1, pp. 863–866, 2009.
- [63] F. K. Wittel, “Single particle fragmentation in ultrasound assisted impact comminution,” *Granular Matter*, vol. 12, no. 4, pp. 447–455, 2010.
- [64] S. Hentz, F. V. Donzé, and L. Daudeville, “Discrete element modelling of concrete submitted to dynamic loading at high strain rates,” *Computers & Structures*, vol. 82, pp. 2509–2524, 2004.
- [65] J. Kozicki, *Application of discrete models to describe the fracture process in brittle materials*. PhD thesis, Gdańsk University of Technology, Department of Civil and Environmental Engineering, Gdańsk, Poland, 2007.
- [66] L. Hedjazi, C. Martin, S. Guessasma, G. Della Valle, and R. Dendievel, “Application of the discrete element method to crack propagation and crack branching in a vitreous dense biopolymer material,” *International Journal of Solids and Structures*, vol. 49, no. 13, pp. 1893–1899, 2012.
- [67] S. Cook, J. A. Åström, T. Zwinger, B. K. Galton-Fenzi, J. S. Greenbaum, and R. Coleman, “Modelled fracture and calving on the totten ice shelf,” *The Cryosphere*, vol. 12, no. 7, pp. 2401–2411, 2018.
- [68] D. I. Benn and J. A. Åström, “Calving glaciers and ice shelves,” *Advances in Physics: X*, vol. 3, no. 1, p. 1513819, 2018.
- [69] J. P. Morris, M. Rubin, G. Block, and M. Bonner, “Simulations of fracture and fragmentation of geologic materials using combined fem/dem analysis,” *International Journal of Impact Engineering*, vol. 33, pp. 463–473, 2006.
- [70] A. Fakhimi and M. Lanari, “DEM–SPH simulation of rock blasting,” *Computers and Geotechnics*, vol. 55, pp. 158–164, 2014.
- [71] C. Yi, D. Johansson, U. Nyberg, and J. Sjöberg, “Numerical simulation for the influence of delay time on the rock fragmentation,” in *International Symposium on Rock Fragmentation by Blasting (Fragblast 10)*, pp. 213–220, CRC Press, Balkama, 2012.
- [72] C. Yi, J. Sjöberg, and D. Johansson, “Numerical modelling for blast-induced fragmentation in sublevel caving mines,” *Tunnelling and Underground Space Technology*, vol. 68, pp. 167–173, 2017.
- [73] P. Moser, “Less fines in aggregate and industrial minerals production—results of a european research project,” in *Third EFEE World Conference of Explosives and Blasting* (R. Holmberg, ed.), (Brighton, UK), pp. 567–574, EFEE, UK, 2005.

- [74] J. Herbst and W. Pate, “Dynamic simulation of size reduction operations from mine-to-mill,” in *Mine to Mill: Exploring the Relationship Between Mining and Mineral Processing Performance*, p. 243, Australasian Institute of Mining and Metallurgy, Carlton, Victoria, Australia, 1998.
- [75] N. Djordjevic, “Origin of blast-induced fines,” *Mining Technology*, vol. 111, no. 2, pp. 143–146, 2002.
- [76] I. Onederra, S. Esen, and A. Jankovic, “Estimation of fines generated by blasting – applications for the mining and quarrying industries,” *Mining Technology*, vol. 113, no. 4, pp. 237–247, 2004.
- [77] F. Ouchterlony and J. Sanchidrián, “A review of development of better prediction equations for blast fragmentation,” *Journal of Rock Mechanics and Geotechnical Engineering*, vol. 11, no. 5, pp. 1094 – 1109, 2019.
- [78] B. Sinha, K. H. Gerstle, and L. G. Tulin, “Stress-strain relations for concrete under cyclic loading,” *ACI Structural Journal*, vol. 61, no. 2, pp. 195–212, 1964.
- [79] H. W. Reinhardt, “Fracture mechanics of an elastic softening material like concrete,” *Heron*, pp. 1–42, 1984.
- [80] L. Jason, G. Pijaudier-Cabot, A. Huerta, and S. Ghavamian, “Damage and plasticity for concrete behavior,” in *Proceedings of European Congress on Computational Methods in Applied Sciences and Engineering (ECCOMAS)* (P. Neittaanmäki, T. Rossi, S. Korotov, E. Oñate, J. Périaux, and D. Knörzer, eds.), pp. 303–328, CIMNE, Jyväskylä, Finland, 2004.
- [81] A. Hillerborg, M. Modéer, and P.-E. Petersson, “Analysis of crack formation and crack growth in concrete by means of fracture mechanics and finite elements,” *Cement and Concrete Research*, vol. 6, no. 6, pp. 773–781, 1976.
- [82] J. A. Åström, P. S. Kumar, I. Vattulainen, and M. Karttunen, “Strain hardening, avalanches, and strain softening in dense cross-linked actin networks,” *Physical Review E*, vol. 77, no. 5, p. 051913, 2008.
- [83] J. Åström and J. Timonen, “Impact fracture of a three-dimensional cube with quenched disorder,” *Physical Review E*, vol. 59, no. 4, p. 4650, 1999.
- [84] L. Triviño, B. Mohanty, and A. Munjiza, “Seismic radiation patterns from cylindrical explosive charges by analytical and combined finite-discrete element methods,” in *Proceedings of the Ninth International Symposium on Rock Fragmentation by Blasting (Fragblast 9)*, vol. 9, pp. 415–26, CRC Press, Balkama, 2009.
- [85] I. Kukolj, A. Irvani, and F. Ouchterlony, “Filming blast fragmentation of rock and mortar cylinders,” in *Proceedings of 12th International Symposium for Rock*

- Fragmentation by Blasting (Fragblast 12)* (H. Schunnesson and D. Johansson, eds.), pp. 483–494, Luleå University of Technology, Luleå, 2018.
- [86] T. J. Holmquist, G. R. Johnson, and W. H. Cook, “A computational constitutive model for concrete subjected to large strains, high strain rates and high pressures,” in *Proceedings of the 14th International Symposium on Ballistics*, vol. 2, pp. 591–600, ADPA, Arlington, 1993.
- [87] G. Johnson and T. Holmquist, “A computational constitutive model for brittle materials subjected to large strains, high strain rates and high pressures,” *Shock Waves and High-Strain-Rate Phenomena in Materials*, pp. 1075–1081, 1992.
- [88] G. R. Johnson, T. J. Holmquist, and S. R. Beissel, “Response of aluminum nitride (including a phase change) to large strains, high strain rates, and high pressures,” *Journal of Applied Physics*, vol. 94, no. 3, pp. 1639–1646, 2003.
- [89] G. R. Johnson and T. J. Holmquist, “An improved computational constitutive model for brittle materials,” *AIP Conference Proceedings*, vol. 309, no. 1, pp. 981–984, 1994.
- [90] D. Johansson, *Effects of confinement and initiation delay on fragmentation and waste rock compaction*. PhD thesis, Luleå University of Technology, Department of Civil, Mining and Environmental Engineering, Luleå, Sweden, 2011.
- [91] T. Riikilä, T. Tallinen, J. Åström, and J. Timonen, “A discrete-element model for viscoelastic deformation and fracture of glacial ice,” *Computer Physics Communications*, vol. 195, pp. 14 – 22, 2015.
- [92] H. Grimshaw, “The fragmentation produced by explosive detonated in stone blocks,” *Mechanical Properties of Non-Metallic Brittle Materials*, pp. 380–388, 1958.
- [93] J. S. Rinehart, *Stress transients in solids*. New Mexico, USA: HyperDynamicS, 1975.
- [94] P. Isaksson, *On crack growth under compressive stresses*. PhD thesis, Luleå University of Technology, Department of Mechanical Engineering, Luleå, Sweden, 2001.
- [95] J. A. Åström. personal communication.
- [96] D. Watstein, “Effect of straining rate on the compressive strength and elastic properties of concrete,” *Journal of the American Concrete Institut*, vol. 49, no. 8, pp. 729–744, 1953.
- [97] H. W. Reinhardt, P. Rossi, and J. G. M. van Mier, “Joint investigation of concrete at high rates of loading,” *Materials and Structures*, vol. 23, no. 3, pp. 213–216, 1990.

- [98] F. M. Mellinger and D. L. Birkimer, “Measurements of stress and strain on cylindrical test specimens of rock and concrete under impact loading,” Tech. Rep. 4-46, U.S. Army Corps of Engineers, Ohio River Div Labs Cincinnati, 1966.
- [99] R. Fu, B. A. Baudet, B. Madhusudhan, and M. Coop, “A comparison of the performances of polypropylene and rubber fibers in completely decomposed granite,” *Geotextiles and Geomembranes*, vol. 46, no. 1, pp. 22 – 28, 2018.



This page intentionally left blank.

**Paper I:**

**Finite element modeling of blast induced fractures of cylinders of mortar and rock**

This page intentionally left blank.

# Modelling blast fragmentation of cylinders of mortar and rock

A. Iravani, I. Kukulj, F. Ouchterlony

*Dept. Mineral Resources Engineering, Montanuniversitaet Leoben, 8700 Leoben, Styria, Austria*

T. Antretter

*Institute of Mechanics, Montanuniversitaet Leoben, 8700 Leoben, Styria, Austria*

J. Åström

*CSC-IT Center for Science, P.O. Box 405, 02101, Espoo, Finland*

**ABSTRACT:** This paper investigates the blast fragmentation of a mortar cylinder by numerical simulations. The aim of the project is to understand the underlying mechanisms causing blast induced fines. Two numerical methods: Finite and Discrete Element Methods (FEM, DEM) with explicit time integration were used and the results were compared with the results of blasting tests. In FEM thin cylindrical disk ( $\text{Ø}140$  mm) with 1 layer of 3D continuum elements and in DEM a 3D cylinder with  $\text{Ø}140 \times 200$  mm were modelled. They were loaded by a pressure evolution acting on borehole wall. Both models reproduce realistic crack patterns consisting of through-going radial cracks, with branching and interconnecting cracks, around a crushed zone at the borehole. The FEM models, however, for slight changes contain unrealistic areas of deleted elements, whereas the DEM models were more robust and delivered realistic fragment size distribution of the expected Swebrec function type.

## 1 INTRODUCTION

In mining and quarrying, blasting is the main method for rock excavation. The explosives are placed in series of boreholes with a predetermined amount and detonation delay time, aiming at achieving a manageable muck pile and a desired fragment size distribution (FSD). An under- or over-charged boreholes are often a financial liability for the companies. That is, in addition to the time and resources costs, the resultant fragment sizes might be smaller than the acceptable size for the processing (recovery) units. Even in well-designed blasting rounds fine particles are generated. For example, in EU quarries around 2.5 billion tons of rocks are annually blasted of which 10 – 15 % is unsellable waste fine particles (Moser 2003).

There are many theories on the source of fine particles due to rock blasting, e.g. the traditional crushed zone model (CZM) that assumes fines are originating from an annular crushed zone around the blast hole, the two component model (TCM) developed by Djordjevic (1999, 2002) and further improvements of the CZM by Onederra et al. (2004) who assumed that the fine particles are originating from a star-shaped crushed zone. Another yet plausible one is that the fines are generated by a mechanism involving dynamic crack branching and merging (Ouchterlony & Moser 2012).

By the advancement of computation power and numerical tools, many researches have started to in-

vestigate blast induced damage, dynamic crack branching and merging and thus fragmentation through numerical simulations. Cho & Kaneko (2004) e.g. studied the dynamic fracture process of a two dimensional disk with a borehole at its center subjected to different dynamic wave forms, different rise time and decay time of the pressure function, peak value of the applied pressure and stress loading rates. Zhu et al. (2007) studied blast induced damage and dynamic crack propagation of a circular rock model with a centrally located borehole using the finite element method (FEM) code Autodyn 2D. Ma & An (2008) implemented a Johnson-Holmquist (JH) constitutive model into the commercial FEM code LS-Dyna and studied the borehole blast induced rock fracture and fracture pattern under different circumstances i.e. different stress loading rates, effect of free surface and joint plane, pre-existing compressive stress, notches, etc.. Wang & Alonso-Marroquín (2009) used the 3D discrete element method (DEM) to model the fracture process and the size distribution in a sphere resulting from different impact rates. Banadaki & Mohanty (2010) investigated the crushed zone, radial and spalling cracks of cylindrical Barre and Laurentian granites subjected to blast load using the built-in JH2 material model in Autodyn with explicit time integration scheme, Nordendale (2013) studied the damage induced in ultra-high strength concrete and ashcrete panels of size  $305 \text{ mm} \times 305 \text{ mm} \times 27 \text{ mm}$  by ballistic impact.

Recently Yi & Johansson (2015) used DEM to simulate blast fragmentation of mortar cylinders with a central borehole. The effect of dynamic loading on the response of rock-type materials was studied. Even if the simulated process as a whole is realistic the resulting blast induced damages and crack patterns are not. Examples of simplified behavior are i) radially straight symmetrical crack patterns, ii) crack propagation without deviation from the initial nucleated direction, iii) cracks without branching and merging, and iv) fragment size distributions (FSD) curves that do not quite look like real ones. In this paper we hope to improve on the work by Yi & Johansson (2015) by taking into account the nucleation, propagation and branching of cracks around the explosion cavity during a blasting event.

We present results from numerical simulations of the blast loading of confined mortar cylinders. These are compared with post mortem CT scans and High Speed Video (HSV) images of dynamic cracks on the specimen's end surface to judge how realistic the simulations are. The work is the first part of the FWF project P 27594-N29 'Fine particles generated by dynamic crack propagation, as in blasting of rock like materials', which started July 1<sup>st</sup>, 2015, see the work presented by Kukolj et al. (2018). It has been suggested that branching-merging of growing cracks is a major source of such fines (Ouchterlony & Moser 2012) and before modeling of these local crack tip occurrences can take place, it is important to have a reliable overall model.

## 2 TYPICAL EXPERIMENTAL RESULTS

The experimental procedure includes blasting a PETN (pentaerythritol tetranitrate) cord of certain charge concentration, i.e. here 6 g/m, 12 g/m and 20 g/m, inside the borehole of a mortar cylinder, which is radially surrounded by a damping layer inside a blasting chamber.

The mortar cylinder production follows a recipe similar to the one from the researches of Johansson & Ouchterlony (2011) and Schimek et al. (2013). The mortar cylindrical structure were produced with dimensions of  $\text{Ø}140 \times 280$  mm and  $\text{Ø}150 \times 300$  mm and the borehole diameter of  $\text{Ø}_{\text{borehole}} = 10$  mm. A plug was fitted at the frontal cylinder-face, 25-50 mm deep inside the borehole, to hinder the blast-generated gas to rush in-between the window and the cylinder and to protect the camera from the detonation-caused flash inside the borehole.

The blasting chamber includes four concrete segments and employs the "impulse trap" concept (Sun 2013). The damping layer, protective window and the four segments of the blasting chamber directly affect boundary conditions reducing the spalling effect and circumferential counter-directed cracks, which could interfere and obscure cracks that

propagate towards the cylinder's circumference (Rossmannith et al. 2005). The damping layer and the window are designed to impede radial and axial blast-induced expansion and, hence, provide more uniform radial crack propagation along the cylinder's axis.

The blast tests used the HSI camera Imager HS 4M (LA Vision) to capture the crack propagation at frame rates of 20,000-37,000 fps at image resolution of  $256 \times 256$  pixels and  $336 \times 336$  pixels.

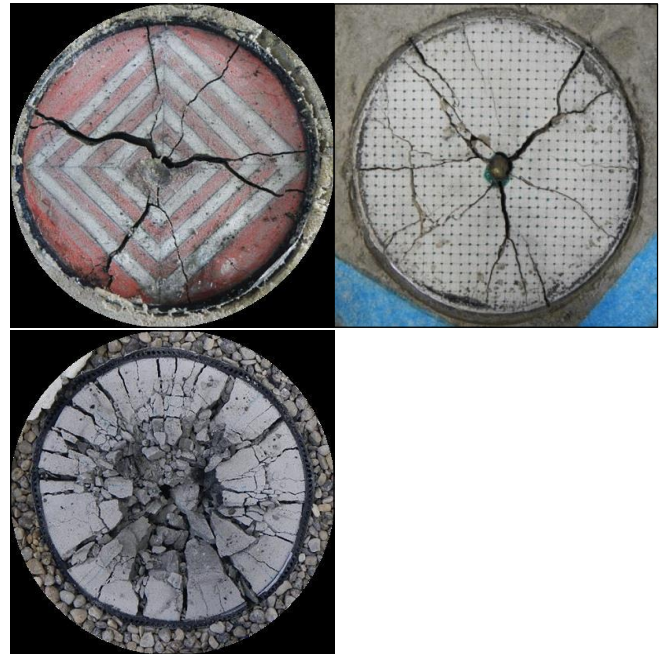


Figure 1. Post-mortem crack network at the front end face of the mortar cylinder blasted with 6 g/m, 12 g/m and 20 g/m of PETN from to left.

## 3 MODEL SETUP

### 3.1 *Abaqus/Explicit and CDP*

The finite element method (FEM) code Abaqus (Simulia, 2014) using an explicit time integration scheme has been used, which is a suitable choice for high speed impact processes. The constitutive model used in this study is Concrete Damage Plasticity model (CDP) (Hillerborg et al. 1976, Lubliner et al. 1989, Lee & Fenvas 1998), a built-in model in Abaqus. The detailed description of CDP is given in the Abaqus analysis user's guide V. 6.14, section 23.6.3. It requires six material constants to model the inelastic behavior of concrete/mortar in addition to rate dependent data in the dynamic range. They are an elastic modulus ( $E$ ), a Poisson's ratio  $\nu$ , a dilation angle  $\psi$ , a flow potential eccentricity  $\epsilon$ , the ratio of initial equibiaxial compressive yield stress to that of the uniaxial compressive stress  $\sigma_{b0}/\sigma_{c0}$ , and the ratio of the second stress invariant on the tensile meridian to that on the compressive meridian at initial yield

for any given value of the pressure invariant  $K_c$  (Simulia, 2014). Jankowiak & Lodygowski (2005) have provided a set of calibrated data for the CDP model. These data have been used as the reference in the quasi-static regime.

The mortar structure was modelled as a cylindrical disk with thickness  $H = 1$  mm,  $\varnothing_{\text{out}} = 140$  mm and  $\varnothing_{\text{inside}} = 6$  mm. On the periphery of the cylinder quiet boundary conditions were used. Three dimensional linear hexahedral stress elements with reduced integration points (C3D8R) and 3D infinite elements (AC3D8R) were used for discretization of the mortar and the peripheral structure as the boundary condition of the confined cylinder. A top view of the model setup and the mesh is illustrated in Figure 2. A summary of the mesh details are given in Table 1.

Table 1. Model's mesh information.

Element type	Element name	Number of elements in the model	Global mesh size mm
Stress elements	C3D8R	40448	1
Infinite elements	AC3D8R	628	Not applicable

The strain-rate dependent failure surface of the CDP model has been developed on the basis of quasi-static data. The Huh-Kang model (2002) was used as the rate form. The peripheral material enclosing the mortar structure was modelled in a simplified way with an elastic material representation called quiet boundary condition, for which the Young's modulus and the Poisson's ratio are identical to those of the mortar structure. This allows us to investigate the crack propagation, branching and merging. Otherwise, the shock waves strike the outer boundary reflect as tensile waves developing rings of tensile damage preventing the propagating cracks originating around the borehole from being distinguishable. The shock waves passing through the finite elements degrade their elastic modulus including those on the periphery connected to the infinite elements. This breaks the initially defined impedance match between the mortar structure and the outer boundary. This could be observed as local reflections of stress waves on the periphery of the mortar structure.

The blast load is of the type of pressure-time history which is applied radially on the borehole wall. The borehole pressure function of Trivino & Mohanty (2009) was implemented:

$$P(t) = P_{\text{peak}} \cdot e^{-\{b_u (t-t_u)\}^{2n}} \cdot e^{-\{b_d (t-t_d)\}^2} \quad (1)$$

where  $b_u$ ,  $t_u$ ,  $n$ ,  $b_d$ , and  $t_d$  define the rising up and decaying down of the pressure function. The parameter  $b_u$  is chosen as a fraction of  $b_d$ :  $b_u = b_d/b_{\text{ratio}}$  with  $b_{\text{ratio}} \geq 2$  (Trivino & Mohanty, 2009). Here,  $b_d$  and  $b_u$  are related to the maximum decay rate,  $m_d$ , and maximum

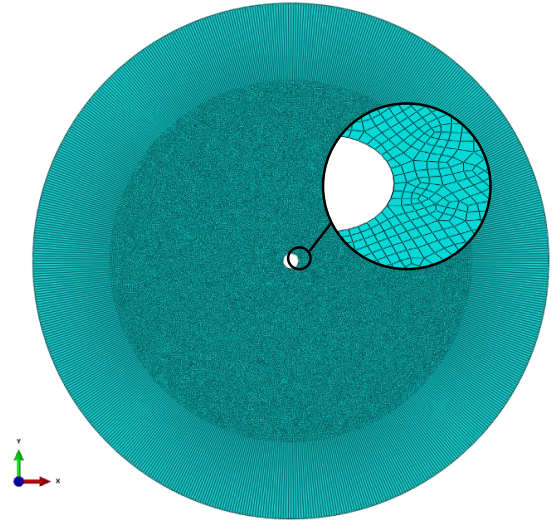


Figure 2. Top view of the model and the magnified discretization around the borehole.

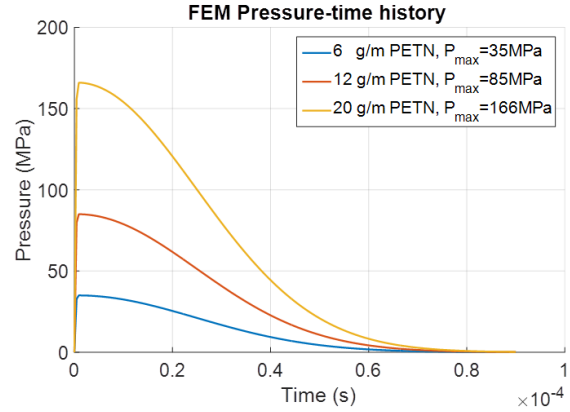


Figure 3. Pressure time loading history with three peak pressures of 35 MPa, 85 MPa and 166 MPa.

imum raise rate,  $m_u$ , respectively. Finally, the parameters  $t_u$  and  $t_d$  are (Trivino & Mohanty, 2009):

$$t_u = [-\ln(\alpha_1)]^{1/2n} / b_u \quad (2)$$

$$t_d = \{[-\ln(\alpha_1)]^{1/2n} - [-\ln(1 - \alpha_2)]^{1/2n}\} / b_u \quad (3)$$

where  $\alpha_1$  and  $\alpha_2$  are the approximate error at  $t = 0$  and  $t = t_{\text{peak-pressure}}$ .

The peak pressures of 166 MPa, 85 MPa and 35 MPa equivalent to 20 g/m, 12 g/m and 6 g/m of PETN were used (Sanchidrián, 2017). In all three loading levels, the pressure rise time to peak is approximately 1  $\mu\text{s}$ . Figure 3 shows the pressure-time history of the loading levels.

### 3.1.1 Continuum finite element models calibrations

Application of the FEM in high speed dynamical processes consisting of large number of fractures has limitations (Nordendale 2013, Donzé et al. 2009). A material model with a strain softening behavior, here CDP, greatly increases the probability for an

unstable solution. The instability in these dynamical simulations show up as an elemental distortion before a mature simulation result is achieved. The elements experiencing large magnitudes of damage have lost almost all of their stiffness, becoming soft and extremely distortable even at negligible levels of external loading. These elements are the main source of unstable simulation results. Here, a solution-dependent element deletion algorithm accompanies the 3D linear hexahedral elements. In CDP, as described in the Abaqus analysis user's guide V. 6.14, scalar damage grows by increasing values of accumulated plastic strain and is separated into tension and compression. The deletion algorithm was developed in the Abaqus VUSDFLD subroutine. The finite elements whose tensile equivalent plastic strain reaches a pre-determined value, here 98% of total damage (100%), cease to carry load using this subroutine. This, however, would cause an error when dealing with the conservation of the mass of the system. Nordendale (2013) has stated on this issue: *"The removal of the elements would have to take place early in the analysis in order to show the appropriate failure scenario leading to model simulating a weaker target than in real life and significantly increase the computation time."*

The use of the CDP model in a high speed dynamical process lacks an equation of state (EoS) to describe the pressure-volume relation. As a consequence, the volumetric strain of a finite element could increase extremely, i.e. there is no volumetric strain locking limit, as a result of enforcing a sudden large value of hydrostatic stress (first invariant of stress tensor) level (Nordendale 2013). In Abaqus/Explicit, the linear and quadratic bulk viscosity parameters, Rayleigh material damping and mass scaling were used to compensate for these nonlinear effects of compaction.

The linear and quadratic bulk viscosity damp oscillations associated with volumetric straining. The former damps transverse and the latter damps longitudinal oscillations (Simulia, 2014). The fixed- and the variable-mass scaling define an element stable time increment at the beginning and during the calculation (the detailed description is in the Abaqus analysis user's guide V. 6.14, section 11.6). These calibration parameters not only help to stabilize the FEM results against the aforementioned issues, but also are a remedy for the results' calibration of the explicit time integration.

In addition to the 2D models with Abaqus/Explicit, complete 3D models of the cylinder, i.e.  $H = 280$  mm, were simulated. In these, similar instabilities as in the 2D models appeared; in addition, they showed unrealistic crack growth patterns. The material model calibration became extremely difficult and time consuming. As an exa-

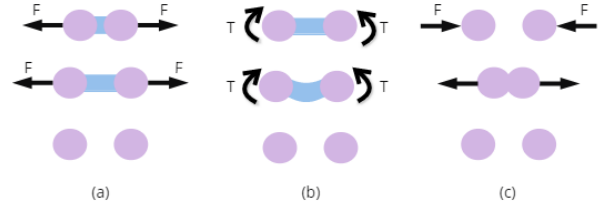


Figure 4. Failure mechanisms due to (a) tension and (b) bending; (c) particles come into contact experiencing repulsive force (Åström et al. 2013)

mple damping parameters that stabilized one model failed to stabilize models that were almost identical. Therefore, we have limited the application of FEM-Abaqus to the 2D models and addressed the 3D modelling using a discrete element code described in the next section. The FEM models required approximately 6 minutes of calculation time using 48 interconnected cores of Intel(R) Xeon(R) CPU E5-2667 v1 @ 2.90GHz.

### 3.2 HiDEM

The 3D modelling was made with the HiDEM discrete element code (Åström 2006, Åström et al. 2013) for several reasons. Firstly the stability problems encountered with Abaqus made the progress toward the goal 3D modeling very slow. Secondly it could be said that a suitable DEM code will probably have less problems with highly dynamic processes (Hedjazi et al. 2012) and thirdly post-processing tools for visualizing e.g. internal cracking and fragmentation, adapted to our problem were already available.

The particles in HiDEM are rigid spheres. They are arranged in a Face-Centered-Cubic (FCC) lattice. The contacts between the particles were modelled using massless beams. The interaction potential between two particles was defined by the Euler-Bernoulli (EB) beam. Åström et al. (2013) gave the elastic energy of beams. The beams break because of tension, shear or bending beyond the fracture limit (Åström et al. 2013, Fig. 4).

At time  $t = 0$  s, the particles are arranged and packed to form the desired cylindrical specimen. Then, the connections between particles are defined using the elastic beams. The equation of motion can be represented by the simplified, mixed matrix and index notation form:

$$\mathbf{M}\ddot{\mathbf{r}}_i + \mathbf{C}\dot{\mathbf{r}}_{ij} + \sum_j \mathbf{K}\mathbf{r}_{ij} = \mathbf{F}_i \quad (4)$$

where  $\mathbf{M}$  = mass-matrix containing the masses and the moments of inertia of the particles;  $\mathbf{r}_i$ ,  $\dot{\mathbf{r}}_i$  and  $\ddot{\mathbf{r}}_i$  = the position, velocity and acceleration vectors of the particle  $i$  including the rotation components;  $\mathbf{r}_{ij}$  = the corresponding position vectors for all the particles  $j$  that are connected to the particle  $i$ ;  $\mathbf{C}$  = the damping

matrix;  $\mathbf{K}$  = the stiffness matrix; and  $F_i$  = the sum of the other forces acting on the particle  $i$ . The stiffness matrix for linear elastic EB beams under small deformation is given by Åström et al. (2013).

An elastic material model was used. The material parameters were identical to those used in the Abaqus/Explicit simulations. The mechanical behavior of the granular disordered materials, e.g. mortar, was modelled here using beams with reduced stiffness. At the beginning of the simulation, 10 per cent of the beams in the whole model were randomly selected to have their stiffness reduced to 10 per cent of that of the originally defined normal stiffness.

Åström (2006, 2013) has described the fracture criterion implemented in HiDEM code. Here, the fracture criterion was described by the elastic strain threshold;  $\epsilon_{crit} = 0.0003$ . The beams have no mass; thus, upon breakage no mass was lost in contrast to the FEM modelling described above. The particles whose connecting beams are all broken are able to move past each other and collide with the other particles (Åström et al. 2013). The collisions are inelastic which is associated with a loss of kinetic energy upon collision (Åström et al. 2013).

A cylindrical mortar structure with  $\varnothing_{out} = 140$  mm,  $\varnothing_{inside} = 10$  mm and the height of  $H = 200$  mm was modelled with the particles. The ratio  $H/D = 2$  used in the experiments was not respected. Johansson (2008) has shown that the fragmentation is quite independent of the  $H/D$  ratio. The diameter of the particles was 3 mm. The blast load was of the type of the pressure-time history which was applied radially on the borehole wall in addition a simplified post-peak pressure was driving all the particles outwards with a constant pressure. The three peak pressures used in Abaqus/Explicit were used. In all the three loading levels, the active pressure front was moving with the velocity of detonation with temporal duration of 1  $\mu$ s. The detonation front had the velocity (VOD) of 6000 m/s. It began at the rear end face of the cylinder moving with the VOD towards the front end surface. In addition, 20 mm of stemming was considered. On the outer periphery of the cylindrical structure, the mantle, quiet boundary conditions similar to those applied in FEM Abaqus/Explicit were used. Therefore, the shock waves hitting the outer periphery were initially not reflected back into the cylinder. In the initial work with HiDEM the goal was to find out if it could give realistic fragmentation and cracking results. A few details of the used version of HiDEM were not optimal for our modelling purpose such matters like the specimen  $H/D$  and the exact value of VOD e.g. were considered less important. The typical calculation time of the DEM models with 100 interconnected CPU cores (Intel(R) Xeon(R) CPU E5-2690 v4 @ 2.60GHz) was 40 minutes.

## 4 RESULTS

### 4.1 FEM: Abaqus/Explicit

#### 4.1.1 Damage evolution

Figure 5 shows snapshots of the finite element cylindrical disks with centralized borehole subjected to the blast load. The loading function is of the pressure vs. time type, acting on the borehole wall as shown in Figure 3 with peak pressure levels of  $P_{peak} = 35$  MPa, 85 MPa and 166 MPa in models A, B and C, respectively. The pressure function parameters are given in Table 2. The models have an initial time resolution of  $1 \times 10^{-8}$  s associated with an element by element time increment determination algorithm in addition to an element stable time increment (mass scaling) of  $1 \times 10^{-10}$  s that acts once at the beginning and then during the simulation run time. It accompanies the finite elements of the cylindrical disk.

Models A, B and C had to be calibrated individually to get stable results. The calibration parameters are given in Table 3. As soon as the simulations starts, at  $t = 0$  s, the pressure rises up and the compressive equivalent plastic strain accumulates around the borehole forming a crushed zone. The generated crushed zone has a diameter of  $\varnothing_{crushed\ zone} = 12$  mm, 14 mm and 35 mm for models A, B and C, respectively. Approximately 1  $\mu$ s after the peak pressure, the tensile equivalent plastic strain begins accumulating on a ring of finite elements close to but not at the borehole. This tensile zone is visible already at 10  $\mu$ s and we call it the severely fractured zone, compare models A, B and C in Figure 5 at  $t = 10$   $\mu$ s. The tensile stresses act on the already damaged material around the borehole initiating the tensile cracks. About 3 to 5  $\mu$ s after the peak pressure (has been reached), depending on the loading level, tensile cracks appear around the borehole. The shock waves emanating from the borehole drive the cracks to the outer periphery, forming a crack network in between the inner and the outer boundary.

Table 2. Parameters' values of the pressure function.

Parameter	$m_u$	$m_d$	$b_{ratio}$	$\alpha_1$	$\alpha_2$
value	$45 \times 10^5$	$25 \times 10^3$	2	$10^{-7}$	$10^{-2}$

Table 3. Model calibration parameters.

Model	Pressure	Linear bulk viscosity	Quadratic bulk viscosity	Rayleigh damping ( $\beta$ )	Mass scaling threshold
	MPa				s
A	35	0.13	1.16	Not necessary	$1 \times 10^{-10}$
B	85	0.12	1.2	$2 \times 10^{-10}$	$1 \times 10^{-10}$
C	166	0.4	1.2	Not necessary	$1 \times 10^{-10}$

By increasing the peak pressure level, the distance of the severely fractured zone to the borehole wall, diameter of the crushed zone, the number of nucleated



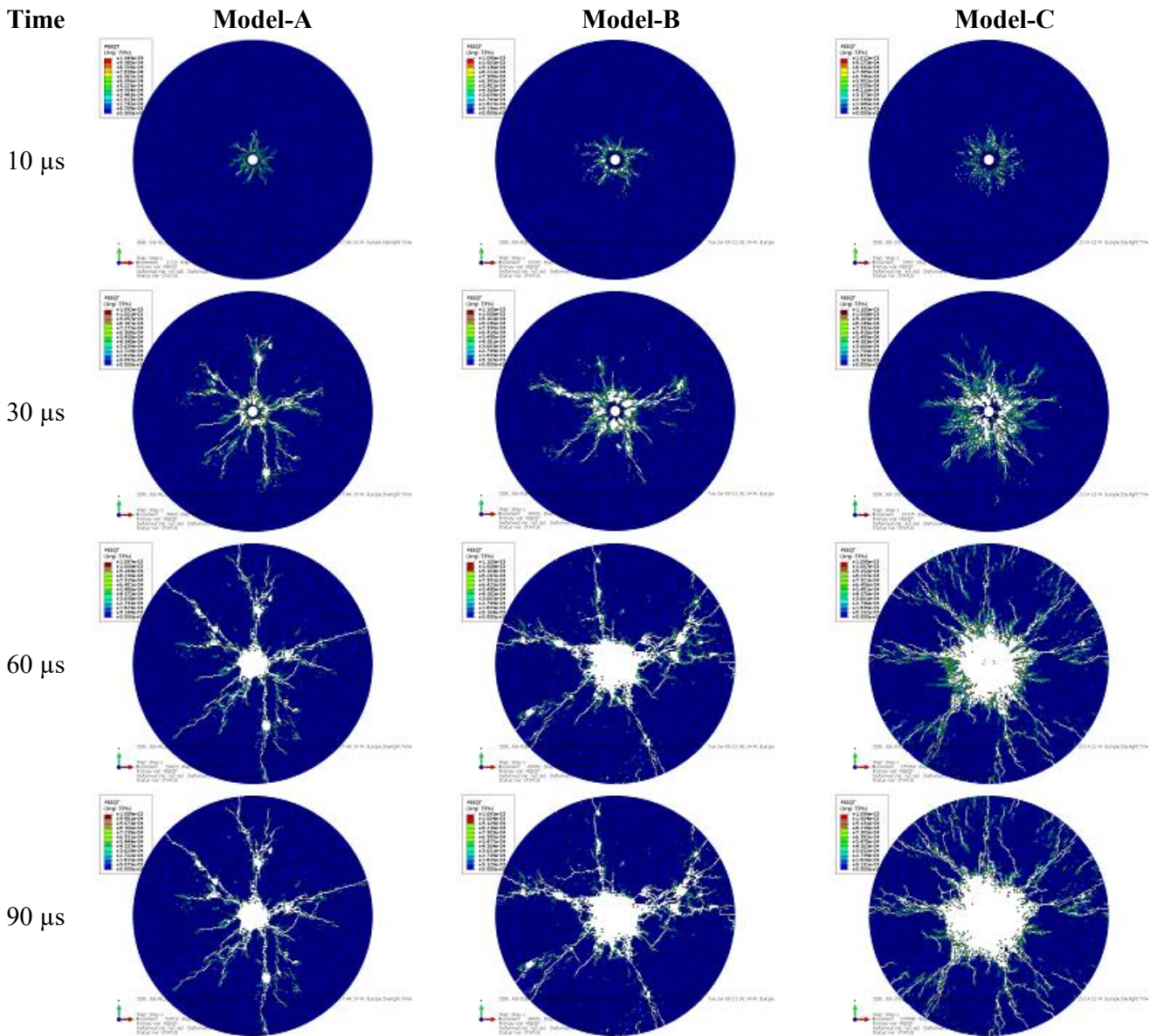


Figure 5. FE cylindrical disks with  $P_{\text{peak}} = 35 \text{ MPa}$ ,  $85 \text{ MPa}$  and  $166 \text{ MPa}$  in models A, B and C. The tensile equivalent plastic strain (PEEQT) as a measure of tensile damage (fully damaged elements are removed so they appear white).

cracks around the borehole wall and the number of cracks which reach the outer periphery of the cylinder increases. In model-C, the amount of the tensile damage occurring around the blast hole is so high that it is no longer possible to count distinguishable nucleated tensile cracks. The post-mortem result of the model has more than 8 radial cracks connecting the severely fractured zone to the outer mantle. A large number of crack branchings, nucleation of tensile cracks not only near the outer periphery but in the whole model, short cracks meeting the outer boundary and the tensile cracks nucleating from the outer boundary converging towards the borehole are distinctive features of this model. A summary of the severely fractured zone is given in Table 4 and the crack network characterization in Table 5.

The crack network characteristics associated with the three loading levels are qualitatively comparable

to the post-mortem results of the in-situ mortar cylinders shot with the same loading levels; compare Figure 1 with Figure 5 at  $90 \mu\text{s}$ .

#### 4.1.2 Energy responses

The issues accompanying the application of the explicit time integration have been discussed above. To understand the associated limitations, the energy responses of the models have been studied to identify the plausibility of the FEM results. Model-C was chosen to illustrate the influence of the four parameter calibrations, see Table 3, on the energy responses and the post-mortem crack network. The calibration process has been performed in the following order:

- Parameter set-1: Default values of bulk viscosities and automatic global time incrementation
- Parameter set-2: Adjusted bulk viscosities, and automatic global time incrementation

- Parameter set-3: Use of mass scaling and element-by-element time incrementation in addition to the Model-2's setup

Figure 6 illustrates the post-mortem crack network and Figure 7 shows the comparison of the energy responses after each of the calibration steps. After the step-1, both the post-mortem cracking network and the energy responses show unrealistic jumps; compare step-1 and -2 in Figure 6 and Figure 7. The voids in the post-mortem image of the step-1 are the symptoms of a large amount of energy dissipated through viscous damping. The post-mortem cracking network does not change visibly between the second and the third calibration step. However, the energy responses illustrate further improvements; compare step-2 and -3 in Figure 7. The total energy for the whole model oscillates around zero for step-3 as it should. The behaviors of the plastic and viscous dissipation energies of the system become smoother and more monotonic.

As mentioned above finding calibration parameter sets that stabilize the FEM simulations is extremely time consuming. This situation becomes more complicated in 3D, where not only the instabilities as in 2D but also unrealistic crack growth patterns are observed. Therefore, as an alternative the discrete element method (DEM) is employed for 3D modelling.

Table 4. Crushed zone and severely fractured zone characterization of the models A, B and C.

Model	Diameter of crushed zone	Diameter of severely fracture zone
	mm	mm
A	12	13
B	14	26
C	36	44.5

Table 5. Crack network characterization of the models A, B and C.

Model	Nucleated at borehole and plastic zone	Total branching points	Total mergings	Arrested cracks	Total nucleation not at borehole and plastic zone	Crack tips reaching to the outer periphery	Number of fragments on face
A	11	14	3	22	4	5	10
B	13	16	4	21	9	15	13
C	too many	too many	too many	>>10	>25	30	too many

#### 4.2 DEM: HiDEM

Figure 8 shows the final 3D crack network of the three loading levels with  $P_{peak} = 35$  MPa, 85 MPa and 166 MPa at  $t = 400$   $\mu$ s. On the left hand side the crack network observable on the surface of the cyli-

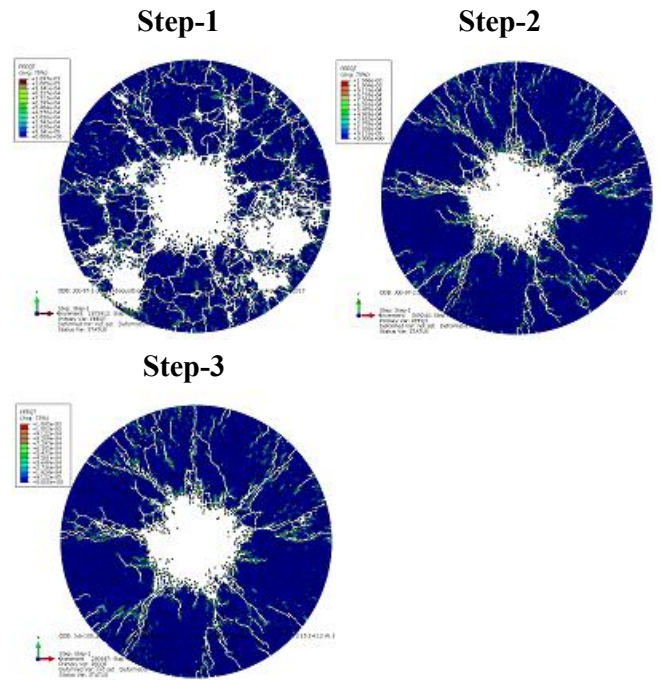


Figure 6. Post-mortem crack network of three steps of energy calibration at 90  $\mu$ s (fully damaged elements are removed so they appear white). Note that Step-3 corresponds to model-C in Figure 5.

nder and on the right hand side the corresponding internal crack network is displayed. By increasing the peak pressure level the number of the radial cracks, branchings and mergings are increasing. This is conforming to the results of FEM/Abaqus presented previously. The number of which, however, is greater than those obtained using FEM calculations. This can be associated with a simpler constitutive model implemented in HiDEM and the simplified method in which the post-peak pressure is implemented. The simplified post-peak pressure is a weakened driving force that drives all particles outwards with a constant pressure on all particles. In reality, escaping gases would be concentrated in the open/opening cracks. The study on these assumptions will be addressed in future work. Comparing the end face post-mortem cracking network of the HiDEM results with those of the experiments also confirms the statements made on the higher number of radial cracks in DEM model above, compare Figure 1 and Figure 8. In Figure 9, the fracture energy curves of the three loading levels are presented. These curves are monotonically increasing and reach a plateau response. The curves are smooth and without any unrealistic jumps such as those often observed in our FEM/Abaqus simulations.

The plausibility of the simulations can also be checked by evaluating the distribution of the debris size. This can also easily be determined in the experiments using standard sieving methods. Such sieving is under way.

Figure 10 shows a set of FSD curves obtained wi-

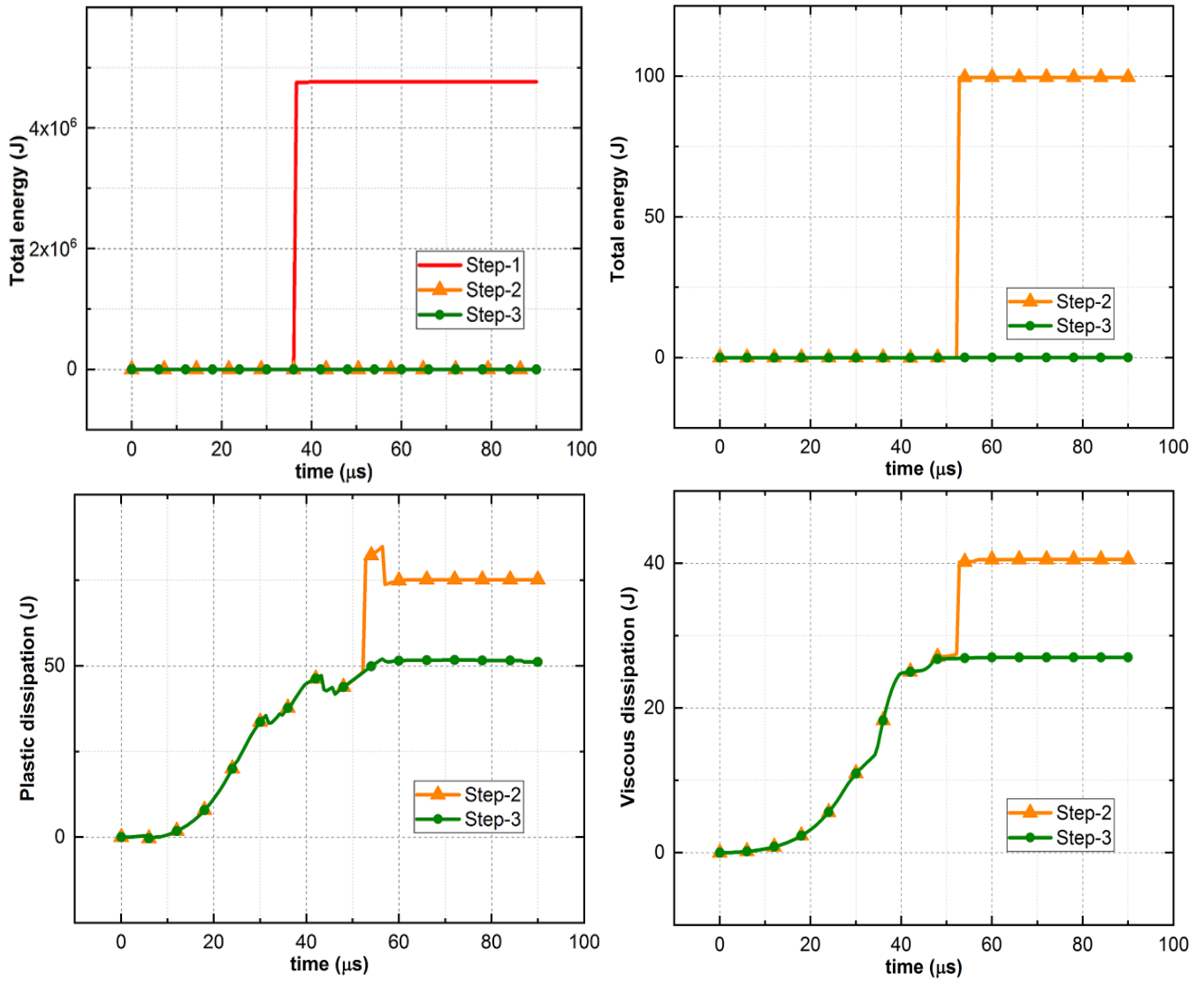


Figure 7. Energy response of model-C to stepwise calibration; Red curves without symbols: Step-1; Orange curves with triangles: Step-2; Green curves with diamonds: Step-3. Top-row: comparison of the total energy output of the whole model for Step -1, -2 and -3. Top-right: magnified total energy output of the whole model for Step -2 and -3. Bottom-row: comparison of the plastic dissipation and the viscous dissipation for Step -2 and -3.

th HiDEM. A fragment is defined by the number of connected spheres  $N$  and the screen size of the fragment is that of a volume equivalent sphere. The upper red curve represents the mass passing fraction of the model with  $P_{\text{peak}} = 166$  MPa. It is smooth and continues connecting the fines region to the coarse one. The curve has Swebrec distribution behavior (Ouchterlony 2009) and is similar to the curves obtained by Johansson (2008) who shot  $\text{Ø}140 \times 280$  mm cylinders of magnetic mortar with 20 g/m decouple PETN cord, also compare with Figure 11. Figure 10 shows that the FSD curves, obtained from DEM simulations, of the cylinders of an identical size by increasing the amount of the explosive shift upward to contain larger fractions of fines. This behavior suggests the Natural Breakage Characteristics (NBC) of Steiner (1991, 1998) which is illustrated by Moser et al. (2003) using seven lab-scale blast experiments; see Figure 5 in Moser et al. (2003). In this figure, the position of the FSD curves along the

mass passing axis shifts upwards by increasing the amount of specific change. In all the three curves illustrated in Figure 10, the fine region starts at 3 mm of mesh size corresponding to the diameter of a single discrete particle. In addition, the curves of the fines region up to 5 mm fragment size are parallel in all the three cases. This 3-5 mm tail is probably an artifact of the particle size used.

By reducing the loading level to  $P_{\text{peak}} = 85$  MPa the discrete character of the data is more pronounced in the region  $x \geq 40$  mm. This behavior in the coarse region suggests a beginning ‘dust and boulders’ behavior and that the number of larger fragments is getting smaller. The blue curve representing the FSD of  $P_{\text{peak}} = 35$  MPa has the full ‘dust and boulder’ behavior expressing a combined discrete and continuous distribution. This characteristic is the result of a blast load which is below the critical charge (Ouchterlony & Moser 2012). At this level, the cylinder just barely falls apart into large blocks, here one bl-

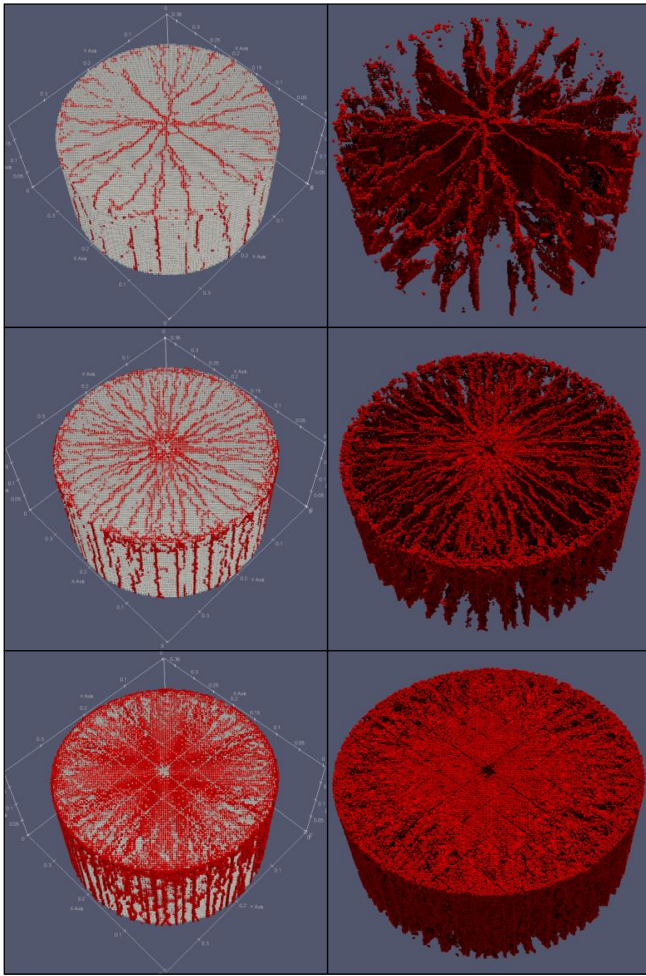


Figure 8. Three dimensional crack network of three blast load levels, left: fracture on surface, right: 3D internal crack network, comparing (from top to bottom)  $P_{peak} = 35$  MPa, 85 MPa and 166 MPa.

ock, in addition to small amounts of very fine materials (Johansson 2008), see Figure 11. In this fragment, the crack network is developed inside the block; however, the required energy to drive the cracks to further propagate, branch or merge to split the body in smaller fragments was not available.

## 5 DISCUSSION AND CONCLUSION

Two numerical calculation methods, i.e. the finite element method (Abaqus) and the discrete element method (HiDEM), with explicit time integration for simulating quasi-brittle material response to civil blast load have been used to model the dynamic crack propagation, branching and merging and eventually to obtain the resultant FSD of blasted mortar cylinders.

With the FEM simulations, the 2D crack propagation, branching, merging and the final cracking network were studied, while the 3D behavior has been simulated with the DEM code. In addition to the cracking parameters, the fragment size distribution

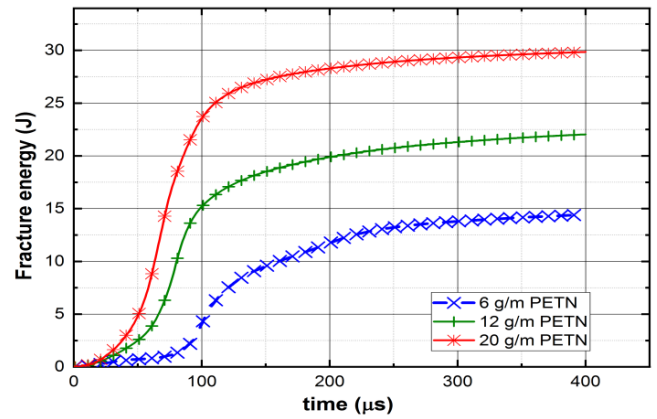


Figure 9. Fracture energy curves of the DEM models for the three loading levels. From bottom to top 35, 85, 166 MPa.

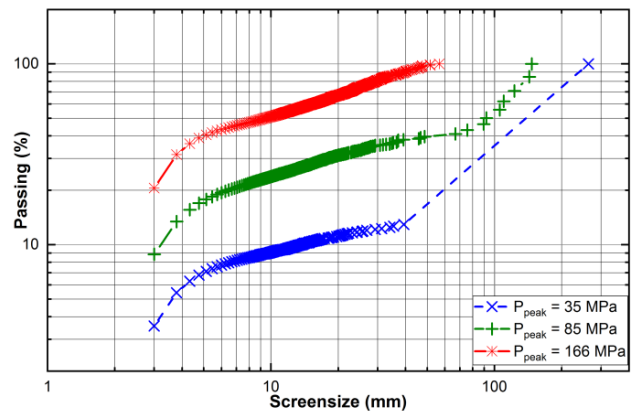


Figure 10. Double logarithmic curves of mass passing, comparing  $P_{peak} = 35$  MPa, 85 MPa and 166 MPa. From top 166 MPa.

of three simulated blasted cylinders has been obtained with the DEM code. Application of the FEM code brought to light a couple of stability issues which made the code difficult to use for our application. They were overcome using model unique calibration parameters associated with the material response and the time integration scheme. This has been shown by monitoring the improvements in the energy responses of a model; the total energy and the two dissipative responses. The FEM results have shown that by increasing the loading level, the number of the total crack nucleations, branchings and mergings increases which consequently should be associated with the increase in the number of fragments visible on the end face. The crack network is qualitatively comparable to the post-mortem HSV images of the mortar cylinder's end surface. Moreover, the FEM results captured very well the stepwise change in the extent of the tensile damage outside the severely fracture zone between different loading levels which is comparable to those of the HSV images. In addition, the results have illustrated the growth in the diameter of the crushed zone and the severely fractured zone caused by increasing the loading levels. However, the large number of failed

and hence deleted elements around the borehole over-estimated the sizes of the crushed zone and the severely fractured zone; thus, it would overestimate the amount of fines with the origin in this region. Moreover, some limitations in the 3D modelling, i.e. unrealistic crack growth pattern in addition to the stability issues encountered in 2D, have limited our use of this FEM method.

The DEM code, however, showed no difficulty in simulating the 3D model. The 3D simulations were made with identical peak pressure levels as those of the FEM simulations. The 3D models showed a more complex crack network. They had a lower stiffness compared to the FEM models. This could be associated with the simpler constitutive model implemented in HiDEM and the simplified method in which the post-peak pressure is implemented. In addition, the fragment size distribution curves obtained using the DEM code for the three loading levels have illustrated the NBC character. Most notably, it is seldom that numerical blast simulations produce FSD curves that look like the ubiquitous Swebrec distribution, including dust and boulders. Future work will focus on the improvement of HiDEM code to allow for the simulations of more realistic crack networks.

## 6 ACKNOWLEDGMENTS

This project is funded by Austrian Science Fund (FWF): P27594-N29. The HiDEM computational results presented have been partially achieved on the Vienna Scientific Cluster (VSC). The HiDEM computational resources used at CSC (Espoo, Finland) have been funded by HPC-Europa3 project funding: HPC17V8YWL.

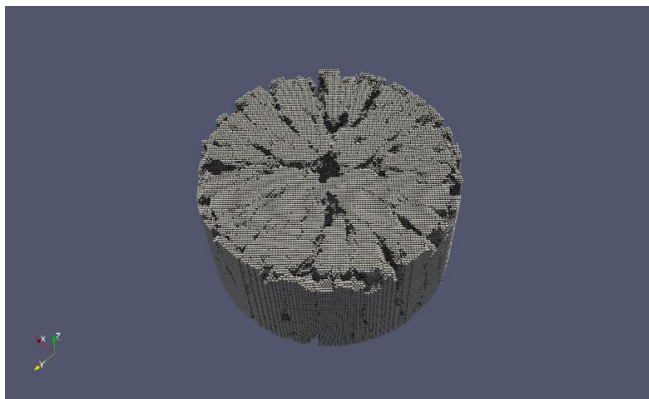


Figure 11. The largest fragment generated at the loading level of  $P_{\text{peak}} = 35$  MPa.

## 7 REFERENCES

- Åström, J.A., 2006. Statistical models of brittle fragmentation. *Advances in Physics* 55(3-4): 247-278.
- Åström, J.A., Riikilä, T.I., Tallinen, T., Zwinger, T., Benn, D., Moore, J.C. & Timonen, J., 2013. A particle based simulation model for glacier dynamics. *The Cryosphere* 7(5): 1591-1602.
- Banadaki, M.M.D. 2010 Stress-wave induced fracture in rock due to explosive action, Doctoral thesis, Toronto, Canada: University of Toronto.
- Cho, S.H. & Kaneko, K., 2004. Influence of the applied pressure waveform on the dynamic fracture processes in rock. *International Journal of Rock Mechanics and Mining Sciences* 41(5): 771-784.
- Djordjevic, N., 1999. A two-component model of blast fragmentation. *In The AusIMM Proceedings*, 304(2): 9-13.
- Djordjevic, N., 2002. Origin of blast-induced fines. *Mining Technology*, 111(2): 143-146.
- Donzé, F.V., Richefeu, V. & Magnier, S.A., 2009. Advances in discrete element method applied to soil, rock and concrete mechanics. *Electronic Journal of Geotechnical Engineering* 8(1): 44.
- Hedjazi, L., Martin, C.L., Guessasma, S., Della Valle, G. & Dendievel, R., 2012. Application of the discrete element method to crack propagation and crack branching in a vitreous dense biopolymer material. *International Journal of Solids and Structures* 49(13): 1893-1899.
- Huh, H. & Kang, W.J., 2002. Crash-worthiness assessment of thin-walled structures with the high-strength steel sheet. *International Journal of Vehicle Design* 30(1-2): 1-21.
- Hillerborg, A., Modeer, M. & Petersson, P. E., 1976. Analysis of crack formation and crack growth in concrete by means of fracture mechanics and finite elements. *Cement and Concrete Research* 6: 773-782.
- Jankowiak, T. & Lodygowski, T., 2005. Identification of parameters of concrete damage plasticity constitutive model. *Foundations of Civil and Environmental Engineering*, 6(1): 53-69.
- Johansson, D. 2008 Fragmentation and waste rock compaction in small-scale confined blasting, Licentiate Thesis, Luleå, Sweden: Luleå University of Technology.
- Johansson, D. & Ouchterlony, F., 2011. Fragmentation in small-scale confined blasting. *International Journal of Mining and Mineral Engineering* 3: 72-94.
- Kukolj, I., Iravani, A., Ouchterlony, F., Weiss, C. & Lubensky, J., 2018. Filming blast fragmentation of rock and mortar cylinders. *In Proceedings of the 12th International Symposium on Rock Fragmentation by Blasting*, in press.
- Lee, J. & Fenves, G. L., 1998. Plastic-Damage model for cyclic loading of concrete structures. *Journal of Engineering Mechanics* 124(8): 892-900.
- Lubliner, J., Oliver, J., Oller, S. & Oñate, E., 1989. A Plastic-Damage Model for Concrete. *International Journal of Solids and Structures* (25): 299-329.
- Ma, G.W. & An, X.M., 2008. Numerical simulation of blasting-induced rock fractures. *International Journal of Rock Mechanics and Mining Sciences* 45(6): 966-975.
- Moser, P. 2003. Less Fines production in aggregate and industrial minerals industry. *In Proceedings of the EFEE 2nd World Conference on explosives & blasting technique*, Balkema, 335-343 2003.
- Moser, P., Grasedieck, A., Olsson, M. & Ouchterlony, F., 2003. Comparison of the blast fragmentation from lab-scale and full-scale tests at Bararp. *In Proceedings of the EFEE 2nd World Conference on explosives & blasting technique*, Balkema, 449-458 2003.

- Nordendale, N.A. 2013 Modeling and simulation of brittle armors under impact and blast effects, Doctoral thesis, Nashville, USA: Vanderbilt University.
- Onederra, I., Esen, S. & Jankovic, A., 2004. Estimation of fines generated by blasting—applications for the mining and quarrying industries. *Mining Technology*, 113(4): 237-247.
- Ouchterlony, F. & Moser, P., 2012. On the branching-merging mechanism during dynamic crack growth as a major source of fines in rock blasting. *In Proceedings of the 10th International Symposium on Rock Fragmentation by Blasting*, New Delhi, 65-75 2012.
- Ouchterlony, F., 2009. Fragmentation characterization: the Swebrec function and its use in blast engineering. *In International Symposium on Rock Fragmentation by Blasting*, Granada, 3-22 2009.
- Rossmannith, H.P., Hochholdinger-Arsic, V. & Uenishi, K., 2005. Understanding size and boundary effects in scaled model blasts – plane problems, *Fragblast*, 9:2, 93-125 2005.
- Sanchidrián, J.A. 2017. Personal communication.
- Schimek, P., Ouchterlony, F. & Moser, P., 2013. Experimental blast fragmentation research in model-scale bench blasts. *In International Symposium on Rock Fragmentation by Blasting*, 51-60 2013.
- Simulia, 2014. Abaqus Theory Manual, Version 6.14, Dassault Systèmes Simulia Corporation, Providence, RI, USA.
- Steiner, H.J., 1998. Zerkleinerungstechnische Eigenschaften von Gesteinen. *Sonderdruck aus Felsbau 16*, 5: 320-325.
- Steiner, H.J., 1991. The significance of the Rittinger equation in present-day comminution technology. *In Proceeding of 17th International Mineral Processing Congress*, Dresden, 177-178 1991.
- Sun, C. 2013 Damage zone prediction for rock blasting, Doctoral Thesis, Salt Lake City, USA: The University of Utah.
- Trivino, L., Mohanty, B. & Munjiza, A., 2009. Seismic radiation patterns from cylindrical explosive charges by combined analytical and combined finite-discrete element methods. *In Proceedings of 9th International Symposium on Rock Fragmentation by Blasting*, Granada, 415-426 2009.
- Wang, Y. & Alonso-Marroquín, F., 2009. DEM simulation of comminution: fragmentation and size distribution. *In AIP Conference Proceedings*, 1145(1): 863-866 2009.
- Yi, C. & Johansson, D., 2015. Discrete element modelling of blast fragmentation of a mortar cylinder. *In 11th International Symposium on Rock Fragmentation by Blasting*, Sydney, 793-800 2015.
- Zhu, Z., Mohanty, B. & Xie, H., 2007. Numerical investigation of blasting-induced crack initiation and propagation in rocks. *International Journal of Rock Mechanics and Mining Sciences* 44(3): 412-424.

The VUSDFLD subroutine used in this paper is given in Appendix A.

**6**

**Paper II:**

**Origin of fines particle in blasting fragmentation:  
compressive crushing**




This page intentionally left blank.

## Physical Origin of the Fine-Particle Problem in Blasting Fragmentation

A. Iravani,<sup>1,\*</sup> J. A. Åström,<sup>2</sup> and F. Ouchterlony<sup>1</sup>

<sup>1</sup>*Department of Mineral Resources Engineering, Montanuniversitaet Leoben, A8700 Leoben, Austria*

<sup>2</sup>*CSC—IT Center for Science, P.O. Box 405, FIN-02101 Esbo, Finland*

 (Received 7 March 2018; revised manuscript received 23 May 2018; published 4 September 2018)

Blasting with explosives and crushing with mills are two major processes for extracting ore minerals. Longstanding problems with these processes are “fines” production in blasting and the related energy consumption of mills. Here, we demonstrate, using numerical simulations and comparison with experiments, that both problems emerge from two universal mechanisms: unstable tensile-crack propagation and compressive impact crushing. These lead to a universal mass-passing-fraction function in sieving. Crushing is limited to, and produces almost all the fines, and thereby inherently consumes a lot of fracture energy. Tensile cracks also produce fines, but the majority of the mass is confined in larger fragments. The key to resolving the fines and energy problem thus lies in minimizing crushing while inducing enough tensile load to reach the breakage threshold.

DOI: [10.1103/PhysRevApplied.10.034001](https://doi.org/10.1103/PhysRevApplied.10.034001)

### I. INTRODUCTION

The extraction of metals from ore minerals is one of the most important industrial processes. In a schematic sense, the initial phase of mineral extraction is the blasting of rock to break it, and then to crush large fragments in mills to produce pieces of desired sizes. A similar procedure is used in the production of construction aggregates for civil-engineering purposes. The interplay between blasting and crushing-milling fragments is quite complex [1]. Two longstanding problems exist within these processes: (1) the production of “fines” or dust in the blasting process, which is an economic waste and an environmental hazard [2,3]; and (2) the huge energy consumption of grinders and mills run by electric motors [4].

The energy consumption problem is, at least partly, a consequence of fines produced in mills. The creation of fines requires a lot of energy as the total created fracture surface grows large. Consequently, the two problems can be condensed into a “fines” problem. A better understanding of the origin of fines could help eliminate these problems at an initial stage and improve the blasting and crushing practices.

There are existing theories on the source of fine particles, such as the crushed-zone model (CZM), which

assumes that fines originate from an annular compressive failure around the blasthole [5] consisting of two nonoverlapping Rosin-Rammler components, one for the coarse material and one for the fine material of the crushed zone. The CZM may be interpreted so that the fragment size is almost (solely) defined by the distance to a blasthole. The two-component model (TCM) [6], in which the connection between distance and size is more diffuse, has defined the shear failure along the *in situ* joints and blast-induced cracks as the other source of fines [7]. Additions to the CZM by Onederra *et al.* [8] have assumed that the fine particles originate from a circular compressive failure zone around the borehole, as well as from crushed and/or sheared material bounded by major blast-induced radial cracks, which are assumed to be evenly distributed around a blasthole, planar, and also to continue along the length of the explosive charge. This constitutes the star-shaped crushed-zone model [9].

The blast cylinders of Svahn [10] are ideal test models to analyze the star-shaped model. The cylinders ( $\varnothing$  300 mm  $\times$  length 600 mm), whose material is categorized using three different colors in the radial direction, i.e.,  $\varnothing_{\text{outer}} = 120, 200, \text{ and } 300$  mm for black, yellow, and green, are blasted. The colored layers are concentric and centrally charged [see Fig. 2(a) in the Supplemental Material [9]]. The fragment-size distribution (FSD) results illustrate a whole range of fragment sizes for the core layer, with an identical general character to that of the outer layers. The results illustrated no tendency either for the core material to consist only of fines or for the outer layers to contain no fines. Both regions (black, yellow + green) produce the whole range of fragment sizes. The black core contains

\*armin.iravani@unileoben.ac.at

Published by the American Physical Society under the terms of the [Creative Commons Attribution 4.0 International license](https://creativecommons.org/licenses/by/4.0/). Further distribution of this work must maintain attribution to the author(s) and the published article's title, journal citation, and DOI.

even less fragments that are smaller than 2 mm fines in absolute terms than the outer layers, bearing in mind that there is no crushing inside the two outer layers [see Fig. 2(b) in the Supplemental Material [9]]. From the analysis of the star-shaped model, one realizes that the relative amount of fines will always decrease with each successive layer of materials. However, the absolute amount of fines generated in the outermost layer is almost double that of the middle layer. This would indicate that the fine particles are generated by mechanisms other than crushing in the outermost layer.

When blasting cylinders of a given size with decreasing amounts of explosives, a critical charge size is reached. At this stage, the cylinder barely falls apart into a few large blocks plus small amounts of very fine materials [11,12]. In the cases referred to, the crushed zone and fragment collisions do not exist. Åström [13] has addressed this issue and declared the unstable rapidly propagating cracks as a source of fines, the physical origin of which is rooted in an intrinsic scale-invariant branching-merging process. Yet another plausible theory is that the fines are generated by a mechanism involving dynamic crack branching and merging [14,15].

The fines problem can be characterized and quantified by the so-called mass-passing-fraction (MPF) function, which has characteristics that are universal for both blasting and mill crushing under different loads [16]. In the mining and construction industries, which handle vast masses of rock and ore each year, productivity is related to mass moved and crushed or milled (comminution), not to numbers of fragments and/or mass for a given size. Aggregate products are, for example, often further defined in terms of their MPF; hence the industries' preoccupation with the MPF. The  $MPF(r)$  is defined as the fraction of mass for a collection of fragments that pass through sieves with different mesh sizes  $r$ . That is, for a mesh size  $r = 0$ ,  $MPF(r) = 0.0$ , and  $MPF(r > r_{\max}) = 1.0$  or 100%, where  $r_{\max}$  is approximately the largest possible fragment.

In most applications, oversize fragments that are too large to handle are a larger liability than an excessive amount of fines but respirable dust, slow leaching and ore losses, etc., are important problems associated with fines. An ongoing project [17] is trying to define the role of crack branching and merging in the generation of fines by HSV recording and modeling of dynamic cracks [11,18] (for the expected use of the results beyond rock-fracture research, see Sec. II in the Supplemental Material [9]).

## II. THE MODEL

In this paper, we employ a discrete-element code (HiDEM) to simulate blasting experiments of magnetic mortar cylinders. The experiments were conducted by Johansson [12] as a set of laboratory blasting fragmentations of magnetic mortar cylinders ( $\varnothing$  140 mm  $\times$  length

280 mm) with PETN (pentaerythritol tetranitrate) cord, with charge concentrations varying from 3, 5, 10, and 20 to 40 g/m. Here, we use data from two set of blasting experiments with different confining conditions, i.e., loose and stiff confinement. The fragment data are collected as mass-passing fractions in sieving with mesh sizes ranging from 0.063 to 90 mm.

In the HiDEM code, a brittle material is discretized as a dense-packed face-centered cubic (fcc) lattice of inelastic spheres connected by breakable beams. The model is described in detail in Refs [13,19]. We model cylinders with material properties that mimic those of magnetic mortar, and use a time-dependent pressure pulse that crudely replicates the blasting process [11]. That is, we apply an initial pressure pulse with a value  $P_{\text{peak}}$  proportional to the charge density that lasts for about a microsecond, and that travels through the sample with a velocity of detonation ( $VOD \sim 6000$  m/s). There is also a post-peak pressure pulse ( $P_{\text{post}} \sim 0.02 P_{\text{peak}}$ ) that lasts for 30  $\mu$ s, and that acts on a larger region than the initial pulse. The true blasting process is highly complex [20] and cannot be modeled in any detail here. Regardless, it seems that applying the pressure-pulse scheme with minor adjustments of the post-peak pressure (0.4–6% of the peak pressure) to mimic various experimental boundary conditions is enough for the numerical model to replicate the crack patterns and MPFs of the experiments. That is, we use the slightly larger  $P_{\text{post}}$  for looser confinement and vice versa. This is simply an observation of how the model works. We are not aware of the physical origin of this behavior.

Before examining the simulation and experimental results, we construct a theoretical estimate of  $MPF(r)$ . The blasting experiments create a compressive shock wave traveling outward in the radial direction. As a cylinder expands outward, it will induce tension in the tangential direction. This immediately indicates that the blasting process will generate both tensile fracture and crushing.

Tensile fracture means crack propagation. Propagating cracks easily become unstable and branch. Crack branches easily merge again to form fragments, which means that propagating cracks leave behind not smooth crack surfaces but fragment-filled fracture zones of finite widths. This process is inherently universal and leads to a characteristic FSD [13,21]. The number of fragments,  $n_{\text{bm}}(s)$ , of size  $s$  in an interval  $ds$  can be written as  $n_{\text{bm}}(s)ds = C_2 s^{-\alpha} \exp(-s/C_3)ds$ , with  $\alpha = (2D - 1)/D$ , where  $D$  is dimension (i.e.,  $D = 1, 2, 3$  for rods, membranes, and bulk objects, respectively) and  $C_2, C_3$  are nonuniversal constants [13,21,22]. The dimensionless size  $s$  is measured as the number of grains composing a fragment (i.e., DEM particles or mortar grains). The power-law part of the FSD originates from branching and merging cracks, while the exponential part introduces a cut-off at a finite width of the fracture zone at which fragmentation locally runs out

of energy. In nature, fragmentation processes of this kind range in size from stellar fragments [23] through icebergs [24] and meteorites [25] to fault gouge [26] and dust [27].

Crushing contains some induced tensile fracturing but it—and especially grinding—are essentially compressive-shear fracture and they are typically processes of continued fragmentation following an initial crack-propagation phase. Such a process essentially modifies the FSD. When tensile cracks have opened up, small-size debris-filled fracture zones are formed. In compressive shear, this debris will be crushed into decreasingly smaller fragments by grinding and compaction. Grinding compaction can, in a schematic fashion, be viewed as a hierarchical process in which ever-smaller fragments are broken to fill pore space that opens up in continuous shear deformation [28,29]. Such a process has a power-law FSD of the form  $n_{\text{crush}}(s)ds = C_1 s^{-\beta} ds$  [13], where  $C_1$  is a constant and  $\beta \sim 1.8\text{--}3.5$  for  $D = 3$ , depending on the degree of grinding and/or crushing. The lower bound for  $\beta$  is determined by  $\beta > \alpha$ , while the upper bound of 3.5 seems to be more of a practical nature than a hard theoretical limit. A value of  $\beta \approx 3.5$  means a very high degree of grinding.

For low blasting loads, the fragments formed by branching and merging in fracture zones amount to just a small fraction of the total mass of a cylinder. Large more or less undamaged “boulders” remain between the formed fracture zones. Note that in our case “boulder” does not mean oversize with respect to the available equipment but merely fragments that are very large compared to the original cylinder. At low loads, the mass fraction of these boulders easily dominates the MPF. For increasing loads, the mass fraction of the boulders decreases and eventually vanishes (cf., Fig. 1). As a first approximation, crack paths far enough from each other for boulders to be formed may be considered as independent. This will result in a Poisson process, and an essentially exponential FSD for boulders [30].

If  $n(s)$  describes the number density of fragments with  $s$  grains, the FSD, or the number of fragments in a size interval  $ds$ , can then be written as follows:

$$n(s)ds = C_1 s^{-\beta} ds + C_2 s^{-\alpha} \exp\left(-\frac{s}{C_3}\right) ds + n_b(s)ds, \quad (1)$$

where the value for  $\beta$  can be determined from a grinding experiment which is discussed later, (see Sec. III descriptions regarding Fig. 4),  $C_3$  determines the typical size of the boulders,  $n_b(s) \sim \exp(-s/s_b)$  is the size distribution for the boulders, and  $s_b$  is the characteristic size of a boulder, governed by the density of induced tensile cracks. Sometimes a large-size cut-off to the crushing power law also appears, which can be approximated by multiplying that first term on the right-hand side by another exponential function.

With the transformation  $ds \propto r^2 dr$  for  $D = 3$ , the MPF( $r$ )  $\sim (1/M_0) \int_{r_{\text{grain}}}^r r^3 n(r) r^2 dr$  can be approximated for fragments smaller than boulders, i.e., for  $r \lesssim r_{\text{grain}} C_3^{1/3}$ , using the function

$$\text{MPF}(r) = f_{\text{cr}} \left(1.0 - \left(\frac{r}{r_{\text{grain}}}\right)^{-3\beta+6}\right) + f_{\text{bm}} \left(\frac{r}{r_{\text{max}}}\right)^{-3\alpha+6}, \quad (2)$$

where

$$f_{\text{cr}} = \frac{m_{\text{grain}}}{M_0} \frac{-3C_1}{-3\beta+6}, \quad (3)$$

$$f_{\text{bm}} = \frac{m_{\text{grain}}}{M_0} \frac{3C_2 r_{\text{max}}^{-3\alpha+6}}{(r_{\text{grain}}^{-3\alpha+6})(-3\alpha+6)}, \quad (4)$$

in which  $M_0$  is the total mass;  $r_{\text{grain}}$  is the grain size of the material; and, for  $D = 3$ , the value of  $3\alpha + 6$  is equal to 1 and thus the first part on the right-hand side of Eq. (2) is the empirical Gates-Gaudin-Schuhmann (GGs) [31] or a simple power-law distribution with exponent  $m = 1$ , and the second part represents the characteristic shape of MPFs for the crushed fines. The parameters  $f_{\text{bm}}, f_{\text{cr}}$  thus determine the mass fractions of fragments formed in the branching-merging and crushing processes, respectively. The ratio  $f_{\text{cr}}/f_{\text{bm}} \sim C_1 r_{\text{grain}}/C_2 r_{\text{max}}$  determines the ratio of crushing to branching-merging fragments. This could be used as such to be the representative measure for the optimization of blasting and the corresponding fragmentation. Finally, the mass fraction of the boulders, absent from Eq. (2), can then be written as  $1.0 - (f_{\text{bm}} + f_{\text{cr}})$ .

In the general case, the MPF can be written as a sum of two incomplete Gamma functions and, if  $n_b(r)$  is assumed to be a Poisson process, an exponential function.

### III. RESULTS AND DISCUSSION

Figure 2(a) shows an experimental MPF( $r$ ) for  $P_{\text{peak}} = 160$  MPa and  $P_{\text{post}} = 0.06 P_{\text{peak}}$ . The experimental data can be fitted almost perfectly by the numerically integrated theoretical MPF( $r$ ) from the general case, except for the very smallest fragments. The theoretical function is obtained by an integral with an assumed constant material grain size  $r_{\text{grain}}$ . For real materials,  $r_{\text{grain}}$  is not a constant, and the small-size limit of the MPF( $r$ ) will reflect this grain-size distribution. For simplicity, we may assume that the mortar grains have a Gaussian size distribution and, as is evident in Fig. 2(a), this fits the experimental data very well.

For comparison, a straight line that represents the GGS( $m = 1$ ) function is also displayed in Fig. 2(a) to demonstrate the range in which branching-merging fragments dominate the MPF. Before reaching 100%, the

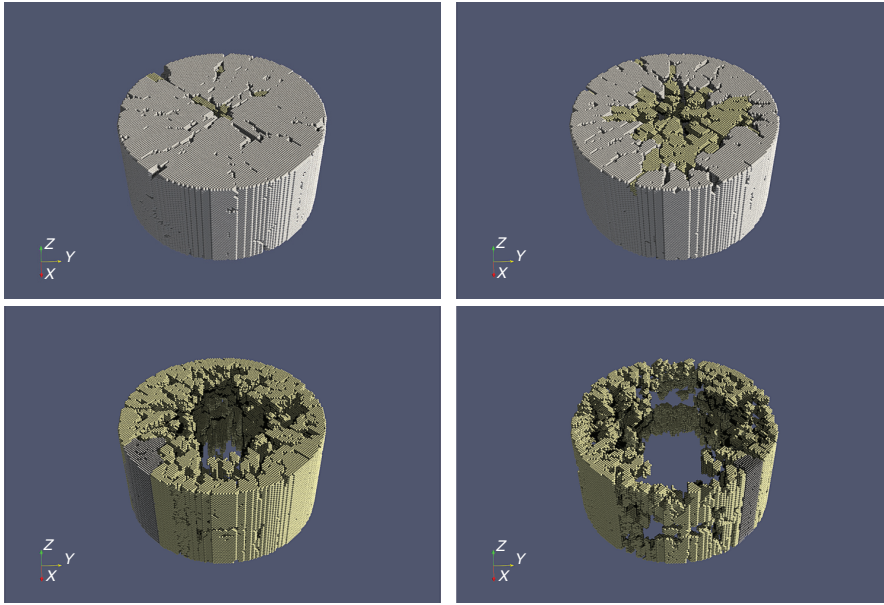


FIG. 1. The numerically computed fragmented cylinders, with  $P_{\text{peak}} = 35, 60, 80,$  and  $160$  MPa, top left to bottom right, respectively. Reconstructions with fragments larger than  $s = 100$  are shown. The largest intact fragment is shown in gray. Fragments containing more than 100 DEM particles are shown in yellow. Smaller fragments are omitted. The DEM-particle radius,  $r_{\text{grain}} = 3$  mm.

experimental MPF also deviates from the GGS function. This part contains the boulders, and in Fig. 2(a) an exponential function for  $n_b(s)$  is used.

The much shorter curve in Fig. 2(a) consists of the numerical MPF and the corresponding fit to the theoretical MPF. The rather striking difference between the experimental and numerical MPFs has the rather trivial origin that the mortar grains are typically of size  $r_{\text{grain}} \sim 0.1$  mm, while in the simulations  $r_{\text{grain}} \sim 3$  mm is used. Figure 2(b) displays a more useful comparison: as this figure demonstrates, the crushing part of  $n(s)$  extends to the kink at about 20–30 grains for both the experimental

and the numerical data. Since the grain size in the numerical model is  $r_{\text{grain}} = 3$  mm, and in the experimental model  $r_{\text{grain}} \sim 0.1$  mm, this means that the mass fraction for crushing is much larger for the numerical data, and it indicates that numbers of grains rather than fragment mass govern crushing.

The data points corresponding to the largest fragments (approximately  $C_3$ ) in Fig. 2(b) are approximately  $10^4$  for the numerical data and approximately  $10^8$  for the experimental [there are so few boulders that  $n(s)$  cannot be determined and they are therefore left out of Fig. 2(b)]. This reflects the scaling  $C_3 \propto r_{\text{grain}}^{-3}$  quite well, indicating

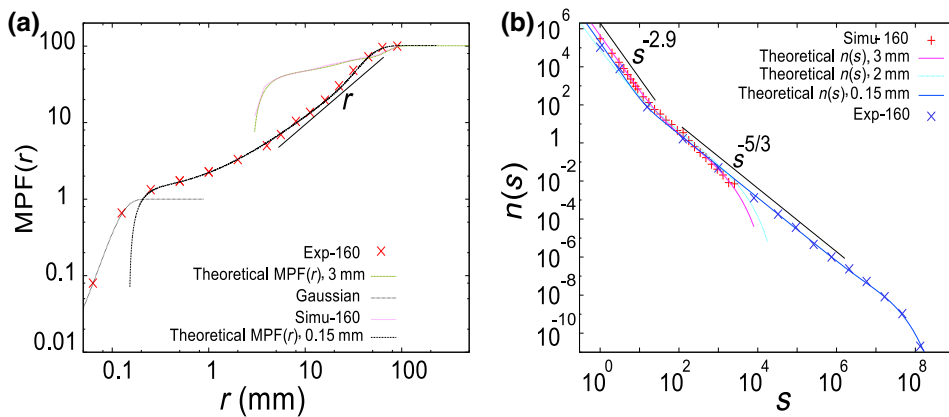


FIG. 2. Experimentally and numerically obtained (a) MPFs and (b) values of  $n(s)$  for  $P_{\text{peak}} \approx 160$  MPa. The experimental (Exp-160) and numerical (Simu-160) data are fitted with the theoretical MPF. In (a) the GGS( $m = 1$ ) function ( $\text{MPF} \propto r$ ) is displayed for comparison, and the grain-size distribution for the fines tail of the experimental MPF is compared to a Gaussian function (grains in the size range  $r \sim 0.1$  mm). In (b), the power laws for crushing and branching-merging are displayed for comparison. The numerical results are for  $r_{\text{grain}} = 2$  and  $3$  mm. The large-fragment cut-off for the distributions (approximately  $C_3$ ) scales as  $C_3 \propto r_{\text{grain}}^{-3}$ .

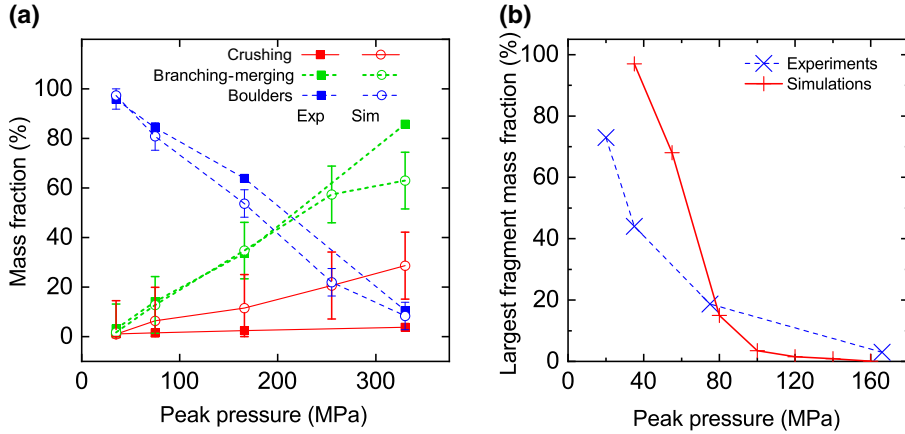


FIG. 3. (a) The crushing, branching-merging, and boulder mass fractions as functions of  $P_{\text{peak}}$  for numerical simulations with  $r_{\text{grain}} = 3$  mm and  $P_{\text{post}} = 0.004 P_{\text{peak}}$ , and experiments with a stiff cylinder confinement. Filled symbols denote the experimental data and unfilled symbols show the simulation data. The estimated errors of the numerical results compared with the experimental data are illustrated by error bars. (b) The mass fraction of the largest fragment as a function of  $P_{\text{peak}}$  for simulations with  $P_{\text{post}} = 0.06 P_{\text{peak}}$  and experiments with a looser confinement: continuous line, simulation; broken line, experiments.

that while number of grains are important for the mass fraction of the crushing fragments, this is not so for the larger fragments. To confirm this, we also compute  $n(s)$  for  $r_{\text{grain}} = 2$  mm. The best fit to this data by the theoretical  $n(s)$  is also displayed in Fig. 2(b). As is evident, the data in this case follow the data for  $r_{\text{grain}} = 3$  mm, except that  $C_3$  moves to a larger value of  $s$  by an

amount roughly consistent with the expected scaling. Consequently, as the observed scaling  $C_3 \propto r_{\text{grain}}^{-3}$  entails, the largest fragments formed by branching-merging have sizes that are independent of  $r_{\text{grain}}$ .

Both Eqs. (1) and (2) can be used to define mass fractions of fragments formed by crushing, branching-merging, and boulders. It is an interesting exercise to plot

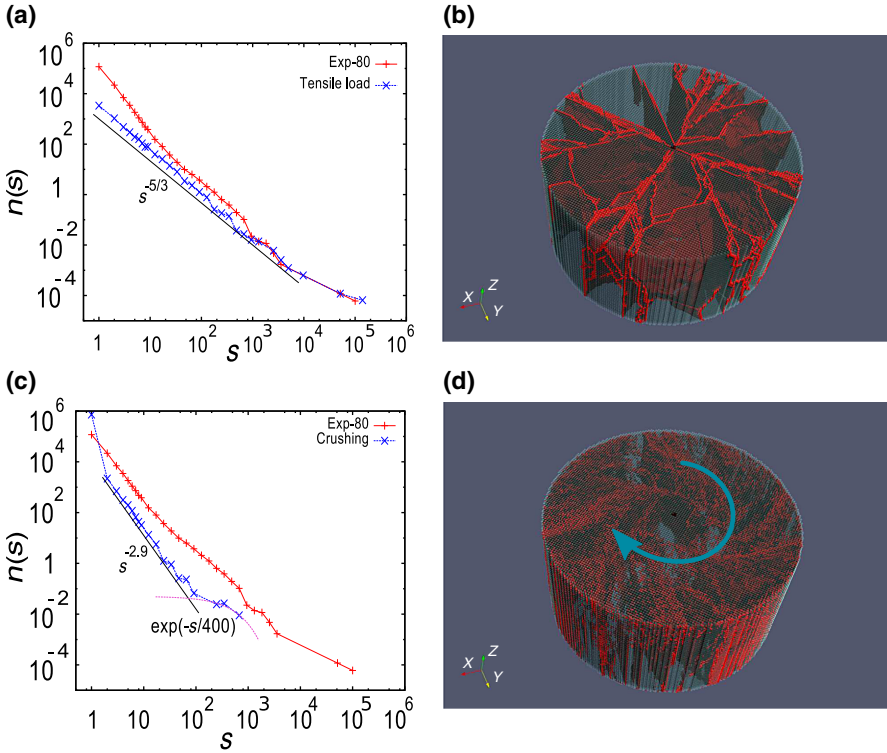


FIG. 4. (a)  $n(s)$  for inflation fragmentation compared to the branching-merging power law. (b) Crack patterns formed during inflation. (c)  $n(s)$  for grinding fragmentation compared to the crushing power law. (d) Crack patterns formed during grinding: the arrow shows the direction of rotation. The blasting  $n(s)$  of  $P_{\text{peak}} = 80$  MPa is displayed for comparison, and an exponential function indicates boulders shown in (c).

these mass fractions from the fitted functions as a function of  $P_{\text{peak}}$  for the numerical and experimental data. Another useful plot is the mass fraction of the largest fragment as a function of  $P_{\text{peak}}$ .

Figure 3(a) displays the mass fractions for the three categories as functions of  $P_{\text{peak}}$ , for simulations with  $P_{\text{post}} = 0.004 P_{\text{peak}}$  and experiments with a stiff confinement [12]. The numerical data ( $r_{\text{grain}} = 3$  mm) again confirm the significantly larger mass fraction for crushing for the larger-grain-size numerical data as compared to the experiments [Fig. 3(a)]. For the other categories, the trend is, as expected, that the mass fraction of the boulders decreases significantly with  $P_{\text{peak}}$ , while those of the smaller fragments created by branching-merging and crushing increase, also as expected. It is obvious that the numerical and experimental data match each other very well, apart from the expected deviations due to differences in  $r_{\text{grain}}$ , which also explain the slight difference in the branching-merging mass fraction for the highest  $P_{\text{peak}}$ , at which the crushing mass fraction grows large enough to begin depleting the branching-merging fraction. The estimated errors of the numerical results are measured (using the standard error of estimate) and illustrated by the error bars. The value for crushing is 13.5% and that for branching-merging is 11.4%, while the value for the boulders is 5.37%.

Figure 3(b) displays the mass fraction of the largest fragment in the simulations compared to the difference in the mass-passing fraction between the largest and second-largest mesh-size sieves, which can be used as a proxy for the largest fragment. These results are for loose experimental confinement and simulations with  $P_{\text{post}} = 0.06 P_{\text{peak}}$ . Figure 3(b) demonstrates that a value of  $P_{\text{peak}} \sim 60\text{--}80$  MPa or larger is needed to reach the breakage threshold of the cylinder. This corresponds to the damage-fragmentation transition [32,33]. At smaller  $P_{\text{peak}}$ , the mass fraction of the largest “fragment” is approximately 1.

To further demonstrate the difference between tensile and compressive fragmentation, we apply two artificial loading conditions that have no direct experimental counterparts. These two loading conditions are chosen to either maximize the tensile loading and minimize the compressive crushing or vice versa. For tensile loading, we apply a force on each DEM particle that increases linearly with time in the outward radial direction, a so-called inflation. For crushing, we apply a similar load on each particle as a compression along the cylindrical axis, as well as a tangential torsion force acting clockwise around the axis of the cylinder; i.e., we choose loading conditions that mimic either a slow “inflation” or a traditional grinding motion.

The results of this exercise are displayed in Fig. 4. Figure 4(a) shows  $n(s)$  for the tensile loading condition and, for comparison, the corresponding function for blasting at  $P_{\text{peak}} = 80$  MPa and the branching-merging power-law function  $s^{-5/3}$ . This figure clearly demonstrates that,

in this case,  $n(s)$  consists of branching-merging fragments and boulders, while crushing fragments are absent. The cracks formed during inflation are displayed in Fig. 4(b). Here, the branching and merging of cracks that form small fragments in fracture zones along the major crack paths are clearly visible. Also, the large boulders between the cracks are easy to detect. This crack pattern largely mimics what can be observed in the experiments, except for the crushing zones near the borehole that can be seen in Fig. 1, for which blasting is applied.

This particular case of inflation fragmentation produces an FSD with ten boulders. The largest one contains 20% of the mass and the smallest 1.3% of the mass. Together, they make up 87% of the mass. The remaining mass is contained in the branching-merging fragments. Also for these, the majority of the mass is contained in the larger fragments. This is easily demonstrated by the integral  $\int s^{-5/3} s ds$ , which represents the total mass, and which gets its major contribution from large values of  $s$ .

Figures 4(c) and 4(d) show the corresponding results for the grinding-type loading condition. Figure 4(c) shows that  $n(s)$  follows the crushing power law  $n(s) \propto s^{-2.9}$  for fragments of a size up to about  $s \sim 100$ . It is worthwhile noting that the number of fragments piles up at  $s = 1$ , indicating that the grinding process attempts to break even these small fragments—which, however, is not allowed in the numerical model. A few boulders that are described well by an exponential function can also be detected.

The crack pattern in Fig. 4(d) show rather obvious traces of the grinding process, and it is distinctly different from the tensile pattern in Fig. 4(b). The grinding process proceeds so that at first a few shear cracks are formed which determine the boulders, and thereafter the grinding process proceeds by crushing fragments within shear zones formed along the shear cracks [13].

#### IV. SUMMARY AND CONCLUSION

In summary, the results in this paper clearly demonstrate that blasting-fragmentation FSDs are composed of three parts, all of which can be described separately by universal fragmentation mechanisms. The fines, or the smallest dustlike particles, arise almost exclusively as a result of compressive-shear fragmentation or crushing. Crushing consumes a lot energy as the density of fracture surfaces increases considerably in regions with very fine fragmentation. The grain-size distribution of the material seems to influence crushing significantly, in contrast to the larger fragments. That is, the mass fraction of the crushing fines decreases with smaller grains, at least for the particular fragmentation-process boundary conditions used here. Thus DEM modeling will probably tend to overestimate the amount of crushed material produced by blasting.

Fragments larger than fines are formed as a result of tensile-crack propagation. Tensile cracks branch and

merge to form smaller fragments, and the tensile cracks delineate the largest fragments, called boulders.

Our results indicate two possible strategies for addressing the fines problem. (1) As the fraction of fines increases monotonically with  $P_{\text{peak}}$  and a minimum  $P_{\text{peak}}$  is required to reach the breakage threshold, the blasting process should be designed with a minimum load to reach this threshold, and with a suitable geometrical proximity of applied charges to limit the resulting boulder size. (2) The blasting itself should be designed so that it minimizes compressive shear and maximizes tensile load. In full-scale blasting rounds with a sequence of delayed holes, alternative (1) would have to include a consideration of the effect of the jointing of the rock mass. The delay sequence itself makes it possible to extend alternative (2) to include consideration of the interaction of tensile cracks from one blasthole with the waves emanating from the next. When computer capacity has grown sufficiently, a code such as HiDEM could become a valuable tool in choosing the right combination of blast parameters at full scale.

#### ACKNOWLEDGMENTS

This project is funded by the Austrian Science Fund (FWF) Grant No. P27594-N269 and has been performed under the Project HPC-EUROPA3 (Grant No. INFRAIA-2016-1-730897), with the support of the EC Research Innovation Action under the H2020 program. In particular, we gratefully acknowledge the support of the CSC—IT Center for Science for the computer resources and technical support provided.

- 
- [1] F. Ouchterlony, Report project P2000-10: Energy optimisation during comminution. Stockholm: Swedish Min. Res. Org. MinFo.
- [2] P. Moser, in *Proceedings of EFEE 2nd World Conference on Explosives and Blasting Technique, 2003*, edited by R. Holmberg (Rotterdam, Balkema, 2003), p. 335.
- [3] P. Moser, in *Proceedings of 3rd EFEE World Conference on Explosives and Blasting*, edited by R. Holmberg (Brighton, UK, 2005), p. 567.
- [4] J. A. Herbst and W. T. Pate, in *Proceeding of Mine to Mill Conference, Brisbane, 1998* (AusIMM, Carlton, 1998), p. 243.
- [5] D. Thornton, S. S. Kanchibotla, and I. Brunton, in *Proceedings of Explo 2001 Conference, 2001*, edited by A. Marton (AusIMM, Carlton, 2001), p. 197.
- [6] N. Djordjevic, in *Proceedings of 6th International Symposium for Rock Fragmentation by Blasting, Johannesburg, 1999*, edited by The South African Institute of Mining and Metallurgy (SAIMM, Johannesburg, 1999), p. 213.
- [7] N. Djordjevic, Origin of blast-induced fines, *Min. Technol.* **111**, 143 (2002).
- [8] I. Onederra, S. Esen, and A. Jankovic, Estimation of fines generated by blasting—applications for the mining and quarrying industries, *Min. Technol.* **113**, 237 (2004).
- [9] See the Supplemental Material at <http://link.aps.org/supplemental/10.1103/PhysRevApplied.10.034001> for a schematic representation of the star-shaped crushed-zone model, Figure 1 and the detailed project application.
- [10] V. Svahn, Lic. thesis, Chalmers University of Technology, 2003.
- [11] A. Iravani, I. Kukolj, F. Ouchterlony, T. Antretter, and J. Åström, in *Proceedings of 12th International Symposium for Rock Fragmentation by Blasting, 2018*, edited by H. Schunnesson & D. Johansson (Luleå University of Technology, Luleå, 2018), p. 597.
- [12] D. Johansson, Lic. thesis, Luleå University of Technology, 2008.
- [13] J. A. Åström, Statistical models of brittle fragmentation, *Adv. Phys.* **55**, 247 (2006).
- [14] J. A. Åström, R. P. Linna, J. Timonen, P. F. Møeller, and L. Oddershede, Exponential and power-law mass distribution in brittle fragmentation, *Phys. Rev. E* **70**, 026104 (2004).
- [15] F. Ouchterlony and P. Moser, in *Proceedings of the 10th International Symposium for Rock Fragmentation by Blasting*, edited by K. Singh Pradeep & S. Amalendu (CRC Press/Balkema, Boca Raton, 2012), p. 65.
- [16] P. Moser, N. Cheimanoff, R. Ortiz, and R. Hochholdingner, in *Proceedings of the EFEE 1st World Conference of Explosives and Blasting Technique, Rotterdam, 2000*, edited by R. Holmberg (A.A. Balkema, Rotterdam, 2000), p. 165.
- [17] FWF project P27594-N29; see detailed project application at [9].
- [18] I. Kukolj, A. Iravani, F. Ouchterlony, C. Weiss, and J. Lubensky, in *Proceedings of 12th International Symposium for Rock Fragmentation by Blasting, Luleå, Sweden, 2018*, edited by H. Schunnesson & D. Johansson (Luleå University of Technology, Luleå, 2018), p. 483.
- [19] J. A. Åström, T. I. Riikilä, T. Tallinen, T. Zwinger, D. Benn, J. C. Moore, and J. Timonen, A particle based simulation model for glacier dynamics, *Cryosphere* **7**, 1591 (2013).
- [20] S. Nie, Swedish Rock Engineering Research Foundation SveBeFo Report No. 42.
- [21] P. Kekäläinen, J. A. Åström, and J. Timonen, Solution for the fragmentation-size distribution in a crack-branching model of fragmentation, *Phys. Rev. E* **76**, 026112 (2007).
- [22] T. I. Riikilä, T. Tallinen, J. A. Åström, and J. Timonen, A discrete-element model for viscoelastic deformation and fracture of glacial ice, *Comput. Phys. Commun.* **195**, 14 (2015).
- [23] R. Ouyed, J. Staff, and P. Jaikumar, Quark-novae in low-mass x-ray binaries with massive neutron stars: A universal model for short-hard gamma-ray bursts, *Astrophys. J.* **729**, 60 (2011).
- [24] A. Stern, A. Adcroft, and O. Sergienko, The effects of Antarctic iceberg calving-size distribution in a global climate model, *J. Geophys. Res.: Oceans* **121**, 5773 (2016).
- [25] D. Sornette, *Critical Phenomena in Natural Sciences: Chaos, Fractals, Selforganization and Disorder: Concepts and Tools* (Springer Science and Business Media, Berlin, 2006).
- [26] A. Billi, On the extent of size range and power law scaling for particles of natural carbonate fault cores, *J. Struct. Geol.* **29**, 1512 (2007).
- [27] J. F. Kok, A scaling theory for the size distribution of emitted dust aerosols suggests climate models



- underestimate the size of the global dust cycle, *PNAS* **108**, 1016 (2011).
- [28] R. Mahmoodi Baram, H. J. Herrmann, and N. Rivier, Space-Filling Bearings in Three Dimensions, *Phys. Rev. Lett.* **92**, 044301 (2004).
- [29] J. A. Åström and J. Timonen, Spontaneous formation of densely packed shear bands of rotating fragments, *Eur. Phys. J. E* **35**, 40 (2012).
- [30] D. E. Grady and M. E. Kipp, Geometric statistics and dynamic fragmentation, *J. Appl. Phys.* **58**, 1210 (1985).
- [31] B. A. Wills and J. Finch, *Wills' Mineral Processing Technology: An Introduction to the Practical Aspects of Ore Treatment and Mineral Recovery* (Butterworth-Heinemann, Oxford, 2015).
- [32] F. Kun and H. J. Herrmann, Transition from damage to fragmentation in collision of solids, *Phys. Rev. E* **59**, 2623 (1999).
- [33] J. Åström, M. Kellomäki, and J. Timonen, Dynamic fragmentation of a two-dimensional brittle material with quenched disorder, *Phys. Rev. E* **55**, 4757 (1997).
- [34] S. Esen, I. Onederra, and H. A. Bilgin, Modelling the size of the crushed zone around a blasthole, *Int. J. Rock Mech. Min. Sci.* **40**, 485 (2003).
- [35] F. Ouchterlony, The Swebrec function: Linking fragmentation by blasting and crushing, *Min. Technol.* **114**, 29 (2005).
- [36] F. Ouchterlony, in *Proceedings of 9th International Symposium on Rock Fragmentation by Blasting, Leiden, 2009*, edited by J. A. Sanchidrián (CRC Press / Taylor & Francis Group, London, 2009), p. 3.
- [37] F. Ouchterlony, U. Nyberg, P. Bergman, and S. Esen, in *Proceedings of 4th EFEE World Conference Explosives and Blasting Technique, Vienna, 2007*, edited by P. Moser (European Federation of Explosives Engineers, UK, 2007), p. 47.
- [38] A. Miklantsch, Dipl. thesis, Montanuniversität Leoben, Austria, 2002.
- [39] G. Reichholf, PhD thesis, Montanuniversität Leoben, Austria, 2003.
- [40] P. Moser, M. Olsson, F. Ouchterlony, and A. Grasedieck, in *Proceedings of EFEE 2nd World Conference on Explosives and Blasting Technique, 2003*, edited by R. Holmberg (Rotterdam, Balkema, 2003), p. 449.
- [41] H. C. Grimshaw, in *Proceedings of Mechanical Properties of Non-Metallic Materials, 1985*, edited by W. H. Walton (Butterworths, London, 1985), p. 380.
- [42] F. Ouchterlony, U. Nyberg, M. Olsson, I. Bergqvist, L. Granlund, and H. Grind, in *Proceedings of EFEE 2nd World Conference Explosives and Blasting Technique, 2003*, edited by R. Holmberg (Rotterdam, Balkema, 2003), p. 193.
- [43] J. A. Sanchidrián and L. M. López, in *Proceedings of EFEE 2nd World Conference Explosives and Blasting Technique, 2003*, edited by R. Holmberg (Rotterdam, Balkema, 2003), p. 357.
- [44] J. A. Sanchidrián, P. Segarra, F. Ouchterlony, and L. M. López, On the accuracy of fragment size measurement by image analysis in combination with some distribution functions, *Rock. Mech. Rock. Eng.* **42**, 95 (2009).
- [45] J. A. Sanchidrián, P. Segarra, L. M. López, and F. Ouchterlony, in *Proceedings of 9th International Symposium on Rock Fragmentation by Blasting, 2009*, edited by J. A. Sanchidrián (CRC Press / Taylor & Francis Group, Leiden, 2009), p. 239.
- [46] J. A. Sanchidrián, F. Ouchterlony, P. Moser, P. Segarra, and L. M. López, Performance of some distributions to describe rock fragmentation data, *Int. J. Rock Mech. Min. Sci.* **53**, 18 (2012).
- [47] J. J. Gilvarry, Fracture of brittle solids. I. Distribution function for fragment size in single fracture (theoretical), *J. Appl. Phys.* **32**, 391 (1961).
- [48] H. J. Steiner, in *Proceedings of 17th International Mining Processing Congress, Dresden, 1991* (Bergakademie Freiberg, Freiberg, 1991), p. 177.
- [49] F. Ouchterlony and P. Moser, in *Proceedings of 8th International Symposium on Rock Fragmentation by Blasting, Chile, 2006*, edited by S. A. Editec (Ediarte S.A., Chile, 2006), p. 207.
- [50] S. P. Michaux, Sub-populations and patterns in blast induced fine fragmentation, *Miner. Eng.* **22**, 576 (2009).
- [51] Z. X. Zhang, S. Q. Kou, L. G. Jiang, and P.-A. Lindqvist, Effects of loading rate on rock fracture: Fracture characteristics and energy partitioning, *Int. J. Rock Mech. Min. Sci.* **37**, 745 (2000).
- [52] P. K. V. V. Nukala, S. Zapperi, M. J. Alava, and S. Šimunović, Crack roughness in the two-dimensional random threshold beam model, *Phys. Rev. E* **78**, 046105 (2008).
- [53] S. Morel, E. Bouchaud, J. Schmittbuhl, and G. Valentin, R-curve behavior and roughness development of fracture surfaces, *Int. J. Fracture* **114**, 307 (2002).
- [54] M. H. B. Nasser, G. Grasselli, and B. Mohanty, Fracture toughness and fracture roughness in anisotropic granitic rocks, *Rock. Mech. Rock. Eng.* **43**, 403 (2010).
- [55] A. Grasedieck, PhD thesis, Montanuniversität Leoben, Austria, 2006.
- [56] D. Johansson, PhD thesis, Luleå University of Technology, Sweden, 2011.
- [57] D. E. Grady and M. E. Kipp, in *High-Pressure Shock Compression of Solids. High-Pressure Shock Compression of Condensed Matter*, edited by J. R. Asay & M. Shahinpoor (Springer, New York, 1993).
- [58] J.-T. Wang, Tailored pulse loading method, *Sci. China A* **32**, 120 (1989).
- [59] F. Dai, PhD thesis, University of Toronto, 2010.
- [60] M. H. B. Nasser, F. Rezanezhad, and R. P. Young, Analysis of fracture damage zone in anisotropic granitic rock using 3D X-ray CT scanning techniques, *Int. J. Fracture* **168**, 1 (2011).
- [61] A. Scott, S. Michaux, and I. Onederra, in *Proceedings of 9th International Symposium on Rock Fragmentation by Blasting, 2009*, edited by J. A. Sanchidrián (CRC Press / Taylor & Francis Group, Leiden, 2009), p. 663.
- [62] Z. P. Bažant, J.-L. Le, F. R. Greening, and D. B. Benson, What did and did not cause collapse of WTC twin towers in New York, *ASCE J. Eng. Mech.* **134**, 892 (2008).

7

**Paper III:**

**Tracing the origin of fines generated in blasting**

This page intentionally left blank.



# Using Small-scale Blast Tests and Numerical Modelling to Trace the Origin of Fines Generated in Blasting

Ivan Kukolj, Armin Irvani, and Finn Ouchterlony

Chair of Mining Engineering and Mineral Economics, Montanuniversitaet Leoben, Leoben, Austria

Received August 30, 2018; accepted September 5, 2018; published online September 25, 2018

**Abstract:** Waste fines from rock breakage often negatively influence economics and environment. The Austrian Science Fund (FWF) sponsors a project to investigate the cause of the fines by studying blast fragmentation throughout small-scale blast tests and numerical simulations. The tests include blast-loading confined granite and mortar cylinders by detonating cord with 6, 12, and 20 g/m of PETN. The blast-driven dynamic cracking at the end face of the cylinder opposite to the initiation point is filmed with a high-speed camera. The filming is followed up by an analysis of surface and internal crack systems and sieving of the blasted cylinders to quantify the amount of fine material created. The numerical simulations cover the blast fragmentation of a mortar cylinder. These simulations use Finite and Discrete Element Methods (FEM, DEM) with explicit time integration. The model cylinders are loaded by a pressure evolution acting on the borehole wall. Both methods produce realistic crack patterns, consisting of through-going radial cracks with crack intersections around a crushed zone at the borehole. Furthermore, the DEM models have also yielded realistic fragment size distributions (FSD). The paper covers the present progress of the ongoing project and related future work.

**Keywords:** Blast-induced fines, Blast tests, High-speed photography, FEM, DEM, Dynamic cracking, Blast fragmentation

**Untersuchungen zur Entstehung von sprenginduzierten Feinanteilen anhand von kleinmaßstäblichen Sprengversuchen und numerischer Modellierung**

**Zusammenfassung:** Bei Gesteinssprengungen entstehende, nicht verwertbare Feinanteile haben oft einen negativen Einfluss auf Umwelt und Wirtschaftlichkeit. Der Österrei-

chische Wissenschaftsfonds (FWF) fördert ein Projekt zur Untersuchung der Ursache von Feinanteilen durch Analyse der Zerkleinerung in kleinmaßstäblichen Sprengversuchen und numerische Modellierung. Die Tests umfassen Sprengversuche an Granit- und Mörtelzylindern mit 6, 12 und 20 g/m PETN Sprengschnur. Die dynamische Rissbildung an der dem Initiationspunkt gegenüberliegenden Stirnseite des Zylinders wird mit einer Hochgeschwindigkeitskamera aufgenommen. Im Anschluss an die Aufnahme erfolgt eine Analyse der oberflächlichen und inneren Rissysteme sowie eine Siebanalyse des gesprengten Materials, um die Masse des entstehenden Feinmaterials zu quantifizieren. Die numerischen Simulationen modellieren die Zerkleinerung eines Mörtelzylinders. Es werden Finite- und Diskrete-Elemente-Methoden (FEM, DEM) mit expliziter Zeitintegration verwendet. Die Modellzylinder werden durch eine, auf die Bohrlochwand wirkende, Druckentwicklung belastet. Beide Methoden produzieren realistische Rissmuster, bestehend aus durchgehenden radialen Rissen mit Rissübergängen (Vereinigung und Unterteilung) rund um eine Zermalmungszone am Bohrloch. Darüber hinaus haben die DEM-Modelle auch eine realistische Korngrößenverteilung geliefert. Der Beitrag behandelt den aktuellen Fortschritt des laufenden Projekts sowie damit verbundene zukünftige Arbeiten.

**Schlüsselwörter:** Sprenginduzierte Feinanteile, Sprengversuche, Hochgeschwindigkeitsfotografie, FEM, DEM, Dynamische Rissbildung, Sprengzerkleinerung

## 1. Introduction

The amounts of mineral fines that are associated with raw materials extraction have practical consequences. One concern is the sustainability of natural resources since fines are often an unsellable liability or waste that has cost money and energy to produce and in the end has to be deposited. This reasoning lay behind the EU project Less Fines [1]. The health aspects of mineral fines have again come into focus, so sources of respirable dust and miti-

I. Kukolj, MSc (✉)  
 Chair of Mining Engineering and Mineral Economics,  
 Montanuniversitaet Leoben,  
 Erzherzog-Johann-Str. 3,  
 8700 Leoben, Austria  
[ivan.kukolj@unileoben.ac.at](mailto:ivan.kukolj@unileoben.ac.at)

Fig. 1: Volume of crushed material around an extended 2D blast-hole (Fig. 2 in [7]); the crushed zone volume  $V_c$  is annular and the breakage zone volume  $V_b$ , which also generates crushed fines, is made up of the  $n$  partial volumes of the star arms

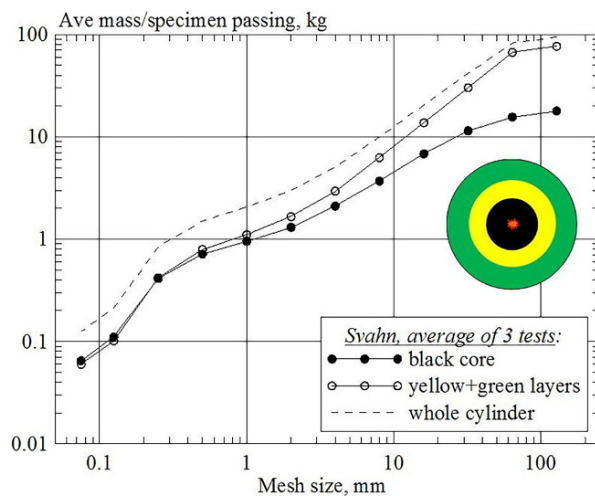
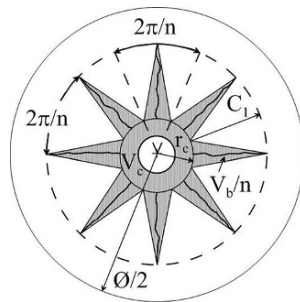


Fig. 2: Sieving curves for blasted multilayered  $\text{Ø}300 \times 600$ -mm cylinders of mortar; comparison of  $\text{Ø}120$ -mm black core with yellow ( $\text{Ø}120$ – $200$  mm) + green layers ( $\text{Ø}200$ – $300$  mm) [8]

gation effects are studied in the ongoing EU Horizon 2020 project “Sustainable Low Impact Mining, SLIM” [2, 3].

Blasting is a major producer of waste fines, crushing and milling another. Blasting is a highly dynamic process and the crack growth that defines breakage is a major source of fines. Such crack-generated fines (CGF) are also produced by crushing and grinding. Fines are inherently related to the amount of energy required in comminution. Most of the area created resides in the fines and this area then determines the consumed comminution energy [4]. A better knowledge of how CGF are generated may also help to improve blasting and crushing practices and to suppress the amount of CGF at the source rather than dealing with them afterwards.

Blast generated fines are often considered to originate mainly from the annular crushed zone around a blast hole, which contains only  $\sim 1$  mm material, and fragmentation models were built around this; e.g. the CZM or crush zone model [5, 6]. It implies that fragment size is (almost) solely defined by the distance to the blast hole, the finest material created at the borehole wall and fragment size, thus, increasing with distance from the blast hole. The circu-

Fig. 3: Post-blast cross section through blasted confined mortar cylinder [9]

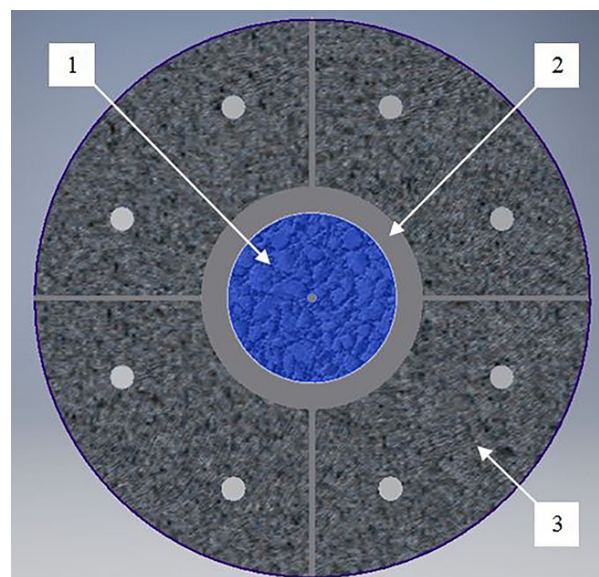
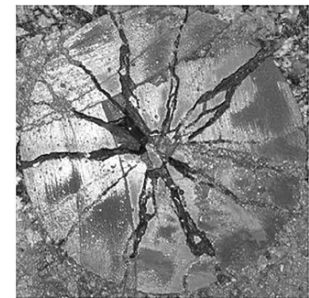


Fig. 4: Prepared blast chamber (transverse cross-section) (1—Blast cylinder; 2—Damping layer; 3—Blast chamber)

lar crushed-zone model was extended to a star-shape one (Fig. 1; [7]).

Blasting tests with layered cylinder specimens [8] contradict the predictions of the star-shaped CZM (Fig. 2). Firstly, the sieving curves for the layers are quite similar in shape and the core region contains fragments well beyond 1 mm in size. Secondly, there is a cross-over point (0.25 mm in Fig. 2) above which the outer layers contain more fine material than the core. Consequently, more  $\sim 1$  mm fines are created outside the black core than inside it.

Post-mortem crack patterns are not as simple either as the CZM (Fig. 3; [9]). Here the cracks have seemingly run along crooked paths, branched, merged, and left debris along the crack paths.

Statistical models of brittle fragmentation [10, 11] point in the same direction, that instability of fast propagating cracks leaves behind a trace of small fragments along their propagation paths, but this has not been observed in rock under blasting-like conditions. More arguments are provided in [12].

This led to the FWF-sponsored project P27594-N29: “Fines generated by dynamic crack propagation, as in blasting of rock-like materials,” which ends Dec 31, 2018.

TABLE 1  
Measured material properties

Property	Granite		Mortar		Damping	
	Mean	St.dev	Mean	St.dev	Mean	St.dev
UCS [MPa]	171.50	9.00	27.70	1.10	–	–
Brazilian tensile strength [MPa]	10.85	1.52	2.90	0.49	–	–
Density [g/cm <sup>3</sup> ]	2.70	0.01	1.66	0.01	2.12	0.08
Young's modulus [GPa]	65.30	0.83	12.20	0.31	–	–
Poisson's ratio [–]	0.24	0.02	0.23	0.05	–	–
<i>P</i> -wave velocity [m/s]	4908	111	3069	62	1210	274
<i>S</i> -wave velocity [m/s]	3212	150	2065	40	643	79

Two main project objectives are to: i) determine the importance of the dynamic mechanism for CGF by capturing images of branching at a moving crack tip and ii) compare the measured fragment size distribution (FSD) with models based either on the mechanism of crack branching and merging or other mechanisms. The first part of this project is described in [13, 14], progress in numerical simulations in [15], and the present state in this paper. It is divided into an experimental part and a part with numerical simulations.

## 2. Methodology

### 2.1 Small-scale Blast Tests

The blast tests [13] include controlled blast loading of a confined hollow cylinder whilst the resulting dynamic cracking is filmed at its frontal end face by means of high-speed photography.

The cylinder is made of mortar or granite,  $\varnothing 150 \times 300$  mm in size, with a  $\varnothing 10$ -mm central axial borehole. The production of the blast cylinders is described in [13].

The loading is achieved by detonating a decoupled PETN (*Pentaerythritol tetranitrate*) cord (6, 12, or 20 g/m) inside the borehole. The detonation propagates along the cord towards a stemming plug at the frontal end face with the velocity (VOD) of about 7300 m/s [16].

The cylinder is radially confined by a 25-mm-thick damping layer inside a blast chamber (Fig. 4). The damping material [13] is a commercial concrete mixture, cured for one day. It improves the acoustic-impedance matching of propagating shock waves and protects the chamber.

Table 1 shows measured material properties of the blast cylinders and the damping layer.

The blast chamber (Fig. 5) includes four concrete segments, axially connected with two metal plates. The segments are designed to radially move about 5 mm during the blast, acting as 'impulse traps' [17]. The rear metal plate includes an opening for inserting the cord. The frontal metal plate includes an opening, allowing filming of the frontal end face through a protective polycarbonate window.

The filming [13] captures crack development at the end face following the detonation. The cracking at the end face starts about when the detonation front reaches the stemming plug, which is seen as slight movement of the plug and occasionally a dimmed detonation-flash around it.

The filming set-up (Fig. 6) records the dynamic crack development, in most cases, with 24,656 fps at  $336 \times 336$  pixels.

## 2.2 Numerical Modelling

### 2.2.1 Modelling in Abaqus

Numerical modelling of blast fragmentation was done using the finite element method (FEM) and the discrete element method (DEM) [14]. The FEM approach (Abaqus) is suitable for modelling blast-induced damage, though presently quite limited for fragmentation analysis [14].

### 2.2.2 HiDEM Model

Blast cylinders are modelled with a 3D discrete element code (HiDEM) [11, 18]. A dynamic sedimentation method is used to generate the initial random structure of the model composed of rigid spheres of 2-mm and 3-mm diameter. Contacts between the particles are modelled using massless beams. The interaction potential between two particles is defined by the Euler-Bernoulli (EB) beam model. Estimates of the beam elastic energy are provided in [18]. The beams break due to exerted tension, shear, or bending beyond the fracture limit (Fig. 4 in [18]).

The particle-motion equation is given in [14]. The model assumes elastic-material behaviour. The stiffness matrix for linear-elastic EB beams under small deformation is provided in [18]. The modelled material has an elastic modulus of  $E = 19.7$  GPa and a Poisson's ratio of  $\nu = 0.19$ , which is somewhat representative of the blast-test mortar. The stochastic mechanical behaviour of granular disordered materials was modelled using beams with reduced stiffness. These beams were randomly selected to have their stiffness reduced to 10% of the original value. Here, the fracture criterion [11, 18] was described by the elastic-strain threshold  $\varepsilon_{crit} = 0.0003$ .

The modelled mortar cylinders are  $\varnothing 140 \times 280$  mm in size with a  $\varnothing 10$ -mm borehole. The blast loading is radially applied onto the borehole wall according to a pressure-time function [14]. The modelled VOD is the same as in the blast tests. A simplified post-peak pressure drives all particles outwards with  $P_{post} = 0.0025P_{peak}$ . The modelling uses three peak pressures of 166 MPa, 85 MPa, and 35 MPa, equiva-

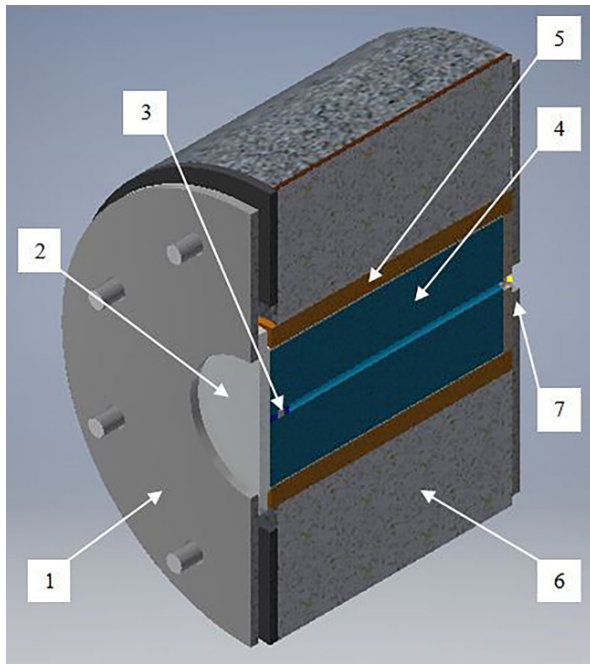


Fig. 5: Prepared blast chamber (axial cross-section) (1—Frontal end metal plate; 2—Protective window; 3—Borehole with stemming; 4—Blast cylinder; 5—Damping layer; 6—Chamber segment; 7—Rear-end metal plate)

lent to 20 g/m, 12 g/m, and 6 g/m of PETN [14]. In addition, 20 mm of stemming was included. Quiet boundary conditions are applied to the mantle to avoid cracking due to reflected tensile waves.

### 2.2.3 Simplified $n(s)$ Model

When blasted, the cylinder expands radially, inducing tangential tension and tensile cracks. In the crushing process, fragments are broken by continual shear deformation [19]. Such a process has a power-law FSD  $n_{\text{crush}}(s)ds = C_1 s^{-\beta} ds$  [11], where  $C_1$  is a constant and  $\beta$  indicates the degree of crushing/grinding, being  $\beta \sim 1.8\text{--}3.5$  when dimension  $D=3$  [11, 15]. Dimensionless size  $s$  is measured in number of grains composing a fragment [15].

The dynamic tensile cracks can easily become unstable, branch, and further merge, forming fragments. This inherently-universal process leads to a characteristic FSD [11, 20]. The number of fragments  $n_{\text{bm}}(s)$  of size  $s$  in an interval  $ds$  can be written as  $n_{\text{bm}}(s)ds = C_2 s^{-\alpha} \exp(-s/C_3)ds$  with  $\alpha = (2D-1)/D$ , where  $C_2$  and  $C_3$  are non-universal constants [11, 15].

If  $n(s)$  describes the number-density of fragments with  $s$  number of grains, the FSD, or the number of fragments in a size-interval  $ds$ , can then be written as [15]:

$$n(s)ds = C_1 s^{-\beta} ds + C_2 s^{-\alpha} \exp(-s/C_3)ds + n_b(s)ds \quad (1)$$

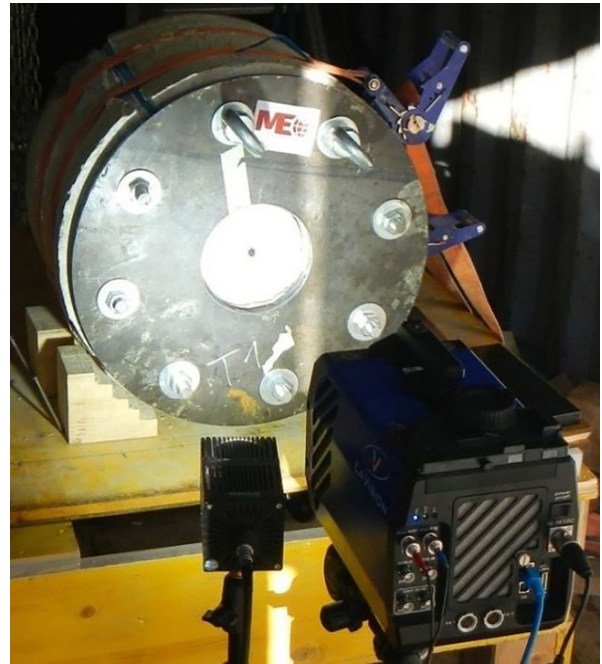


Fig. 6: High-speed filming set-up for the blast tests

where the boulder intensity  $n_b$  is given by the characteristic boulder size  $s_b$  and

$$n_b(s) = \exp(-s/s_b) \quad (2)$$

With the proper transformation from  $s$  to  $r$ , i.e.  $ds \propto r^2 dr$  for  $D=3$ , leaving the exponential part of the second term in the  $n(s)$  formula and integrating the  $n(s)$ , the mass passing fraction at screen size  $r$  (MPF( $r$ )) can be approximated for fragments smaller than boulders [15]:

$$\text{MPF}(r) = f_{\text{cr}} [1.0 - (r/r_{\text{grain}})^{-3\beta+6}] + f_{\text{bm}} (r/r_{\text{max}})^{-2\alpha+6} \quad (3)$$

where  $f_{\text{bm}}$  and  $f_{\text{cr}}$  determine the mass fraction of fragments formed in the branching-merging and the crushing process,  $r_{\text{grain}}$  is the approximated diameter of the material grain size, and  $r_{\text{max}}$  is the approximated diameter of the largest fragment.

## 3. Preliminary Results

### 3.1 Crack Patterns

The high-speed images (Fig. 7) show more intensive cracking with the increase of charge. Similarly, crack patterns are denser and develop earlier in granite than in mortar. The high-speed images of both mortar and granite shots show three phases of crack development [13].

Firstly, following the plug movement, initial cracks emerge and propagate mainly in the radial direction. In

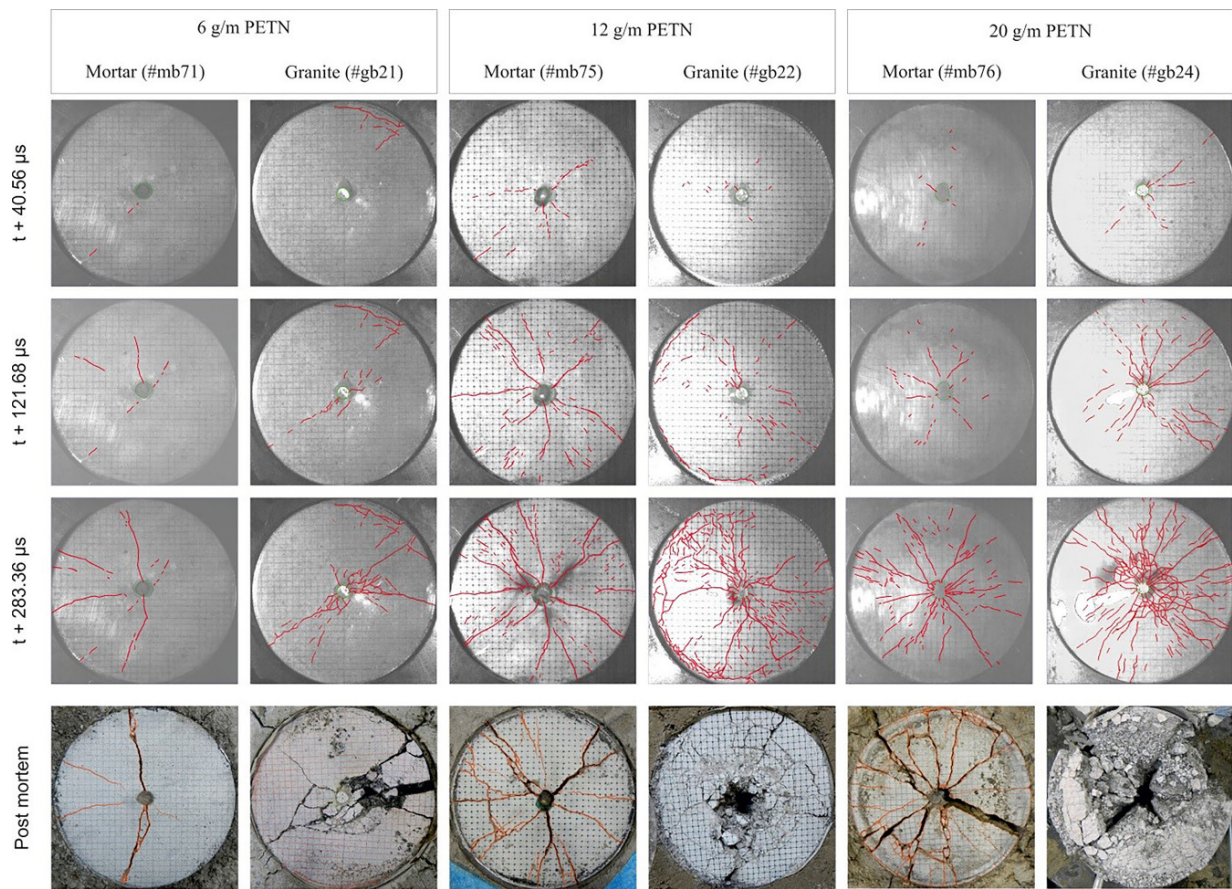


Fig. 7: High-speed and post-mortem end-face images of the cylinders with respect to the charge and material

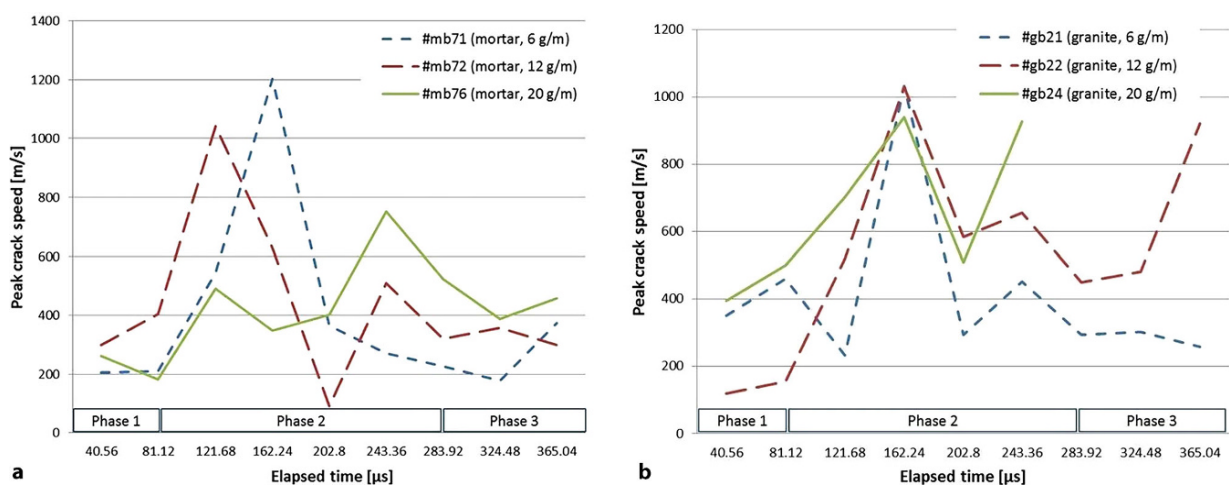


Fig. 8: Peak crack speed in blast cylinders with respect to material, charge amount, and elapsed time (a Mortar curve set; b Granite curve set)



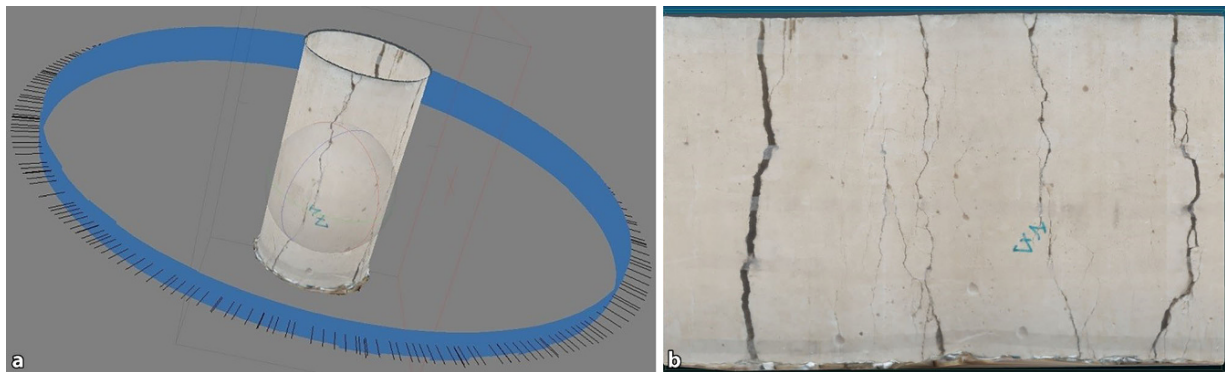


Fig. 9: Post-mortem mantle image (a Processing; b "Unfolded" mantle, cylinder #mb71)

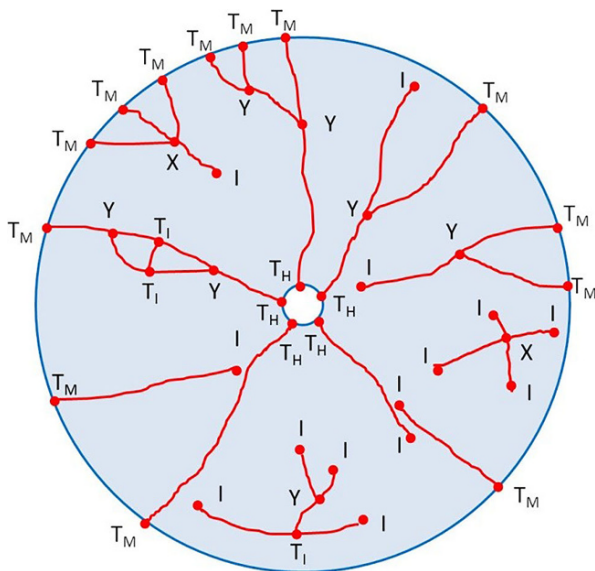


Fig. 10: Topological representation of crack-pattern features

the second phase, the crack-propagation speed reaches its peak and quickly drops with multiple cracks branching-merging (Fig. 8). After the second phase, the main cracks have reached the borehole and/or the mantle and end-face spalling with fumes leakage may occur.

The post-mortem crack patterns are observed at the end face (Fig. 7), on the mantle, and internally through computer tomography (CT) [13].

The mantle crack patterns are firstly photographed and then processed in Agisoft PhotoScan® to produce a 3D model of the mantle, which is then projected onto a 2D image for further analysis (Fig. 9).

So far the CT cross-sections and mantle images indicated that the number of main cracks and the number of main intersections basically do not change in the axial direction [13].

The crack patterns in the high-speed and post-mortem images are traced and topologically analysed, similarly as in [21]. This includes decomposition of a crack network into topological features (Fig. 10): branches, crack intersections

( $J_{int}$ : X, Y, and  $T_I$ ), borehole intersections ( $T_H$ ), mantle intersections ( $T_M$ ), and crack-end nodes (I).

The analysis quantifies the development of the features in the images with respect to time, from  $40.56\mu s$  to  $527.28\mu s$  and finally to the post-mortem state (pm). The results are presented in a ternary diagram with respect to the percentage of the feature categories (Fig. 11).

The results show that the percentage of crack intersections rapidly increases and the percentage of end nodes drops during the second phase, as the initial smaller cracks coalesce.

The number of active end nodes (i. e. propagating crack tips) and intersections both increase with the increase of charge and more so in granite than in mortar.

Fig. 12 shows resulting 3D crack networks from the modelling with respect to the three loading levels at  $t = 400\mu s$ . By increasing the loading level, the internal damage intensity increases. Accordingly, the crack system becomes more complex, increasing in number of main radial cracks and intersections.

### 3.2 Fragmentation Analysis of Blasted Cylinders

Fig. 13 shows sieving FSD curves of selected blast cylinders. The curves shift upwards to contain larger fractions of fines when the charge is increased, in accordance with the Natural Breakage Characteristics (NBC) properties [4]. The curve-fitting procedure is ongoing.

### 3.3 Numerical Estimates of Fragmentation and Fines Sources

Fig. 14 shows FSD curves obtained with HiDEM modelling. A fragment is defined by the number of connected particles  $N$  and the screen size is that of the diameter of a volume-equivalent sphere. The curves represent the mass-passing fraction of the model for different blast-loading levels. The curve with  $P_{peak} = 166\text{MPa}$  is similar to the sieving curves and well approximated by the Swebrec function [22]. The FSD curves from the DEM simulations also show an NBC-like relationship.

Fig. 11: Results from the topological analysis (cylinder #mb75); the data points relate to crack-pattern state with respect to elapsed time

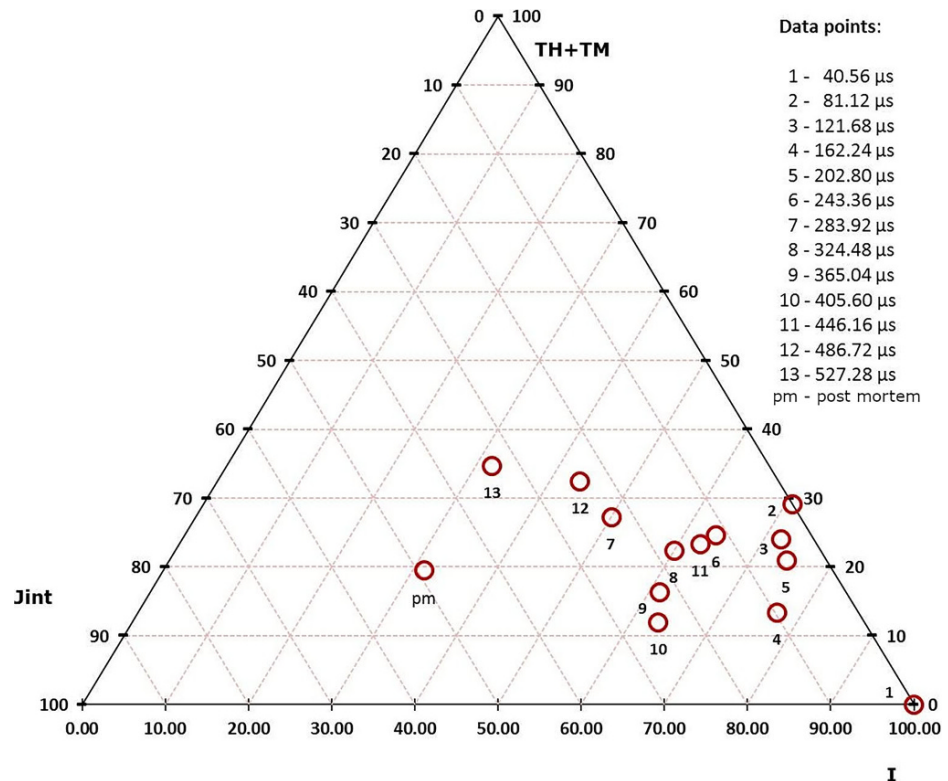
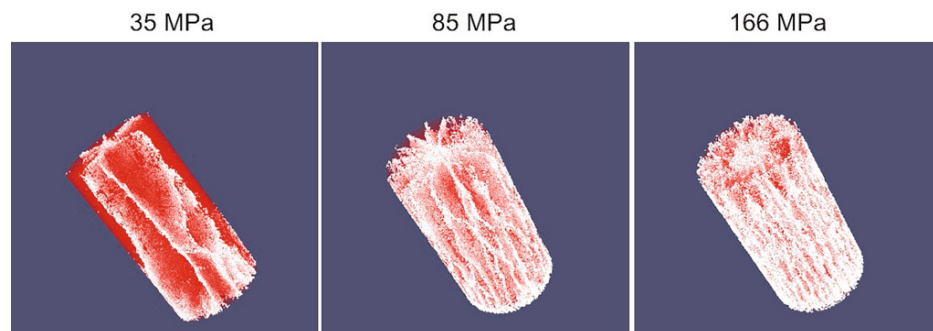


Fig. 12: Crack patterns of modelled cylinders



At 35 MPa and 85 MPa, the mass-passing curves indicate the “dust and boulders” phenomenon. The curve with  $P_{\text{peak}}=35\text{ MPa}$  contains 94% of the cylinder mass in one boulder. The curve with  $P_{\text{peak}}=85\text{ MPa}$  contains a wider range of fragment sizes and four boulders, with almost 50% of the cylinder mass. This results from blasting below the critical charge level [9, 12].

By using Eq. 3, the percentage mass fraction of fragments formed by branching-merging and crushing [15] can be determined for the results (Table 2). The size of the branching-merging fragments ranges from a single DEM particle to a maximum value, which depends on the applied loading level. Similar to the MPF, the size of these fragments is approximated by the diameter of the volume equivalent sphere.

Simulations have also been conducted with radially-layered mortar cylinders, like those in [8]. The cylinders are

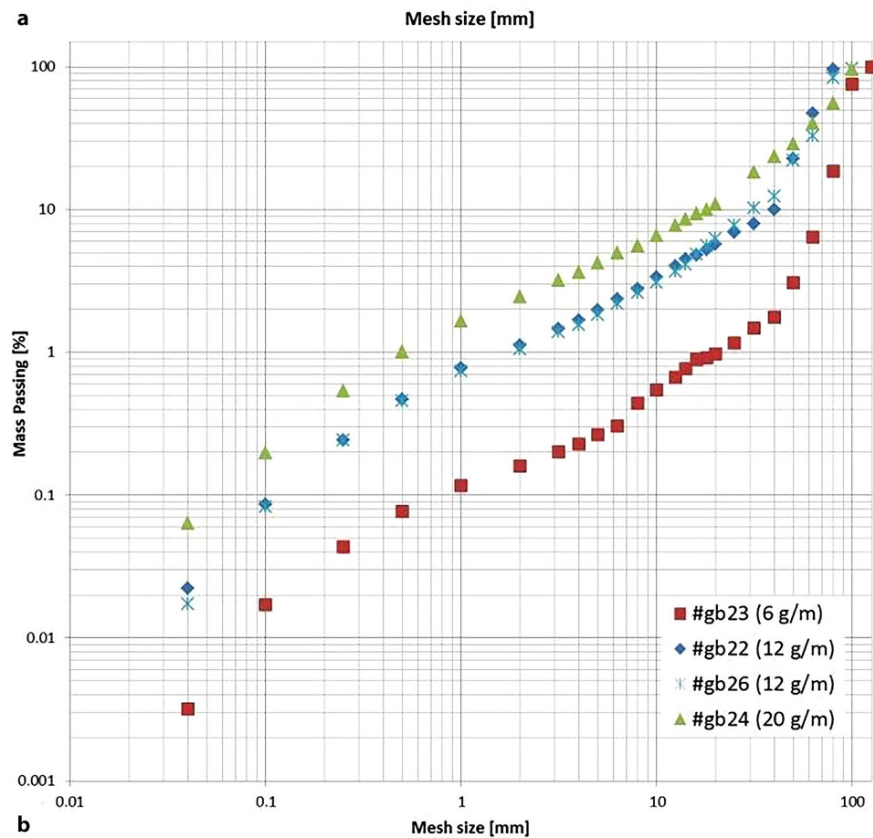
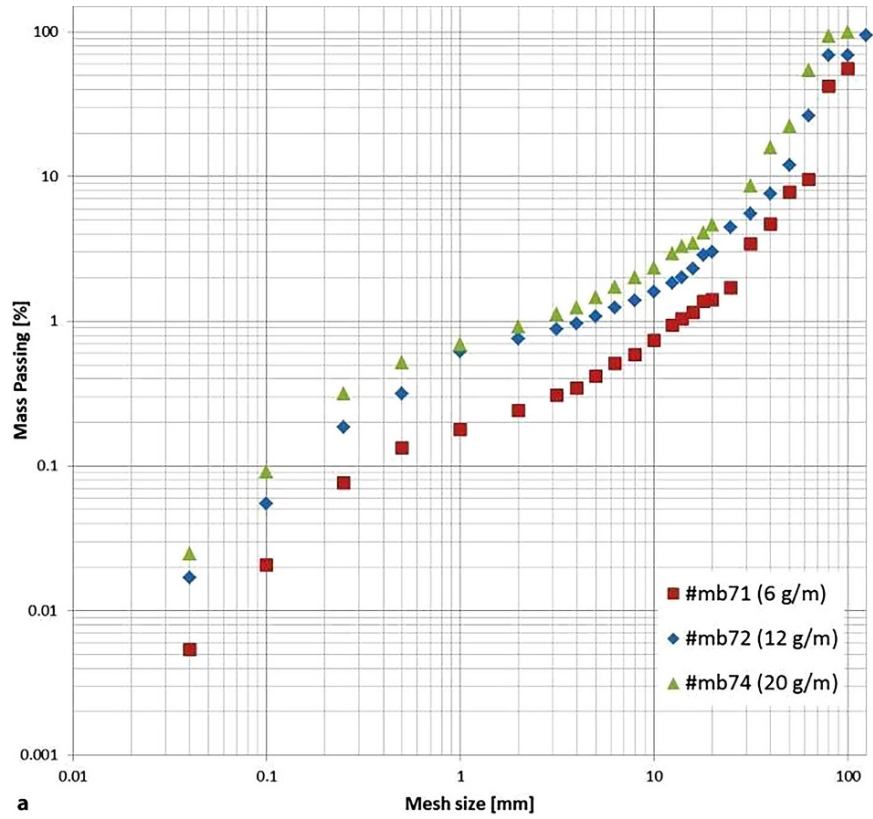
banded at radii  $r=30\text{ mm}$  and  $r=50\text{ mm}$ , creating three concentric regions. A routine calculates the absolute mass of very fine particles containing only one DEM particle in each region. Fig. 15 shows that the absolute mass of the fines in region 3 ( $50\text{ mm}<r<70\text{ mm}$ ) is larger than in region 1 ( $5\text{ mm}<r<30\text{ mm}$ ), thus confirming the results from [8].

#### 4. Conclusions

The ongoing project studies dynamic mechanisms behind blast-induced fines.

The filming shows a three-phase crack-pattern development. The main cracks and intersections in mortar are more numerous and appear earlier with higher charge and the same tendencies are observed in granite, but at a higher level. They are detectable before the third phase and do

Fig. 13: Selected sieving curves of blasted cylinders (a Mortar curve set; b Granite curve set)



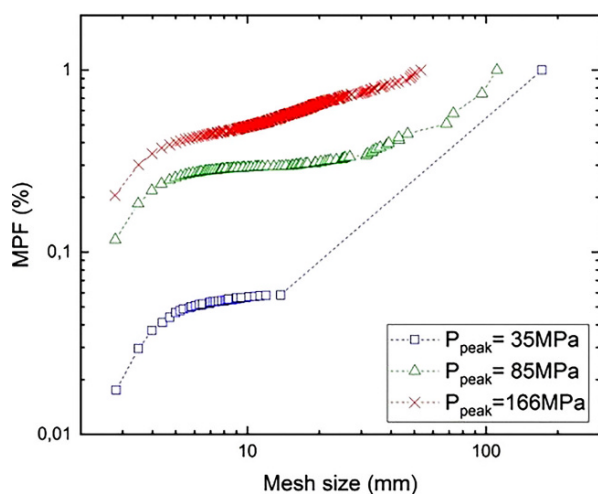


Fig. 14: FSD curves of modelled cylinders

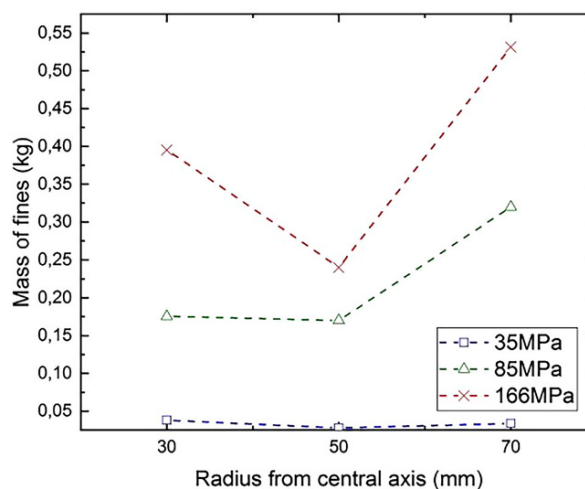


Fig. 15: Absolute mass of fine-particles with respect to the radius from the borehole

TABLE 2 Percentage mass fraction of fragments formed by crushing, branching-merging, and in boulders					
$P_{\text{peak}}$	Fragment mass percentage [%]				Max. diameter of branching-merging fragments $r_{\text{max}}$ [mm]
	Crushing	Branching-merging	Boulders	Branching-merging (<10 particles)	
35	4.5	1.5	94	0.5	14.1
85	26.5	19.6	53.9	1.1	70.9
166	37.5	55.3	7.1	4.3	52.4

not significantly change in the axial direction. Although the crack speed is higher in mortar [13], crack patterns develop with more propagating crack tips in granite.

The numerical modelling has used the finite element method (Abaqus) and the discrete element method (HiDEM) with explicit time integration to model the dynamic crack propagation, branching and merging, and blast fragmentation of mortar cylinders. The FEM simulations provided results on dynamic 2D crack propagation, whereas the 3D behaviour has been more successfully simulated with the DEM code (HiDEM).

The HiDEM code provides realistic FSD results of blasted mortar cylinders, focusing on three major fragmentation mechanisms: borehole crushing, branching-merging, and secondary crushing of branching-merging fragments. The modelling results are in general agreement with the layered-cylinder blast results [8].

The FSD sieving curves of both blasted and modelled cylinders follow reasonably well the NBC parallel upward shift with the charge increase.

Future work will include further topological analysis of the images, analysis of blast-induced 3D crack patterns, determining other possible fines-generating mechanisms acting in the high-speed images, and further fragmentation analysis of the modelled and the blasted cylinders, including laser diffractometry for the grain sizes below 40  $\mu\text{m}$ . The comparison of the simulation results with the blast-test results will take place after necessary calibrations. The final

results will determine the relative influence of observed dynamic mechanisms on the fines generation and a discussion of how the fines could be suppressed.

**Acknowledgements.** The project is funded by Austrian Science Fund (FWF): P27594-N29. The authors would like to thank Dr. Jan Åström (CSC-IT, Espoo, Finland), Prof. Thomas Antretter, Prof. Christian Weiss, Jan Lubensky, and Gerold Wölfler (Montanuniversität Leoben) for their help and support.

**Funding.** Open access funding provided by Montanuniversität Leoben.

**Open Access** This article is distributed under the terms of the Creative Commons Attribution 4.0 International License (<http://creativecommons.org/licenses/by/4.0/>), which permits unrestricted use, distribution, and reproduction in any medium, provided you give appropriate credit to the original author(s) and the source, provide a link to the Creative Commons license, and indicate if changes were made.

## References

- Moser, P.: Less fines in aggregate and industrial minerals production – results of a European research project, in: Holmberg, R. (ed.): Proceedings of 3<sup>rd</sup> EFEE World Conference on Explosives and Blasting, England: EFEE, 2005, pp 567–574
- Ouchterlony, F.; Sifferlinger, N. A.; Brechelmacher, A.: Das europäische Horizon 2020-Forschungsprojekt “Sustainable Low Impact Mining – SLIM”, BHM Berg- und Hüttenmännische Monatshefte, 163 (2018), Nr. 2, pp 52–56
- Sanchidrián, J. A.: SLIM: Technology for blasting to improve mining, in: Schunnesson, H.; Johansson, D. (eds.): Proceedings of 12<sup>th</sup> International Symposium on Rock Fragmentation by Blasting, 2018, pp 783–793

4. Steiner, H. J.: The significance of the Rittinger equation in present-day comminution technology, in: Proceedings of 17<sup>th</sup> International Mineral Processing Congress, Bd I, 1991, pp 177–188
5. Thornton, D.; Kanchibotla, S. S.; Brunton, I.: Modelling the impact of rockmass and blast design variation on blast fragmentation, in: Marton, A. (ed.): Proceedings of Explo 2001 Conference, AusIMM: Carlton (u.a.), 2001, pp 197–205
6. Esen, S.; Onederra, I.; Bilgin, H. A.: Modelling the size of the crushed zone around a blasthole, *International Journal of Rock Mechanics and Mining Sciences* 40(2003), pp 485–495
7. Onederra, I.; Esen, S.; Jankovic, A.: Estimation of fines generated by blasting—applications for the mining and quarrying industries, *Mining Technology, Transactions of the Institute of Mining and Metallurgy A*:113 (2004), pp A1–A11
8. Svahn, V.: Generation of fines in bench blasting, Lic. thesis, Gothenburg, Chalmers Univ. Technology, Dept. of Geology, Publication A104, 2003
9. Johansson, D.: Fragmentation and waste rock compaction in small-scale confined blasting, Lic. thesis 2008:30, Luleå: Luleå Univ. Technology, 2008
10. Åström, J. A.; Ouchterlony, F.; Linna, R. P.; Timonen, J.: Universal dynamic fragmentation in D dimensions, *Physical review letters* 92(2004), Nr. 24, pp 245506–1/4
11. Åström, J. A.: Statistical models of brittle fragmentation, *Advances in Physics* 55(2006), Nr. 3–4, pp 247–278
12. Ouchterlony, F.; Moser, P.: On the branching-merging mechanism during dynamic crack growth as a major source of fines in rock blasting, in: Singh, P. K.; Sinha, A. (eds.): *Rock Fragmentation by Blasting*, Proceedings of 10<sup>th</sup> International Symposium on Rock Fragmentation by Blasting, USA, Boca Raton (u.a.): CRC Press, 2012, pp 65–75
13. Kukulj, I.; Iravani, A.; Ouchterlony, F.; Weiss, C.; Lubensky, J.: Filming blast fragmentation of rock and mortar cylinders, in: Schunnesson, H.; Johansson, D. (eds.): *Rock Fragmentation by Blasting*, Proceedings of 12<sup>th</sup> International Symposium on Rock Fragmentation by Blasting, 2018, pp 483–494
14. Iravani, A.; Kukulj, I.; Ouchterlony, F.; Antretter, T.; Åström, J.: Modelling blast fragmentation of cylinders of mortar and rock, in: Schunnesson, H.; Johansson, D. (eds.): *Rock Fragmentation by Blasting*, Proceedings of 12<sup>th</sup> International Symposium on Rock Fragmentation by Blasting, 2018, pp 597–610
15. Iravani, A.; Åström, J. A.; Ouchterlony, F.: Physical origin of the fine-particle problem in blasting fragmentation, *Physical Review Applied*, 10, 034001 (2018). <https://doi.org/10.1103/PhysRevApplied.10.034001>
16. Schimek, P.: Improvement of fragmentation by blasting, Diss., Leoben, Montanuniv., Lehrst. f. Bergbaukunde, Bergtechnik und Bergwirtschaft, 2015
17. Sun, C.: Damage zone prediction for rock blasting, Doctoral Thesis, The University of Utah, Dept. of Mining Engineering, 2013
18. Åström, J. A.; Riikilä, T.I.; Tallinen, T.; Zwinger, T.; Benn, D.; Moore, J. C.; Timonen, J.: A particle based simulation model for glacier dynamics, *The Cryosphere* 7(2013), Nr. 5, pp 1591–1602
19. Åström, J. A.; Timonen, J.: Spontaneous formation of densely packed shear bands of rotating fragments, *The European Physical Journal E* 35 (2012), p 40
20. Kekäläinen, P.; Åström, J. A.; Timonen, J.: Solution for the fragmentation-size distribution in a crack branching model of fragmentation, *Physical Review E* 76, 026112 (2007)
21. Sanderson, D. J.; Nixon, C. W.: The use of topology in fracture network characterization, *Journal of Structural Geology* 72 (2015), pp 55–66
22. Ouchterlony, F.: Fragmentation characterization: the Swebrec function and its use in blast engineering, in: Sanchidrián, J. A. (ed.): *Rock Fragmentation by Blasting*, Proceedings of 9<sup>th</sup> International Symposium on Rock Fragmentation by Blasting, Spain, Granada (u.a.): CRC Press, 2009, pp 3–22

**Paper IV:**

**Origin of fines particle in blasting fragmentation:  
unstable tensile crack growth type**

This page intentionally left blank.

# Generation of fine fragments during dynamic propagation of pressurized cracks

A. Iravani<sup>1</sup>, F. Ouchterlony<sup>1</sup>, I. Kukolj<sup>1</sup>, J.A. Åström<sup>2</sup>

<sup>1</sup>Dept. Mineral Resources Engineering, Montanuniversität Leoben, A8700 Leoben, Austria

<sup>2</sup>CSC - IT-center for science, P.O.Box 405, FIN-02101, Esbo, Finland

(Dated: January 14, 2020)

High-resolution numerical simulations of cracks driven by an internal pressure in a heterogeneous and brittle granular medium produce fragment-size distributions with the same characteristics as experiments on blasted cylinders of mortar and rock in both the fine- and the intermediate-size fragment-regions. To mimic full-scale blasts used e.g. within the mining industry, the cracks propagate in a medium that is either under compression, neutral or under tension. In a compressive environment, shear fracture produce a large volume of fines, while in a neutral or tensile environment, unstable crack-branching is responsible for a much smaller volume of fines. The boundary between the fines and the intermediate size fragments scales as the average grain size of the material. The ultimate goal is to develop a blasting process that minimize the fines, which in mining are both an environmental hazard and useless for further processing.

## I. INTRODUCTION

A fundamental process within the mining industry is the blasting of rock to extract minerals. This process creates a lot of dust that cannot be processed further and that is also an environmental hazard. It would therefore be of great significance to minimize the dust which is often called 'fines'. The blasting process is carried out by drilling cylindrical holes and blasting them from within. The blast creates a conical compressive shock wave that travels outward in the radial direction of the cylinder. As the hole expands outward, it will induce tension in the tangential direction. The stress waves emanating from the borehole will sooner or later reach a boundary or an interface between two dissimilar materials. Here, the specific acoustic impedance of the host rock plus the angle of wave incidence define the stress waves interaction at the boundary such as mode transformation, transmission, reflection and refraction [1]. Reflected waves often meet cracks initiated by the primary wave. In this way, propagating cracks may experience both compressive and tensile environments that influence the fines production.

Well-known theories within mining engineering for blast-induced fines typically postulate compressive and/or shear failure as the main mechanism for fine fragments production such as the crushed zone model (CZM) [2], the two component model (TCM) [3] and the additions to CZM by Onederra et al. [4]. However, when blasting cylinders of a given size with decreasing amount of explosives, a critical charge size is eventually reached. At this point, the cylinder barely falls apart into a few large blocks plus a small volume of very fine fragments [5, 6]. In such a case, a crushed zone around the borehole and crushing due to fragment collisions normally do not occur and the theories fail. An inspection of the outcome of such experiments reveals that the fines originate along the propagation paths of the cracks that create the large blocks. This indicates that the key to understanding the blast-induced fines production can be found in the de-

tailed modeling of cracks driven by the internal pressure induced by the blast and propagating in a medium that is under externally applied stresses that can be either compressive or tensile.

Within the physics community, fragmentation research has typically been concentrated around the possible universality of scale-invariant power-law FSDs. There seems to be limited universality, but there are dependencies on dimensions, and compressive or impact fragmentation seems to behave differently than tensile fragmentation [7–11].

In this article we report the results of blasting experiments and numerical simulations of propagating cracks driven by internal pressure and propagating under specific external stress-states that mimic realistic conditions for full-scale blasting. The model materials are granular both in the simulations and in the experiments with a average granularity of the order of 0.1 mm. The main difference between the experiments and the simulations is that in the simulations the grains are indestructible, while in the experiments the grains can fragment and there is also an inter-granular matrix that can form fragments much smaller than the typical grain size. Nevertheless, we are able to demonstrate that the FSDs for experiments and simulations are very similar and that they can be understood in terms of universal processes.

Here we find that the granularity length scale determines a boundary between fines- and intermediate-size fragments. In the intermediate size-region, the FSD has the universal form of the crack branching-merging process, while in the fines region the FSD has the form induced by shear crushing if the external stresses are compressive, and a branching-merging process if the external stresses are tensile or neutral. In the latter case, the boundary between the two regions appear as an off-set in the FSD. As a consequence we find that the total volume of fines in blasting are affected by the granularity of the material that is blasted, the stress environment of the propagating cracks, and the total charge used in the



blast.

## II. FRAGMENTATION THEORY

The magnitude of the external compressive stresses surrounding a pressurized crack has direct influence on its speed of propagation. For example, a high compressive stress that acts perpendicular to the crack flanks reduces the propagating velocity of the crack tip. Depending on the magnitude of the compressive stress and the crack's driving force the velocity may eventually drop below the critical branching velocity of the material  $V_c$  [12]. This process may lead to crack closure and at even higher compressive stresses cause crushing by compressive shear. In compressive shear, the debris will be crushed into decreasingly smaller fragments by grinding and compaction. This process may perhaps be conceptualized as a hierarchical process in which ever smaller fragments are broken to fill pore space that opens up in continuous shear deformation [13, 14], or it may have similarities with impact fragmentation [10, 11]. In both cases the FSD can be approximated by a power-law fragment size distribution of the form  $n_{crush}(s)ds \propto s^{-\beta}ds$ , where the exponent  $\beta$  depends on the material and the specific way it is fragmented, and may takes values roughly in the range 1.8 – 3.5 [7, 11]. Dimensionless size  $s$  is here measured in number of grains in fragments of a granular material.

In the absence of externally applied compressive stresses suppressing the propagating crack, the velocity of the crack propagation increases to a value close to  $V_c$  where the crack begins to branch [12]. Crack branches readily merge to form fines as can be seen in Fig. 3. This branching-merging process is inherently universal and leads to a characteristic FSD [7, 15]. This can be written as  $n_{bm}(s)ds \propto s^{-\alpha} \exp(-s/s_i)ds$ , with  $\alpha = (2D - 1)/D$ , where  $D$  is dimension (i.e.  $D = 2, 3$  for membranes and bulk objects, respectively) [7, 15, 16]. The branches propagate for a short distance and are arrested in the stress free wake region created by the main propagating crack [12] inducing a size cut-off defined by  $s_i$ . The size cut-off is here approximated by an exponential function [15].

At the scale of the grain size in a granular material we expect that the processes for fines formation described above are highly influenced by the granularity of the material. At larger scales, we expect the material to behave like a continuous material. It is thus reasonable to postulate that, in a granular material, there needs to be separate terms in the FSD for fragments at and below the grain sizes,  $s_f$ , and for larger, intermediate-size fragments,  $s_i$ . For the blasting scenarios investigated here we expect that the fines are created by either crushing or crack branching-merging, while the intermediate-size fragments appear as a result of crack branching-merging only. In principle, there could obviously be crushing also at the intermediate-size scale, but within the context investigated here, this does not happen.

The largest fragments, often called boulders, are the ones delineated by the main cracks. The main cracks can typically be assumed to propagate independent of each other and thereby to form a Poisson process [17], which induces an exponential term at the largest sizes of the FSD,  $n_b(s)ds \propto \exp(-s/s_b)ds$ , where  $s_b$  sets the characteristic size of the boulders.

This would give the following options for the FSDs, with right-hand side terms describing fines, intermediate-size fragments, and boulders, respectively:

$$n(s)ds = C_1 s^{-\beta} ds + C_2 s^{-\alpha} \exp\left(-\frac{s}{s_i}\right) ds + C_3 \exp\left(-\frac{s}{s_b}\right) ds, \quad (1)$$

which we would expect to appear for blasting under externally applied compressive stress, while in a tensile environment we would expect:

$$n(s)ds = C_1 s^{-\alpha} \exp\left(-\frac{s}{s_f}\right) ds + C_2 s^{-\alpha} \exp\left(-\frac{s}{s_i}\right) ds + C_3 \exp\left(-\frac{s}{s_b}\right) ds, \quad (2)$$

where  $C_1, C_2$  and  $C_3$  are constants that determine the relative weights of the different fragment size regions.

A good way to estimate the validity of Eqs. (1, 2) is to relate them to the Mass Passing Fraction ( $MPF(x)$ ) that is the common function used to characterize fragmentation results within the mining community [18]. The  $MPF(x)$  is defined as the fraction of mass for a collection of fragments that passes through successive set of sieves with decreasing mesh sizes  $x$ . That is, for a mesh size  $x = 0$ ,  $MPF(x) = 0.0$ , and  $MPF(x > x_{max}) = 1.0$  or 100%, where  $x_{max}$  is the largest fragment.

With the transformation  $s \approx (x/x_{grain})^3$ ,  $ds = 3x^2/x_{grain}^3 dx$  for  $D = 3$ , the  $MPF(x)$  can be written:

$$MPF(x) = \frac{m_{grain}}{M_0} \frac{3}{x_{grain}^3} \int_{x_{grain}}^x x'^3 n(s(x')) x'^2 dx', \quad (3)$$

where  $M_0$  is the total mass,  $x_{grain}$  is the grain-size of the material, and  $m_{grain}$  the mass of a grain. This equation can be written as a sum of two incomplete Gamma functions. It is however more useful to examine Eq. (3) in the case where  $n_b(s)$  is neglected and the exponential parts of the first two terms in Eqs. (1, 2) are replaced by limited ranges of integration. That is, the first term is assumed to be valid within the interval:  $[x_{grain}, x_{trans}]$ , and the second term within  $[x_{trans}, x_{max}]$ , where  $x_{trans} \propto s_f^{1/3}$  is the transition size between fines and intermediate-size fragments (cf. Fig. 1(b)), and  $x_{max} \propto s_b^{1/3}$  is the maximum size of boulders. If we neglect the term of the order  $x_{grain}/x_{max}$ , we get for the  $MPF(x)$ :

$$MPF(x) = f_{fp} \left( \left( \frac{x}{x_{grain}} \right)^{-3\langle\alpha,\beta\rangle+6} - 1.0 \right) + f_{ip} \left( \frac{x}{x_{max}} \right)^{-3\alpha+6}, \quad (4)$$

where  $\langle\alpha,\beta\rangle$  means either  $\alpha$  or  $\beta$  depending on which  $n(s)$  equation, i.e. Eqs. (1, 2), is used. The factors  $f_{fp}$ , and  $f_{ip}$  are constants:

$$f_{fp} = \frac{m_{grain}}{M_0} \frac{3C_1}{-3\langle\alpha,\beta\rangle+6}, \quad (5)$$

$$f_{ip} = \frac{m_{grain}}{M_0} \frac{3C_2 x_{max}^{-3\alpha+6}}{\left( x_{grain}^{-3\alpha+6} \right) (-3\alpha+6)}. \quad (6)$$

For  $D = 3$  the value of  $-3\alpha + 6$  is equal to 1 and thus the second part on the right hand side of Eq. (4) becomes the empirical Gates-Gaudin-Schuhmann distribution (*GGSS*) [19] which is a power-law function with an exponent  $m = 1$ , and the first part represents the characteristic shape of MPFs for the fine fragments. This is consistent with the typical functional forms observed for MPFs: a non-universal shape for the fines, followed by a wider or a narrower interval described by the *GGSS*-function, and finally a non-universal shape for the boulders. Representative examples are displayed in Fig. 1(a). A method of the reverse transformation from  $MPF(x)$  to  $n(s)$  is given in Appendix A.

### III. EXPERIMENTS

#### A. Experimental setup

We perform a set of blasting experiments and together with data from earlier experiments we have fragmentation data for 28 controlled blasting experiments of cylinders of sandstone [20], granite, mortar and magnetic mortar (MM) [6]. The cylinders are blasted from within a central borehole along the axis of the cylinder. There are three different outer boundary conditions: (1) at the outer boundary of the cylinders there is a layer of aggregate under a 1 MPa pressure, a so-called pre-stressed aggregate [6], (2) a momentum trap (MT) [21, 22] which at the outer boundary absorbs much of the incident compressive wave induced by the blast, and (3) an ‘unconfined’ or a free outer boundary at which the initial compressive wave is reflected as a tensile wave. The logic behind studying these different outer boundary conditions is to model different blasting scenarios with the cracks forming in tensile, neutral and compressive environments.

Details of the experiments are listed in Table I. The table is sorted by the sieving technique. Initially the post-mortem cylinders are mechanically sieved with minimum

mesh sizes of either 0.063 mm or 0.04 mm to a maximum fragment size until a full MPF curve is formed. The fine fragments of the experiments E1 and E2 were apart from mechanical sieving also measured using a laser diffraction method (LDM) with a resolution down to  $0.4 \mu\text{m}$ . The results from LDM were then merged with the mechanical sieving data thus forming a wider range FSD. These are listed as E6 and E7. The fine fragments of the experiment tests listed in E5 were also additionally measured using a sedimentation method [20].

**Table I:** Experimental configurations

No.	Material	No. of blasted cylinders	Charge density/ Specific charge (g/m) / (kg/m <sup>3</sup> )	Confinement	Minimum mesh size (mm)
mechanical sieving					
E1	Mortar	3	6, 12, 20	MT	0.04
E2	Granite	3	6, 12, 20	MT	0.04
E3	MM[6]	5	3, 5, 10, 20, 40	unconfined	0.063
E4	MM[6]	4	5, 10, 20, 40	pre-stressed aggregate	0.063
+ sedimentation					
E5	Sandstone[20]	6	0.46, 0.444, 0.431, 0.231, 0.218, 0.22	unconfined	0.002
+ laser diffraction					
E6	Mortar	3	6, 12, 20	MT	0.0004
E7	Granite	4	6, 12, 20	MT	0.0004

#### B. Experimental results

A pre-stressed and a momentum trap  $MPF(x)$  are displayed in Fig. 1(a) together with fits to Eq. (3). The theoretical  $MPF(x)$  functions are obtained by numerical integration and with a constant material grain size  $x_{grain}$ . For real materials,  $x_{grain}$  is obviously not a constant (cf. Fig. 3). The  $x_{grain}$  values used are listed in the last column in Table I as the ‘Minimum mesh size’. The deviation between the experimental and the theoretical MPFs for the smallest fragments is a result of the theory assuming a minimum fragment size of a single grain, while the experimental data lumps all masses smaller than the resolution into a single point.

The same data in the  $n(s)$  form is displayed in Fig. 1(b). The difference between pre-stressed and MT boundary conditions become evident when presented in this form: (i) In the fine-fragments region of the pre-stressed cylinder the FSD has a much steeper slope with a power-exponent  $\beta \approx 2.2$  as indicated in the figure. For the cylinder confined by MT the exponent is the expected  $\alpha \approx 5/3$ . (ii) At a fragment size of  $s \sim 10^2$  for the pre-stressed case there is a cross-over to the branching-merging power-law  $\alpha \approx 5/3$ , while for the MT case there appears the same power-exponent for both fines and intermediate fragment sizes but there is an off-set to lower fragment number by about an order of magnitude at  $s \sim 10^3$ . (iii) There are cross-overs to exponential FSDs

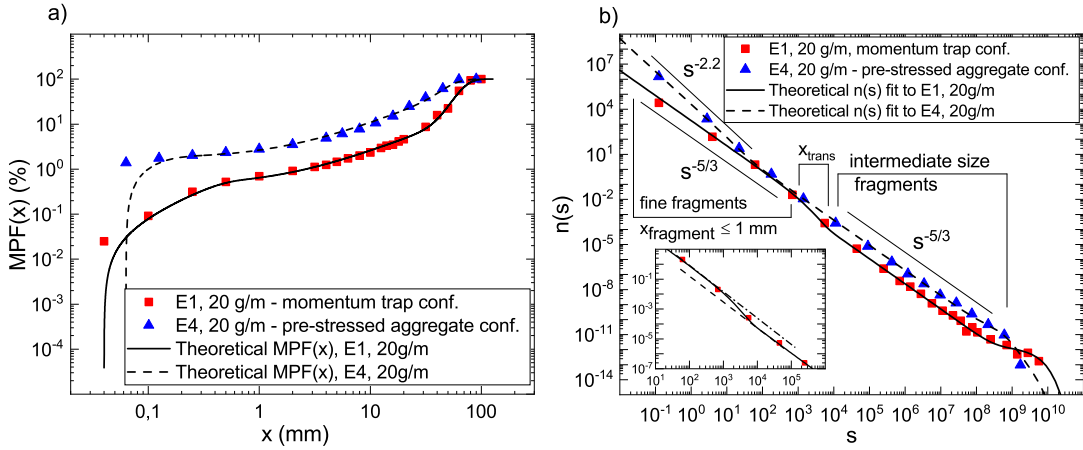


**Figure 1:** a) Two sets of experimental MPFs: red squares and blue triangles, and the two corresponding theoretical  $MPF(x)$ -fits: the solid and the dashed black lines. The data correspond to two blasted cylinders confined by MT (E1) [21, 22] and pre-stressed (E4) [6] boundary conditions, respectively. b) The corresponding  $n(s)$  for the same data together with fits to Eqs. (1, 2). Here, the first data point on the  $s$  axis refers to the smallest detectable fragment.

in both cases at the boulder size. There is a more pronounced boulder part for the MT case and the boulders are slightly bigger. In the intermediate fragment-size region, i.e.  $x_{\text{trans}} < x < x_{\text{boulders}}$ , the power-exponents are identical  $\alpha \approx 5/3$ , but there are more intermediate-size fragments for the pre-stressed case.

With these results it becomes evident that the more interesting case from a blasting technology point of view is the MT boundary condition, as it produces significantly less fines than the pre-stressed case.

In order to test the statistical significance of the off-set in the FSD of the cylinders confined by MT we perform statistical analysis to determine whether the slopes (gradients) of the two fitted power-laws for the fine fragments and the intermediate size fragments, are significantly different and whether the off-set between these lines is significant [23].

**Table II:** Regression analysis, E7: 20 g/m and E5: 0.444 kg/m<sup>3</sup>

Fitting region	Fine fragments region	Intermediate size fragments region
Equation	$\ln(C_1) + \alpha \ln(s)$	$\ln(C_3) + \alpha \ln(s)$
Parameter		
<b>E7</b>		
$\ln(C_1)$	$3.59 \pm 0.25$	-
$\ln(C_3)$	-	$2.04 \pm 0.69$
$\alpha$	$-1.695 \pm 0.021$	$-1.669 \pm 0.022$
R-squared	0.9969	0.9977
Adj. R-squared	0.9967	0.9975
<b>E5</b>		
$\ln(C_1)$	$6.80 \pm 0.19$	-
$\ln(C_3)$	-	$5.49 \pm 1.24$
$\alpha$	$-1.687 \pm 0.020$	$-1.742 \pm 0.045$
R-squared	0.9991	0.9966
Adj. R-squared	0.9990	0.9959

For the analysis we first use two sets of data: 1) the

wider range FSD obtained by LDM for granite (E7) blasted with 20 g/m of PETN with 23 data points forming the fine fragments region, and 2) the data from sedimentation of fine fragments of sandstone (E5) blasted with 0.444 kg/m<sup>3</sup> with 8 data points forming the fine fragments region. The reason for the choice of these two data sets is to lessen the inherent systematic error of each sieving technique on the resultant FSDs. Here, for the analysis, the data points between the two lines, if any, and also the ones forming the boulder part are not considered, see Fig. 2(a) and (b). The results of the linear regression are given in Table II.

**Table III:** Statistical significance study of the fines and intermediate size fragments' fitted lines, E7: 20 g/m and E5: 0.444 kg/m<sup>3</sup>

Test	Fine fragments region	Intermediate size fragments region
<b>E7</b>		
No. of data points	23	17
R	-0.998	-0.998
p(R)	$8.42E-28$	$1.09E-20$
Residual variance	F = 6.818	p(F) = 0.0002
Gradient	F = 1.691	p(F) = 0.202
Intercept	F = 4.556	p(F) = 0.039
<b>E5</b>		
No. of data points	8	7
R	-0.999	-0.998
p(R)	$2.03E-10$	$2.28E-7$
Residual variance	F = 3.277	p(F) = 0.090
Gradient	F = 1.439	p(F) = 0.255
Intercept	F = 21.45	p(F) = 0.0005

The results of the statistical analysis for the significance of the two fitted power-law lines are given in Table III. The two large correlation coefficients ( $|R| \approx 1$ ) and their highly significant p-values, i.e. p(R), indicate the

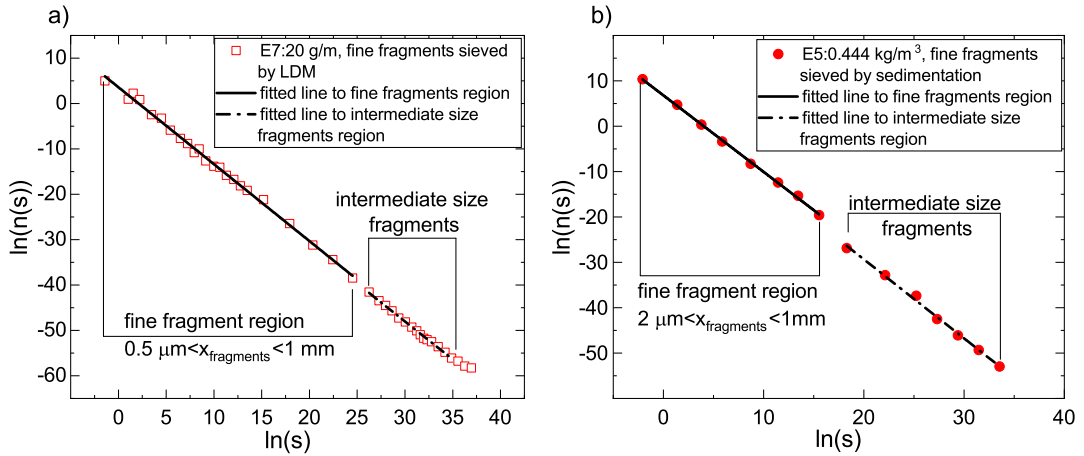


**Figure 2:** Two fitted lines of fine fragments region and intermediate size fragment region shown as solid and dashed lines, respectively. In a) the data points (square symbols) correspond to the experiment E7 with 20 g/m of PETN, and in b) the data points (filled circles) correspond to the experiment E5 with 0.444 kg/m<sup>3</sup>, see Table I. The regression function and parameters of these fits are listed in Table II.

existence of the two legitimate lines to compare. The p-value of the residual variance for experiment (E7) illustrates a significant difference between the two variances. Napier-Munn [23] suggests considering smaller value of  $p(F)$  for gradient and intercept tests. The comparison of the gradients with  $p(F) = 0.202$  emphasizes that the two lines are parallel, i.e. difference in the slope values is statistically insignificant. The small p-value of the intercept suggests that a real separation exists between the two parallel lines.

We analyzed all available data sets, except those with the pre-stressed boundary condition, in the same fashion as above. In all the 24 data sets a significant off-set between the fine- and intermediate- size fragment's fitted lines exists and in 22 of them the fine- and intermediate-size fragment's fitted lines are parallel. The two data sets that have different gradients are E5: 0.46 kg/m<sup>3</sup> and E5: 0.431 kg/m<sup>3</sup>. The exponent of the fine fragment size distribution for both these sets is  $\alpha \approx 5/3$ , but the intermediate-size one deviates slightly in these two cases. Consequently, with all data considered the experimental MPFs can be described by Eq. (2) unless the pre-stressed boundary condition is applied.

The post-mortem fractures and crack flanks of the blasted cylinders E1 and E2, see Table I, have been analyzed by scanning electron microscope (SEM). Figure 3 shows two images of crack branching and merging in granite (E2: 20 g/m) and mortar (E1: 12 g/m) both with a similar field of view of 0.179 mm × 0.785 mm. Figure 3(a) shows two radial cracks (radial in the sense of propagating in an outwards radial direction of the cylinder from the central borehole where the blast took place) that have propagated from the lower left corner (where the borehole is) and merged in the upper middle part of the image. This merging mechanism fragmented the corner material, i.e. just below the merging point, most

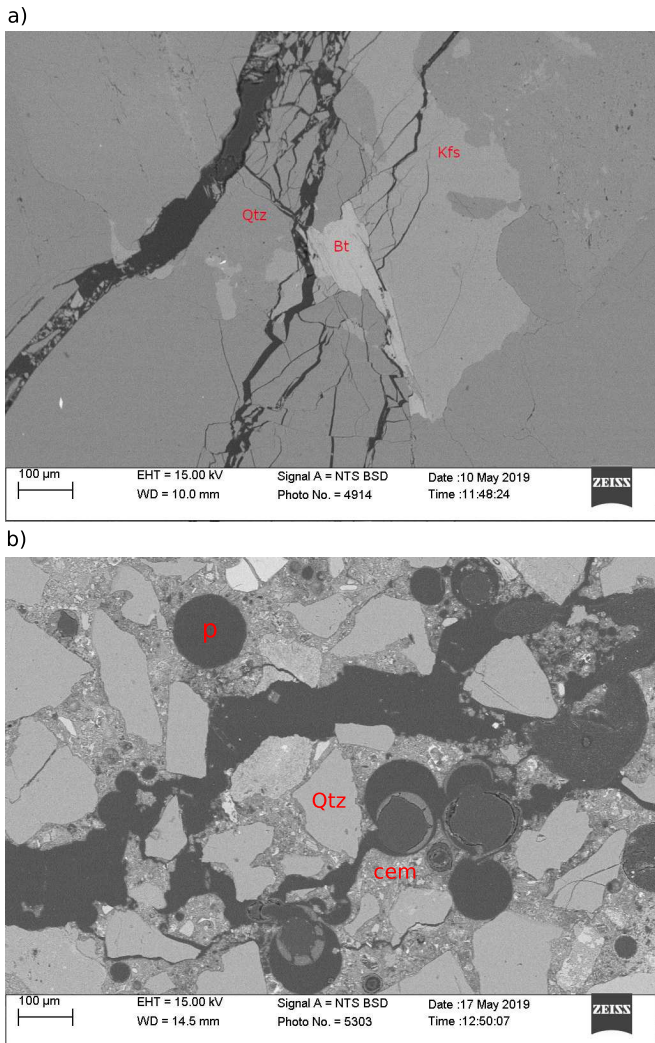
likely due to the brittleness of the quartz grain located there. The characteristic structure of the branching-merging process leading to scale-invariance is clearly visible in this figure: a large number of very small fragments are generated close to the main cracks, while larger but fewer fragments are generated further from the main cracks until the crack branches vanish at a characteristic cut-off size.

Figure 3(b) shows a region of a main radial crack propagated from the lower left (borehole) to the upper right corner of the image. The crack path, in this case, has fairly few microcracks compared to Fig. 3(a). However, the middle part of the crack includes branching cracks that follow grain boundaries that separate out some fragments. This illustrates how granularity influence fines formation.

## IV. COMPUTATIONS

### A. Numerical model

We use a customized version of the HiDEM code [24] which has been developed for numerical simulation of brittle fracture. In HiDEM, the materials are discretized by in-elastic spheres that are connected by mass-less elastic Euler-Bernoulli beams. In the version used here, the DEM particles are randomly packed using a dynamic deposition algorithm. The beams have square cross-sections  $w^2 \sim D_{particle}^2$ , length  $l \sim 2D_{particle}$  and Young's Modulus  $E = 19.7$  GPa. Due to the random packing, the number of beams connecting adjacent particles varies between 8 and 20. To mimic the experimental materials, initially, ten percent of the beams are randomly chosen to have their stiffness reduced to 10 percent of the value of an intact beam.



**Figure 3:** SEM pictures of the branching and merging mechanism and fragment formation in a) granite blasted with 20 g/m of PETN (E2) with quartz (Qtz), biotite (Bt) and K-feldspar (Kfs) grains indicated on the image, and b) mortar blasted with 12 g/m of PETN (E1) with quartz (Qtz), cement (cem) and pores (p) indicated.

We have used a fracture criterion composed of two parts: a) maximum strain criterion  $(L - L_0)/L_0$ , where  $L_0$  is the original length of a beam, and  $L$  the length of a stretched or compressed beam, and b) a pure bending part  $ABS(\theta_1 - \theta_2)$ , where  $\theta_1$  and  $\theta_2$  are rotations of the end-points of a beam. A beam breaks if deformation exceeds a threshold value for:  $(L - L_0)/L_0 + const \times ABS(\theta_1 - \theta_2)$ . The threshold value used is  $\varepsilon = 0.0003$ , i.e. typical tensile failure strain of mortar or concrete. We have tested also several other criteria including one in which we replace the rotation term with a shear term, however, the fragmentation results with this criterion match the experimental results best.

We do not have the computational resources to simulate the fragmentation of the full cylinders used in the experiments at high resolutions. With a grain size of the

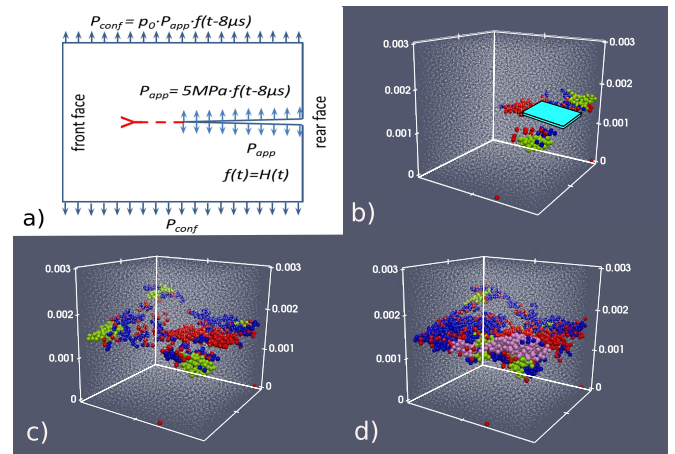


**Figure 4:** a) Schematic side view of the cube with a predefined crack,  $H(t)$  is the Heaviside function. b), c) and d) show the evolution of the fragmentation of the cube ( $3 \text{ mm} \times 3 \text{ mm} \times 3 \text{ mm}$ ) when  $p_0 = 0$  at  $t = 2 \mu\text{s}$ ,  $4 \mu\text{s}$  and  $8 \mu\text{s}$ , respectively. In b) the initial crack plane ( $1.5 \text{ mm} \times 1 \text{ mm}$ ) is shown in light blue. The cube's particles are shown with white points to improve the visibility of the fragments. Red: single particle fragments, blue: fragments containing two particles, green: fragments containing 3 to 10 particles, pink: fragments containing 11 to 100 particles. d) Represents the final stage of crack growth at  $t = 8 \mu\text{s}$ .

order of 0.1 mm and cylinders of size  $\varnothing 140 \text{ mm} \times 280 \text{ mm}$  they contain billions of particles. Instead, to capture the dynamic fragmentation process along propagating cracks we use the correct 0.1 mm resolution but compute fragmentation of small scale cubes. We use cubes of size  $3 \text{ mm} \times 3 \text{ mm} \times 3 \text{ mm}$  with particles of diameter 0.1 mm and  $6 \text{ mm} \times 6 \text{ mm} \times 6 \text{ mm}$  with particles of diameter 0.05 mm, 0.08 mm, 0.1 mm and 0.2 mm. We initiate cracks with a predefined mid-plane edge crack. The initial crack is horizontal and goes half way through the cube. To mimic the blasting process, a dynamic pressure is applied on the initial crack flanks with a value  $P_{app} = 5 \text{ MPa}$  for a duration of  $8 \mu\text{s}$ . To model the boundary conditions in the experiments there is an additional external stress  $P_{conf} = p_0 \times P_{app}$ , with  $p_0$  a constant that is applied on the top and bottom faces of the cube acting perpendicular to the crack flanks, see Fig. 4(a). As a representative example Fig. 4(b)-(d) illustrate the time evolution of the dynamic crack propagation and the fragmentation in the small cube for an unstressed condition,  $P_{conf} = 0 \text{ MPa}$ . The sample breaks into a large number of small fragments each composed of single or a few particles along the fracture plane due to the unstable tensile crack propagation induced by  $P_{app}$ , while the rest of the sample remains intact. The degree of fine fragments generation depends on the ratio  $p_0 = P_{conf}/P_{app}$  that may be both negative and positive for compression and tension, respectively.

We performed fragmentation computations of the smaller cube with external stresses in the range  $P_{conf} = -0.2P_{app}$  (compression) to  $+0.15P_{app}$  (tension), i.e.  $p_0 =$

**Table IV:** Regression data for the fine region of FSD for cube with the nine levels of external stresses. The values after  $\pm$  sign are standard error of the mean. Regression equation:  $\ln(C_1) + \alpha \times \ln(s) - s/s_f$

const. \ $p_0$	-0.2	-0.15	-0.1	-0.05	0	+0.05	+0.07	+0.1	+0.15
$\ln(C_1)$	6.32 $\pm$ 0.15	6.76 $\pm$ 0.28	7.10 $\pm$ 0.18	7.50 $\pm$ 0.15	7.68 $\pm$ 0.12	7.68 $\pm$ 0.20	7.78 $\pm$ 0.14	8.00 $\pm$ 0.087	8.14 $\pm$ 0.082
$\alpha$	-2.357 $\pm$ 0.082	-2.328 $\pm$ 0.444	-1.969 $\pm$ 0.227	-1.657 $\pm$ 0.245	-1.694 $\pm$ 0.263	-1.881 $\pm$ 0.250	-1.782 $\pm$ 0.220	-1.702 $\pm$ 0.185	-1.524 $\pm$ 0.175
$s_f$	2.62E30 $\pm$ 0.0	14.87 $\pm$ 21.60	11.10 $\pm$ 4.83	4.84 $\pm$ 1.26	5.07 $\pm$ 1.78	8.95 $\pm$ 3.46	7.12 $\pm$ 2.44	4.80 $\pm$ 1.13	4.24 $\pm$ 0.83
Adj. R-square	0.9893	0.9687	0.9862	0.9899	0.9918	0.9837	0.9907	0.9961	0.9963

-0.2 to +0.15 in steps of 0.05 plus  $p_0 = +0.07$ , altogether 9 values. This models the dynamics of a nucleated crack propagating in a heterogeneous medium with different local crack tip region stresses, which occurs during the dynamic crack propagation of blast induced cracks [25]. To average over several packing patterns, five different densely packed cubes were generated and fragmented for each external confinement pressure, i.e. external stresses, and their FSDs were added to each other to form a single FSD for each level of  $P_{conf}$ . We also computed FSDs for four larger cubes (6 mm $\times$ 6 mm $\times$ 6 mm) with varying resolution (particle size) and at  $p_0 = +0.15$  to investigate the influence of the characteristic size of the model cube, the DEM-particle size, and the influence of boundary fragmentation [11].

## B. Numerical results

Figure 5(a) shows the simulation results for the FSDs obtained with the nine external stress levels described above. In the figure, the theoretical  $n(s)$  are fitted to the data using Eqs. (1, 2) with the second term on the r.h.s. neglected. The fine fragments regions of the FSDs behave in the same way as in the experiments: The fine fragments power-law exponent is close to  $-5/3$  for positive  $p_0$ , and decreases to approximately  $-2.36$  for the smallest  $p_0$ . The exponential cut-off for the fines appear at  $s_f \sim 4 - 15$ . The larger fragments can either be described by an exponential or there are just a few separate very large boulders.

In the simulations with the three highest external tensile stresses, the fracture plane completely splits the cube, creating two or three large boulders at  $t \approx 7 \mu s$ . However, for the other stress levels a large number of fine fragments are generated but the cubes retained their integrity as the single largest fragment.

Fig. 5(b) shows only FSDs for  $p_0 = -0.2, 0.0, 0.15$  to highlight the change in the power-exponent for the fines. Table IV lists the regression analysis results for the computed data where the fine fragments region of these FSDs are fitted with regression line  $\ln(C_1) + \alpha \times \ln(s) - s/s_f$ . The average value for the exponents, for  $p_0 \geq -0.05$ , in total six levels of external stresses, is  $-1.707 \pm 0.0490$ . A critical compressive external stress is reached at  $p_0 \approx -0.1$ , at which crushing becomes dominant over tensile fracture.

Since, the power-law range for the fines in Fig. 5(a)

is extremely short, and the exponential cut-off begin to influence the exponent value, we also tested fitting the exponent using weights  $1/\sqrt{\ln(s)}$  in the fitting algorithm. Then the average value of  $-\alpha$  for  $p_0 \geq -0.05$  become, e.g.  $-1.688 \pm 0.053$ , which is even closer to  $-5/3$ .

The reason the power-law range for the fines is so small in the simulations compared to the experiments is that the smallest possible fragment in the simulations is a single grain. In the experiments fragments get several orders of magnitude smaller. Notice, however, that  $s_f$  corresponds to fragments of linear size roughly in the range  $(4 - 20) \times x_{grain}$  for both experiments and simulations, indicating that it is indeed the grain size that determines the cross-over between fines and intermediate size fragments regions. Notice that,  $D_{particle} \sim x_{grain}$ .

Another discrepancy between experiments and simulations with the small cubes is the lack of the intermediate size range in the simulated FSDs. The reason for this seems to be that almost all fragments larger than the fines are boundary fragments which tend to have an exponential FSD [11].

In order to demonstrate both of the above, we computed FSDs for larger cubes and for different  $D_{particle}$ . The FSDs for a larger cube (6 mm $\times$ 6 mm $\times$ 6 mm) with the same particle size of  $x_{grain} = D_{particle} = 0.1$  mm at external stress level  $p_0 = +0.15$  is compared to its counterpart for the smaller cube in Fig. 5(c). Table V lists the result of a significance study for the two fitted lines of fines and intermediate size fragments for the larger cube. The conclusion is the same as for the experiments: The power exponent of the FSD for the fines and the intermediate-size fragments are the same, and there is an off-set between them.

**Table V:** Statistical significance study of the fine and intermediate size fragments' fitted lines for simulation of the large cube (6 mm $\times$ 6 mm $\times$ 6 mm) with  $D_{particle} = 0.1$  mm

Test	Fine-fragments region	Intermediate fragment size region
No. data points	3	10
R	-0.997	-0.980
p(R)	4.90E-2	7.16E-7
Residual variance	F = 15.047	p(F) = 0.197
Gradient	F = 0.009	p(F) = 0.928
Intercept	F = 21.961	p(F) = 8.500E-4

Figure 5(d) shows FSDs for the larger cube (6 mm $\times$ 6 mm $\times$ 6 mm) with the four different particle sizes of 0.2

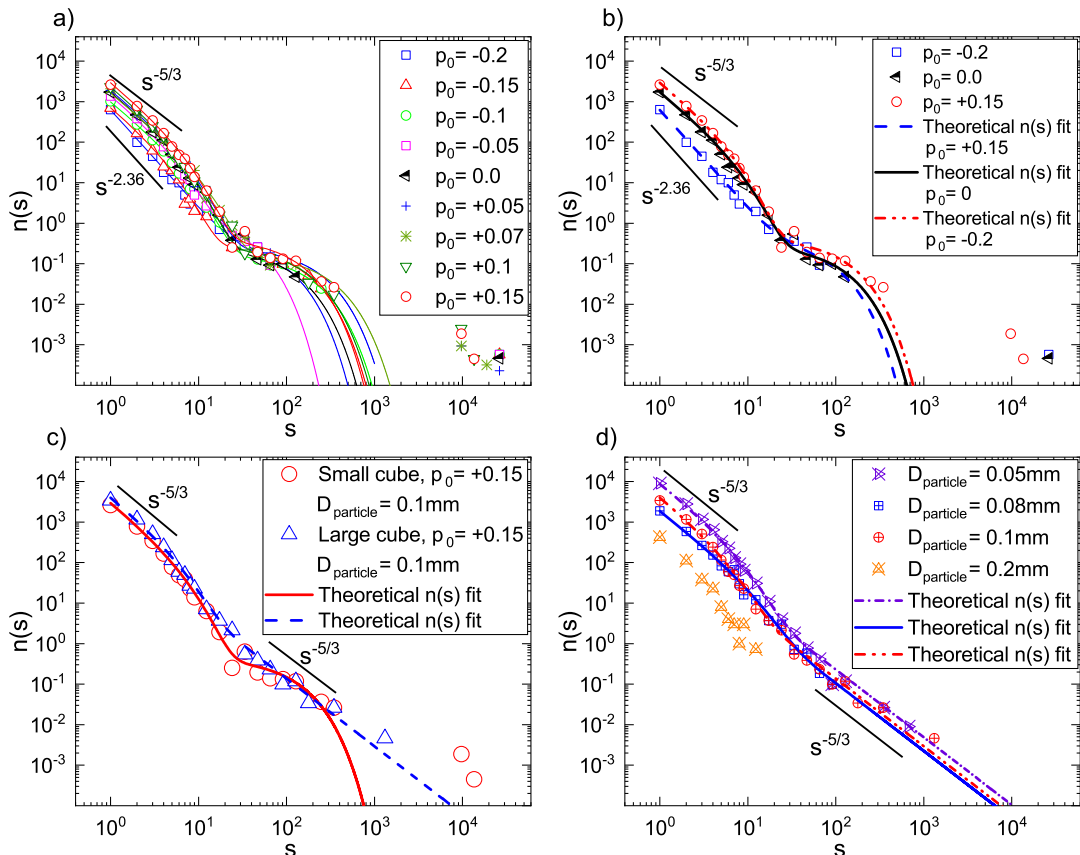


**Figure 5:** a) FSDs for dynamic crack propagation in the small cubes ( $3 \text{ mm} \times 3 \text{ mm} \times 3 \text{ mm}$ ) for the nine different external stress levels and their  $n(s)$  fits shown by the lines with the same color as the symbols. b) FSDs for the unstressed and the two extreme external stress conditions with  $p_0 = +0.15$  and  $p_0 = -0.2$ . Two lines with slopes of  $-2.36$  and  $-5/3$  are shown for comparison. c) FSD for the large cube ( $6 \text{ mm} \times 6 \text{ mm} \times 6 \text{ mm}$ ) with particle size  $0.1 \text{ mm}$  at  $p_0 = +0.15$  compared with that of the small cube at the same external stress condition. d) FSDs for the large cube with four different particle sizes  $0.2 \text{ mm}$ ,  $0.1 \text{ mm}$ ,  $0.08 \text{ mm}$  and  $0.05 \text{ mm}$  at  $p_0 = +0.15$ . The corresponding theoretical  $n(s)$  fits are shown by lines. Lines with slopes of  $-5/3$  are shown for comparison.

mm,  $0.1 \text{ mm}$ ,  $0.08 \text{ mm}$  and  $0.05 \text{ mm}$ . The fine fragment regions of the four simulations extend to roughly the same  $s_f \sim 10$ . Notice that this means a 64 times smaller fragment volume for the smallest particles compared to the largest. This demonstrates that the fragment *volume* at the cross-over between fines and intermediate size scales as the grain size  $D_{particle}^3$ .

## V. SUMMARY AND CONCLUSION

Here we report 28 experimental FSDs, where 4 are confined with pre-stressed aggregate and the rest are either unconfined or confined using a momentum trap. The fine fragments for 6 of them are sieved, apart from the standard mechanical sieving, with the sedimentation method down to  $0.002 \text{ mm}$ . For an additional 7 of them the fine fragments are estimated with laser diffraction with a resolution down to  $0.4 \mu\text{m}$ . These experimental FSDs, except the 4 that are confined with pre-stressed aggregate,

have two fragment-size regions in which branching and merging of cracks generate a FSD of the universal scale-invariant form. These are the fine and the intermediate-size fragments regions. Both can be described with a power-law exponent close to  $-5/3$  with a statistically significant off-set between them. If the blasted material is under compression induced by the pre-stressed confinement, the fine fragments are described by a steeper power-law.

Numerical simulations of the same effect can be achieved using a detailed model of a pressurized crack propagating within a cube with randomly packed spherical elements and a midplane crack. Again, the FSD has two regions with an approximate exponent of  $-5/3$ , unless the crack is under strong enough external compressive stresses, in which case the fines region has a steeper power-law.

In both cases, the conclusions are supported by a statistical significance analysis. By varying the resolution in the numerical model, i.e. reducing the particle size, it is shown that the cross-over between the two regions scales

as the average grain size.

Within mining it is common that operations require both blasting and ensuing crushing-grinding. The latter may well be the major contributor to the fines generation [4]. If the blast fragmentation is made coarser to reduce fines production by lowering the charge concentration, the need for increased crushing-grinding may quite possibly results in more total fine material from the operation. This makes the optimization of the process very challenging.

### Acknowledgments

This work has been funded by Austrian Science Fund (FWF): project P27594-N29. We thank Prof. Thomas Antretter (Montanuniversität Leoben) for his valuable support.

### Appendix A: EXPERIMENTAL MPFS

The transformation from experimental  $x - MPF(x)$  data to  $s$ - $n(s)$  data uses the derivative of Eq. (3). Let  $x_{min}$  denotes the smallest mesh then with  $s = (x/x_{min})^3$ :

$$n(s) = C \frac{MPF'(x)}{s ds/dx} = C \frac{x_{min}^3 MPF'(x)}{3x^2 s(x)}, \quad (A1)$$

with the prefactor  $C = \frac{M_0 x_{min}^3}{3m_{grain}}$ . The value of the prefactor in Eq. (A1) shifts the curve along the y-axis in  $\log(s)$ - $\log(n(s))$  space but does not change its shape. In our calculations the prefactor  $C = 1$  was used. The difference quotient for two successive mesh sizes  $x(i+1)$  and  $x(i)$  is used to calculate:

$$MPF'(x(j)) \cong \frac{MPF(x(i+1)) - MPF(x(i))}{x(i+1) - x(i)}, \quad (A2)$$

at  $x(j) = \sqrt{(x(i+1)x(i))}$ , the geometric mean (mid) points of all bins except the first,  $j = 2, \dots, n-1$ . Two points are added to this shifted data set;  $x(j=1) = x_{min}/2$  and  $x(j=0) = 0$  for which  $MPF(0) = 0$ . The equations  $s(j) = (x(j)/x_{min})^3$  define the corresponding  $s$ -values and Eqs. (A1, A2) the corresponding  $n(s(j))$  values.



- 
- [1] J. S. Rinehart, *Stress transients in solids*, (HyperDynamicS, New Mexico, 1975).
- [2] D. Thornton, S. S. Kanchibotla, and I. Brunton, in *Proceedings of Explo 2001 Conference, 2001*, edited by A. Marton, (AusIMM, Carlton, 2001), p. 197.
- [3] N. Djordjevic, in *Proceedings of 6th International Symposium for Rock Fragmentation by Blasting, Johannesburg, 1999*, p. 213.
- [4] I. Onederra, S. Esen, and A. Jankovic, *Estimation of fines generated by blasting - applications for the mining and quarrying industries*, Mining Technology 113, 237 (2004).
- [5] A. Irvani, I. Kukolj, F. Ouchterlony, T. Antretter, and J. Åström, in *Proceedings of 12th International Symposium for Rock Fragmentation by Blasting, 2018*, edited by H. Schunnesson & D. Johansson, p. 597.
- [6] D. Johansson, Lic. thesis, Luleå University of Technology, 2008.
- [7] J. A. Åström, *Statistical models of brittle fragmentation*, Adv. Phys. 55, 247 (2006).
- [8] A. Irvani, J. A. Åström, and F. Ouchterlony, *Physical Origin of the Fine-Particle Problem in Blasting Fragmentation*, Phys. Rev. Applied 10, 034001 (2018).
- [9] A. Meibom, and I. Balslev, *Composite power laws in shock fragmentation*. Phys. Rev. Lett. 76, 2492 (1996).
- [10] F. Wittel, F. Kun, H. J. Herrmann, and B. H. Kröplin, *Fragmentation of Shells* Phys. Rev. Lett. 93, 035504 (2004).
- [11] P. Gergő, I. Varga, and F. Kun, *Emergence of energy dependence in the fragmentation of heterogeneous materials*, Phys. Rev. E 90, 062811 (2014).
- [12] E. Sharon and J. Fineberg, *Microbranching instability and the dynamic fracture of brittle materials*, Phys. Rev. B 54, 7128 (1996)
- [13] R. Mahmoodi Baram, H. J. Herrmann, and N. Rivier, *Space-Filling bearings in three dimensions*, Phys. Rev. Lett. 92, 044301 (2004).
- [14] J. A. Åström and J. Timonen, *Spontaneous formation of densely packed shear bands of rotating fragments*, The European Physical Journal E 35, 40 (2012).
- [15] P. Kekäläinen, J. A. Åström, and J. Timonen, *Solution for the fragmentation-size distribution in a crack-branching model of fragmentation*, Phys. Rev. E 76, 026112 (2007).
- [16] T. I. Riikilä, T. Tallinen, J. A. Åström, and J. Timonen, *A discrete-element model for viscoelastic deformation and fracture of glacial ice*, Comput. Phys. Commun. 195, 14 (2015).
- [17] D.E. Grady, and M.E. Kipp, *Geometric statistics and dynamic fragmentation*, Journal of Applied Physics, 58, 3, 1210 (1985).
- [18] P. Moser, N. Cheimanoff, R. Ortiz, and R. Hochholdinger, in *Proceedings of the EFEE 1st world conference of explosives and blasting technique, Rotterdam, 2000*, edited by R. Holmberg (A.A. Balkema, Rotterdam, 2000), p. 165.
- [19] B. A. Wills and J. Finch, *Wills' mineral processing technology: an introduction to the practical aspects of ore treatment and mineral recovery* (Butterworth-Heinemann, 2015).
- [20] H. C. Grimshaw, in *Proceedings of In Mechanical properties of non-metallic materials, 1958*, edited by W. H. Walton, (Butterworths, London, 1958), p. 380.
- [21] C. Sun, PhD thesis, The University of Utah, USA, 2013.
- [22] I. Kukolj, A. Irvani, F. Ouchterlony, C. Weiss, and J. Lubensky, in *Proceedings of 12th International Symposium for Rock Fragmentation by Blasting, Luleå, Sweden, 2018*, edited by H. Schunnesson & D. Johansson, p. 483.
- [23] T. J. Napier-Munn, *Statistical methods for mineral engineers-How to design experiments and analyze data* (Julius Kruttschnitt Mineral Research center, Queensland, Australia, 2014), Sec. 6.3.
- [24] <https://github.com/joeatodd/HiDEM>
- [25] H. P. Rossmannith and K. Uenishi, *On size and boundary effects in scaled model blasts spatial problems*, Int. J. for Blasting and Fragmentation, 9, 139 (2005).

The MPF data of the experiments given in Table-1 of this paper are presented in Appendix B. In Appendix C and D the corresponding regression data and the statistical significance analysis, except for data set E4, are respectively given.

This page intentionally left blank.

## 9 Discussion

Yi and Johansson [59] used the bonded particle method implemented in the LS-DYNA code to model the blasting of unconfined cylinders of mortar (140 mm  $\times$  280 mm) with a centralized blast-hole. The explosive loading in the blast-hole was modeled using the particle blast method which is also implemented in the LS-DYNA code. Four simulations were performed for different explosive strength values. They plotted  $x - \text{MPF}(x)$  curves and  $x_{50}$  and  $x_{\max}$  versus the specific charge. The simulation results were then compared to fragmentation data of experimental tests with similar boundary and loading conditions.

They produced  $x - \text{MPF}(x)$  curves whose  $x_{50}$  and  $x_{\max}$  values were close to the ones of the experiments. However, the general behavior of the  $x - \text{MPF}(x)$  curves were not conforming to the experimental MPF curves. They noted that: “*Although both results have similar  $x_{50}$  and  $x_{\max}$ , the curve for the experimental results is steeper than that for the numerical results. The fine fragments take a big proportion of total fragments in the numerical results compared to those in the experimental results*”.

Our HiDEM simulation of the cylindrical specimens produced  $x - \text{MPF}(x)$  curves which also were not completely conforming to the experimental ones. The mass fraction of the fine-fragments made up a too large portion of the total mass, just like reported by Yi and Johansson [59]. Unlike them we have transformed the data for our  $x - \text{MPF}(x)$  curves to the  $s - n(s)$  FSD representation to compare our HiDEM simulation results with the experiments. This has made it possible to more clearly indicate the role of the fines generating mechanism.

Michaux [2, 5] studied the blast-induced fine-fragmentation in a similar way to our study with a larger focus on experiments, see Sec. 1.2.1 above. His data plotting  $x - A(x)$  and  $x - N(x)$  produced piece-wise straight lines (poly-lines) in log-normal and log-log space. He postulated that the different slopes of these lines characterize different fragmentation processes and that the kinks connecting these lines define the size limits where the process of fragmentation changes.

Michaux [5] concluded from the poly-line character of his data that the fragmentation is not truly fractal. He also notes that: “*The generation of fine fragmentation characterization has two fragment size thresholds of note, 10 mm and 1 mm, and is self-similar in nature*” and that: “*It has been postulated that these different sub-populations are generated by different mechanisms, which manifest as different micro crack branching characteristics. It is further postulated that while fragmentation may*

*not be a true fractal, the individual mechanisms that create it may possibly be."*

The importance of this in relation to our work is that Michaux [2, 5] finds many branching-merging mechanisms that operate over fixed size ranges. We on the other hand have found that the power-law exponent in  $s - n(s)$  is either  $-5/3$ , which is expected of branching-merging or some higher absolute value that shows an increasing contribution of crushing-shearing. Using his logic we have come much closer to showing that there is a universal branching-merging mechanism operating during tensile crack growth. We arrived at our conclusions because we used the  $s - n(s)$  formulation to represent both the experimental data and the simulation results.

Through transformation of the experimental  $x - \text{MPF}(x)$  data into the  $s - n(s)$  space, we have found that the FSD consists of three regions. They are the fine-fragments, the intermediate size fragments and the boulders. The fine-fragments region and the intermediate size one are connected either by a kink or by a vertical offset. The former takes place when the power-law exponent of the size distribution for the fine-fragments is of the crushing-shearing type ( $\beta > \alpha$ ). The latter, however, occurs when both the regions are formed by the branching-merging type of fragmentation. The location of the kink or the offset is found to be different between different materials, and in the experiments it is located between 0.25 mm to 2 mm, see Table E.I in Appendix E below.

We also have CT-micrographs that show that a macroscopic crack in granite or mortar is associated with an irregular band of microscopic cracks, see Fig. 1.3(b) above. It, however, shows the influence of the granularity to form fine-fragments. We have also shown that by increasing the numerical model resolution in the HiDEM the location of the offset, independent of the particle size, is at  $s_f \sim 10$ . However, this means a smaller fragment volume for smaller particle sizes. In this figure, Fig. 1.3(b), this band of micro cracks does not look like the conceptual or simplified branching-merging model used to derive the universal exponent  $\alpha \approx 5/3$  [17], Fig. 1.3(a). However, apparently this model is a good description of what is happening at the micro-scale. It is not the final and full description, though, because e.g. the dynamics of crack formation is not included [95].

## 10 Summary and Conclusions

The objective of this thesis is to use numerical methods and simulations to gain insight into the role of branching-merging in blast fragmentation. The currently most common theories on the source of blast-induced fines presume crushing-shearing as the main mechanism generating the fines-particles and that the majority of the fines is produced at or around a blast-hole, see Sec. 1.3. Dynamic crack branching and merging at the tips of dynamically propagating cracks was suggested as another plausible source of fine-fragments.

For this reason, following a review on experimental research of blast induced fracture and fragmentation, the brittle fragmentation characteristics and prediction equations have been reviewed. The FSDs, i.e.  $s - n(s)$  numerical results of fragmented specimens taken from the literature or mathematically derived, have been found to have a power-law behavior with either a universal power-law exponent  $-5/3$  corresponding to branching and merging or a higher value for crushing-shearing.

Next, a review of the most commonly used numerical methods for simulating fracture and fragmentation of concrete and other rock-like materials subjected to high-pressure loads has been made. The continuum mechanics based method (FEM) coupled with a damage-plasticity constitutive material model and the discrete element based model code (HiDEM) have been found useful as simulation tools for blast induced brittle fracture and fragmentation. Afterwards, the theoretical backgrounds of the numerical tools, i.e. CDP constitutive theory and the HiDEM discrete element code, that were used in this study were provided.

A comparison has been made between the FE code (Abaqus/Explicit) with the CDP constitutive material model and the HiDEM code in which particles are connected using beams with elastic material behavior. At the beginning, they were tested for the resultant fracture pattern and fragmentation of mortar.

The simulation results of these numerical tools show that for three load levels the simplified 2D FE models give more realistic post-mortem end-face fracture patterns than HiDEM's ones, Fig. 3.4. However, the 3D HiDEM models are superior in producing the MPFs and the FSDs. The HiDEM models are numerically more stable, whereas the FE models each require model-unique calibration parameters and the calibration of a 3D FE model is more complicated and time consuming.

Next, using experimental FSDs and the HiDEM simulation results, an  $s - n(s)$  equation, Eq. 3.1 was developed. It implicitly describes the blast induced frag-

mentation mechanisms. The FSD equation consists of three terms describing: 1) the fine-fragments, 2) the intermediate size fragments each with their corresponding power-law exponent, and 3) the boulders. The results demonstrate that for a stiffly confined cylinder the largest amount of the fine-fragments is created by the crushing-shearing mechanism. The branching-merging of tensile cracks form intermediate size fragments independent of the character of the confinement. The major tensile cracks delineate the boulders, which may contain internal cracks, see Fig. 3.6.

The absolute mass of fine-fragments was calculated as a function of their distance to the blast-hole. The HiDEM simulation results, supported by the experimental results of Svahn [4] demonstrate that the largest amount of fine-fragments is not even in the weak mortar solely created at or around the blast-hole as the original CZM assumes. The mass of the fine-fragments around the blast-hole is in absolute terms smaller than the mass of the fine-fragments formed outside the crushed zone.

In Paper IV simulations for a small scale cube model with a pre-defined pressurized edge crack were performed where the propagating crack was subjected to different values of lateral external stresses, both compressive and tensile. At high compressive external lateral stress levels, the majority of the fine-fragments were formed by crushing-shearing. Whereas, when the external lateral stresses were tensile or mildly compressive, the fine-fragments were formed by branching and merging of the propagating tensile crack fronts.

The FSD results of the former external lateral stress condition were accurately reproduced by the blast test setups of the stiffly confined cylinders. The ones of the latter external lateral stress condition were in agreement with the experimental FSDs of cylinders, which were either unconfined or confined using the MT concept. Hence, the first term describing the fine-fragments in the  $s - n(s)$  equation, Eq. 3.1, was modified to account for the branching-merging mechanism of fine-fragments generation, Eq. 3.2.

In conclusion, it has been demonstrated that the blast-induced fine-fragments of a brittle material like rock or mortar are formed not only by crushing-shearing but also due to branching-merging at the tips of dynamically propagating cracks or some similar mechanism. The active fine-fragments generating mechanism depends on the external stress level surrounding the propagating crack. The further conclusions of this thesis can be summarized after each research task:

**Conclusion 1:** to create a three-dimensional numerical model that describes the behavior of quasi-brittle materials, i.e. concrete or rock-like materials, fracturing when subjected to a civil blast load

- a two-dimensional FEM analysis using Abaqus/Explicit with a CDP constitutive material model produces a reasonable post-mortem end-face fracture pattern,
- however, the CDP in FEM needed implementation of model-unique calibration parameters, i.e. linear and quadratic bulk viscosity, Rayleigh material damping coefficients, mass scaling, and element-by-element time step estimation, unfortunately these parameters are case specific,
- the three-dimensional DEM analysis using HiDEM produces MPFs and FSDs that are similar to the experimental results,
- the use of a dynamic deposition method is more suitable than the FCC lattice structure to build a geometrical model, because the FCC lattice favors both preferential crack growth and crushing-shearing,
- on the outer periphery the quiet boundary condition in FEM and the velocity damping in HiDEM made it possible to study a simplified fracture network for a cylindrical specimen consisting of through-going cracks that connect the crushed zone to the outer boundary or merge with the other surrounding cracks,
- the pressure-time explosive loading function used is not realistic, but it made it possible to obtain realistic simulation results, in the future the blast-hole loading will have to incorporate the volume expansion of the explosive gases [59],
- the post-peak amplitude in the pressure-time explosive loading function has to be calibrated to mimic the experimental results, as used in Fig. 3(b) of Paper II,
- the small scale HiDEM cubes with a pre-defined pressurized edge crack are useful when studying under which stress conditions the branching-merging mechanism switches to crushing-shearing;



**Conclusion 2:** to compute the FSDs of the numerical model subjected to civil blast load, especially for the fine-fragments

- in HiDEM, independent of the geometrical configuration, the FSDs are expressed using the  $s - n(s)$  representation with the parameter  $s$  being the number of particles forming a fragment and the  $n(s)$  being the number of fragments each containing  $s$  particles,
- the computed FSDs consist of three distinct regions representing fine-fragments, intermediate size fragments, and boulders,
- the fine and intermediate size fragments are connected by either a kink or an offset,
- in the HiDEM simulations the former occurs when high compressive confinement stresses surround the propagating cracks and the latter occurs when the confinement is tensile or at low compressive levels,
- the location of the kink or the offset connecting the fine-fragments region and the intermediate size region is governed by the granularity of the material which is roughly in the range of  $s_f \sim 4 - 20$ ,
- the computed MPF of a blast cylinder is obtained from: a fragment is defined by the number of connected rigid particles  $s$  it contains and the mesh size (screen size) of the fragment is defined by the diameter of the volume equivalent sphere;

**Conclusion 3:** to compare the computed FSDs with the results from the experiments carried out as a part of the FWF project [3] and from the literature

- the transformation of the  $x - \text{MPF}(x)$  data to  $s - n(s)$  i.e. FSD data is made,
- we have compared our numerical FSDs with experimental data sets from Johansson [27], Grimshaw [92], and from our own tests [3], i.e., in total for 32 data sets, where a good agreement was found between the experimental and the numerical results,
- we have compared the absolute mass of fine-fragments as a function of their distance to the blast-hole with the results from Svahn [4]. The results were contrary to the classical CZM which presumes that the fine-fragments are almost solely formed around the blast-hole,
- our blast cylinder tests with no or weak mantle confinement generate fines fragments created by a branching-merging type of fragmentation, when the confinement increases, more and more opposing the radial expansion of the cylinder, the crushing-shearing mechanism takes over,
- numerical simulations of a pressurized crack subjected to external lateral stresses show the same effect, when the external lateral stresses become compressive the crushing-shearing mechanism forms the fine-fragments, when the external lateral stresses become more tensile the branching-merging mechanism forms the fine-fragments,
- in the cube model, an effect of a rigid boundary condition of the blast cylinder tests is studied by adding a compressive stress wave that is moving against the propagation direction of the pressurized crack corresponding to a returning compressive stress wave. It widens the crack path and induces more crushing fines when the external lateral stresses are compressive and are at a level to hold two crack flanks together,
- the returning compressive stress wave may also cause the propagating crack tip to branch due to shearing,
- an effect of a lower impedance boundary condition of the blast cylinder tests is studied by adding a returning tensile stress wave. In the cube model, the returning tensile wave induces branching of the propagating pressurized crack,

**Conclusion 4:** to provide a scientific explanation of how these fine-fragments are generated

- fragments formed by different mechanisms produce different power-law exponents in  $s - n(s)$  space, branching-merging gives the universal power-law exponent of  $-5/3$  and crushing produces a higher absolute value,
- the three terms of the FSD  $s - n(s)$  equation of the stiffly confined cylinders indicate that the fine-fragments were formed by crushing, intermediate size fragments by branching-merging, and the boulders are delineated by major tensile cracks,
- the FSDs of the blast cylinders that are unconfined or confined by MT are different from the FSDs of the stiffly confined blast cylinders in that not only are the intermediate-size fragments created by branching-merging type of fragmentation but the fines-region ones are too.

## 11 Outlook

This thesis performs a numerical analysis of blast induced fracture and fragmentation. To achieve meaningful results, a number of simplifications have been made in the constitutive material model, in the internal boundary conditions, i.e. the explosive pressure load in the blast-hole and in the outer boundary conditions. Despite these simplifications, reasonably realistic FSDs have been obtained. To obtain a better quantitative agreement, the following aspects will have to be considered:

- DEM models will become more realistic with the implementation of a more sophisticated constitutive material model. Such a model should use two different strength values corresponding to the tensile and compressive strengths. Moreover, it would also be useful to implement plastic hardening, softening (see Sec. 2.1) and rate dependency [96, 97, 98].
- The pressure applied on the blast-hole wall has so far been a function of time,  $p(t)$ . Pressure as a function of specific volume,  $p(v)$  is more realistic.
- Once the new models work well for the type of cylinder tests made so far, a further step would be to model high resolution lab-scale size cylinders or full scale geometries.
- Other types of cementitious or rock-like materials subjected to civil blast load should be analyzed.
- Boundary conditions play an important role in the results of the fragmentation, see Table-IV and also Fig. 5(a) and (b) in Paper IV. Therefore, it would be useful to study different boundary conditions in high resolution lab-scale size cylinders to understand in greater detail when and under which circumstances the crushing mechanism for creating fine-fragments will dominate over the branching-merging mechanism, and vice versa.
- The MPF of the HiDEM simulation results were obtained such that the screen size of a fragment is the diameter of the volume equivalent sphere, however, calculating the major lengths of a fragment would provide the researcher with the fragment's shapes and a more accurately calculated MPF.

This page intentionally left blank.

# List of Figures

Figure 1.1 –Average mass passing distribution curves for three blasted cylinders of Svahn [4], comparing black core with the sum of the two outer layers. $\varnothing_{\text{outer}} = 120 \text{ mm}$ , $200 \text{ mm}$ and $300 \text{ mm}$ for black, yellow and green. The figure is taken from [8]. The inset of the figure illustrates the multilayered setup of the blasted cylinders. . . . .	3
Figure 1.2 –Michaux [2] plots of $x - A(x)$ and $x - N(x)$ . a) The plot of $x - A(x)$ in a log-normal scale, the fragments sub-population of monzonite has three regions with different gradients. The thresholds are indicated with $\theta \sim 100 \mu\text{m}$ and $\phi \sim 1 \text{ mm}$ . b) The plot of $x - N(x)$ in a log-log scale, the grout data set has three regions with different gradients. The size ranges are fixed and are indicated in the figure. . . . .	5
Figure 1.3 –a) Schematic representation of a 2D crack branching and merging fragments formation on both sides of a propagating crack. Thick line in the middle is the main crack and the thin lines are side branches [15]. b) A branching and merging mechanism and the resultant fragmentation in granite blasted with $20 \text{ g/m}$ of PETN. The figure is taken by scanning electron microscope [3]. . . . .	7
Figure 1.4 –Failure mechanisms due to a) tension, b) bending, c) shearing, and d) compression, particles come into contact experiencing repulsive force. . . . .	10
Figure 1.5 –Schematic view of a) CZM [24], b) star shape model [76]. Figures are taken from [77] . . . . .	12
Figure 1.6 –The relationships between research tasks (RT) and the appended papers . . . . .	14
Figure 1.7 –The relationships between the contents of the appended papers . . . . .	15

Figure 2.1 –a) Compressive stress-strain loading-unloading curves for a concrete cylinder with high-intensity repeated compressive loading, the figure is taken from [78]; b) Tensile stress-strain curve in a post-peak cyclic test, the figure is taken from [79]; Schematic representation of the loading-unloading behavior in c) an elastic-damage constitutive model, d) an elastic-plastic constitutive model, and e) an elastic-plastic damage constitutive model. . . . .	17
Figure 2.2 –Influence of the $w_c$ weight factor which controls the recovery of the tensile and compressive stiffness upon load reversal. Figure is taken from [1]. . . . .	20
Figure 2.3 –Shape of yield function in the deviatoric plane with different values of $K_c$ . Figure is taken from [1]. . . . .	21
Figure 3.1 –a) Top view of the FE model discretized using the C3D8R stress elements and a quiet boundary condition formed using the 3D infinite elements (CIN3D8) b) Pressure-time explosive loading history with three peak pressures of 35 MPa, 85 MPa, and 166 MPa used in the FE models. . . . .	25
Figure 3.2 –The fracture patterns developed a) with the application of the quiet boundary condition, b) free boundary condition. . . . .	26
Figure 3.3 –Propagation of a shock wave through a one-dimensional mesh [1] .	27
Figure 3.4 –Experimental end-face fracture patterns of blasted mortar cylinders [3, 85] with PETN cords of a) 6 g/m, b) 12 g/m, and c) 20 g/m. The FE simulation results of the 2D disks blasted with the explosive load levels equivalent to e) 6 g/m of PETN, e) 12 g/m of PETN and f) 20 g/m of PETN. The deleted elements in the simulation results of Figs. (d)-(f) are shown in white. . . . .	28
Figure 3.5 –a) The HiDEM cylinder used in Paper II which is blasted with the explosive load level equivalent to 6 g/m of PETN, particles are arranged in a FCC lattice structure. b) The so-called stiff test set-up with a layer of pre-stressed aggregate around the outer periphery of the cylinder as the confining condition [90]. The pre-stressed level is determined by the torque used to tighten the bolts. . . . .	29
Figure 3.6 –Fragment size distribution in $s-n(s)$ space. Triangular data points represent the experimental data [27]. The data are fitted in log-log space using Eq. 3.1 and represented by the dashed line. The three regions of the FSD are marked. . . . .	29

- Figure 3.7 –End-face fracture pattern of the HiDEM cylinder which is generated using the dynamic deposition algorithm. . . . . 31
- Figure 3.8 –a) HiDEM simulation results, absolute mass of fine-fragments, i.e. fragments formed by one DEM particle, at three concentric cylinders with outer radii of  $r_{\text{outer}} = 30$  mm, 50 mm, and 70 mm. Three cylinders blasted at three explosive load levels of 35 MPa, 85 MPa and 166 MPa equivalent to 6 g/m, 12 g/m and 20 g/m of PETN cord, b) Svahn [4] experimental data of the fine fragments smaller than 2 mm at three concentric layers of black  $r_{\text{outer}} < 60$  mm, yellow  $r_{\text{outer}} < 100$  mm and green  $r_{\text{outer}} < 150$  mm for three blasted cylinders with 40 g/m of PETN. . . . . 32
- Figure 3.9 –Triangular data points represent the experimental data in  $s - n(s)$  form. In this experiment (E1: 20 g/m), the cylinder is confined by MT [3]. The data are fitted in log-log space using Eq. 3.2 and represented by the dashed line. The three regions of the FSD are marked. The inset shows the offset connecting the fine-fragments region to intermediate size one. The two extended dashed lines shown in the inset are for better illustration of the offset. . . . . 33
- Figure 3.10 –2D schematic representation of the cube and the defined boundary conditions. . . . . 35
- Figure 3.11 –The FSDs of the dynamic crack propagation in the cube with a returning compressive stress wave a) for  $P_{\text{conf}} = -0.2 P_{\text{app}}$  and b) for  $P_{\text{conf}} = +0.15 P_{\text{app}}$ ; and for comparison, that of the cube at the same boundary conditions without the returning compressive stress wave in blue. The corresponding theoretical  $n(s)$  fits are shown by lines with the same color as the symbols. The lines with slope  $-5/3$ ,  $-2.5$  and  $-2.35$  are shown for comparison. The final fracture patterns for  $P_{\text{conf}} = -0.1 P_{\text{app}}$  in c) without the returning compressive stress wave and in d) the same with the returning compressive stress wave. The cube’s particles are shown with white points for visibility of fragmentation. Red: single particle fragments, blue: fragments containing two particles, green: fragments containing 3 to 10 particles, pink: fragments containing 11 to 100 particles. . . . . 36
- Figure 3.12 –The final fracture patterns for  $P_{\text{conf}} = +0.05 P_{\text{app}}$  in a) the cube without the returning tensile stress wave and in d) the same cube but with the returning tensile stress wave. Red: single particle fragments, blue: fragments containing two particles, green: fragments containing 3 to 10 particles. . . . . 37



This page intentionally left blank.

## 12 Appendices

### Appendix A: Abaqus/Explicit VUSDFLD

```
C -----
C Element deletion using PEEQT values
C -----

      subroutine vusdfld(
c Read only -
      *   nblock, nstatev, nfieldv, nprops, ndir, nshr,
      *   jElem, kIntPt, kLayer, kSecPt,
      *   stepTime, totalTime, dt, cmname,
      *   coordMp, direct, T, charLength, props,
      *   stateOld,
c Write only -
      *   stateNew, field )

      include 'vaba_param.inc'

      dimension jElem(nblock), coordMp(nblock,*),
      *         direct(nblock,3,3), T(nblock,3,3),
      *         charLength(nblock), props(nprops),
      *         stateOld(nblock,nstatev),
      *         stateNew(nblock,nstatev),
      *         field(nblock,nfieldv)
      character*80 cmname

      parameter( nrData=6 )
      PARAMETER( ZERO = 0.D0, ONE = 1.D0, TWO = 2.D0,
      * THREE = 3.D0, THIRD = ONE/THREE, HALF = .5D0,
      * TWOTHIRDS = TWO/THREE, THREEHALFS = 1.5D0 )

      character*3 cData(maxblk*nrData)
      dimension rData(maxblk*nrData), jData(maxblk*nrData)
c Define maximum PEEQT:
      FS = 0.0011

      jStatus = 1
```

```

call vgetvrm( 'PEEQT', rData, jData, cData, jStatus )

if( jStatus .ne. 0 ) then
    call xplb_abqerr(-2,'Utility_routine_VGETVRM_ '//
*       'failed_to_get_variable.',0,zero,' ')
    call xplb_exit
end if

call setField(nblock, nstatev, nfieldv, nrData,
*   rData, stateOld, stateNew, field, FS)

return
end

```

```

C-----
subroutine setField( nblock, nstatev, nfieldv,
*   nrData, PEEQT, stateOld, stateNew, field, FS)

include 'vaba_param.inc'

dimension stateOld(nblock,nstatev),
*   stateNew(nblock,nstatev),
*   field(nblock,nfieldv), PEEQT(nblock,nrData)
PARAMETER( ZERO = 0.D0, ONE = 1.D0, TWO = 2.D0,
*   THREE = 3.D0, THIRD = ONE/THREE, HALF = .5D0,
*   TWOTHIRDS = TWO/THREE, THREEHALFS = 1.5D0 )

do k = 1, nblock
field(k,1)= PEEQT(k,1)
stateNew(k,1) = field(k,1)
c   Failure criterion
if(StateNew(k,1) .gt. FS) then
StateNew(k,2) = 0.0
endif
enddo
return
end

```

```

C-----
C VUAMP: introducing pressure function profile
C-----

```

```

C   Pressure Function taken from Trivino & Mohanty
C   "Seismic radiation patterns from cylindrical
C   explosive charges by Analytical and combined FDEM"
C-----
      SUBROUTINE VUAMP(
*       ampName, time, ampValueOld, dt, nprops,
*       props, nSvars, svars, lFlagsInfo, nSensor,
*       sensorValues, sensorNames, jSensorLookUpTable,
*       AmpValueNew,
*       lFlagsDefine,
*       AmpDerivative, AmpSecDerivative, AmpIncIntegral)

      INCLUDE 'VABA_PARAM.INC'

C       time indices
      parameter (iStepTime      = 1,
*              iTotTime        = 2,
*              nTime           = 2)

C       flags passed in for information
      parameter (iInitialization = 1,
*              iRegularInc      = 2,
*              ikStep           = 3,
*              nFlagsInfo       = 3)

C       optional flags to be defined
      parameter (iComputeDeriv   = 1,
*              iComputeSecDeriv = 2,
*              iComputeInteg    = 3,
*              iStopAnalysis    = 4,
*              iConcludeStep    = 5,
*              nFlagsDefine     = 5)
      dimension time(nTime), lFlagsInfo(nFlagsInfo),
*              lFlagsDefine(nFlagsDefine),
*              sensorValues(nSensor),
*              props(nprops),
*              sVars(nSvars)

c       Choose parameters M_u and M_d
c       Rise Time 7.85 microsecond:
c           parameter( mu = 5e5, md = 20e3)

```

```

c      Rise Time 1 microsecond:
c
parameter( mu = 45e5, md = 15e3)

parameter( mu = 45e5, md = 25e3)
parameter( m_ratio = mu/md , b_ratio = 2)
parameter( alpha1 = 10e-7, alpha2 = 10e-3)

character*80 ampName

      if (ampName(1:7) .eq. 'USERAMP' ) then

          if (lFlagsInfo(iInitialization) .eq. 1) then
              ampValueNew = ampValueOld
          else
              ttim = time(iStepTime)
              bd = (sqrt(real(2))/2) * exp(0.5) * md
              bu = bd / b_ratio
              nn = (sqrt(real(2))/2) * exp(0.5) * b_ratio
*              * m_ratio
              n = ANINT(real(nn))
              tu = ((-log(alpha1)) ** (0.5/n))/bu
              td = (((-log(alpha1)) ** (0.5/n)) -
*              ((-log(1 - alpha2)) ** (0.5/n)))/bu
              Pu = exp(-(bu * (ttim - tu)) ** (2 * n))
              Pd = exp(-(bd * (ttim - td)) ** (2) )
              P = Pu * Pd
              ampValueNew = P
          endif
      endif

return
end

```

**Appendix B: Experimental MPFs**

Tables B.I to B.VI list the experimental MPF data of the experiments given in Table-I of Paper IV given in Chapter 8.

Table B.1: Experimental MPFs of E1 and E2

E1: 6 g/m		E1: 12 g/m		E1: 20 g/m		E2: 6 g/m		E2: 12 g/m		E2: 20 g/m	
Mesh size [mm]	MPF [%]	Mesh size [mm]	MPF [%]	Mesh size [mm]	MPF [%]	Mesh size [mm]	MPF [%]	Mesh size [mm]	MPF [%]	Mesh size [mm]	MPF [%]
125	58.34	125	100	125	100	125	100	125	100	125	95.54
100	58.34	100	73.68	100	100	100	75.56	100	75.56	100	95.54
80	44.20	80	73.68	80	71.55	80	18.57	80	18.57	80	55.80
63	10.01	63	28.02	63	27.56	63	6.40	63	47.03	63	39.97
50	8.10	50	12.78	50	10.05	50	3.09	50	22.72	50	28.95
40	4.88	40	8.12	40	8.98	40	1.78	40	9.97	40	23.46
31.5	3.57	31.5	5.87	31.5	5.14	31.5	1.48	31.5	7.99	31.5	18.21
25	1.77	25	4.75	25	2.79	25	1.163	25	6.89	25	13.95
20	1.48	20	3.20	20	2.40	20	0.978	20	5.71	20	10.87
18	1.44	18	3.03	18	1.89	18	0.919	18	5.22	18	10.01
16	1.20	16	2.46	16	1.87	16	0.888	16	4.81	16	9.33
14	1.08	14	2.14	14	1.56	14	0.769	14	4.48	14	8.57
12.5	0.979	12.5	1.95	12.5	1.36	12.5	0.672	12.5	4.04	12.5	7.80
10	0.776	10	1.70	10	1.22	10	0.549	10	3.37	10	6.58
8	0.613	8	1.47	8	1.07	8	0.443	8	2.79	8	5.59
6.3	0.532	6.3	1.32	6.3	0.930	6.3	0.304	6.3	2.38	6.3	4.95
5	0.433	5	1.14	5	0.804	5	0.264	5	1.99	5	4.23
4	0.362	4	1.03	4	0.714	4	0.228	4	1.69	4	3.63
3.15	0.320	3.15	0.936	3.15	0.583	3.15	0.202	3.15	1.46	3.15	3.19
2	0.252	2	0.804	2	0.440	2	0.160	2	1.12	2	2.45
1	0.187	1	0.656	1	0.328	1	0.117	1	0.775	1	1.67
0.5	0.139	0.5	0.336	0.5	0.194	0.5	0.0769	0.5	0.470	0.5	1.01
0.25	0.0797	0.25	0.196	0.25	0.0541	0.25	0.0433	0.25	0.244	0.25	0.540
0.1	0.0216	0.1	0.0584	0.1	0.0149	0.1	0.0172	0.1	0.086	0.1	0.198
0.04	0.00564	0.04	0.0179	0.04	0.00320	0.04	0.00320	0.04	0.0223	0.04	0.0637

Table B.II: Experimental MPFs of E3 [27]

3 g/m			5 g/m			10 g/m			20 g/m			40 g/m			
Mesh size [mm]	MPF [%]	Mesh size [mm]	MPF [%]	Mesh size [mm]	MPF [%]	Mesh size [mm]	MPF [%]	Mesh size [mm]	MPF [%]	Mesh size [mm]	MPF [%]	Mesh size [mm]	MPF [%]	Mesh size [mm]	MPF [%]
125	100.00	125	100.00	125	100.00	125	100.00	125	100.00	125	100.00	125	100.00	125	100.00
90	100.00	90	100.00	90	100.00	90	100.00	90	100.00	90	100.00	90	100.00	90	100.00
63	38.94	63	86.62	63	100.00	63	100.00	63	100.00	63	100.00	63	100.00	63	100.00
45	14.71	45	29.05	45	85.72	45	85.72	45	98.91	45	98.91	45	100.00	45	100.00
31.5	7.02	31.5	15.27	31.5	65.51	31.5	65.51	31.5	84.99	31.5	84.99	31.5	99.61	31.5	99.61
22.4	4.64	22.4	10.14	22.4	42.03	22.4	42.03	22.4	64.16	22.4	64.16	22.4	87.49	22.4	87.49
16	3.35	16	6.89	16	27.55	16	27.55	16	48.84	16	48.84	16	71.99	16	71.99
11.2	2.16	11.2	4.86	11.2	18.20	11.2	18.20	11.2	36.06	11.2	36.06	11.2	59.92	11.2	59.92
8	1.59	8	3.44	8	12.84	8	12.84	8	25.63	8	25.63	8	49.80	8	49.80
5.6	1.19	5.6	2.51	5.6	8.70	5.6	8.70	5.6	18.19	5.6	18.19	5.6	40.12	5.6	40.12
4	0.923	4	1.87	4	6.12	4	6.12	4	13.42	4	13.42	4	32.71	4	32.71
2	0.630	2	1.20	2	3.70	2	3.70	2	8.25	2	8.25	2	22.24	2	22.24
1	0.465	1	0.846	1	2.49	1	2.49	1	5.49	1	5.49	1	15.66	1	15.66
0.5	0.367	0.5	0.636	0.5	1.87	0.5	1.87	0.5	4.071	0.5	4.071	0.5	11.83	0.5	11.83
0.25	0.267	0.25	0.455	0.25	1.33	0.25	1.33	0.25	2.81	0.25	2.81	0.25	7.94	0.25	7.94
0.125	0.160	0.125	0.244	0.125	0.693	0.125	0.693	0.125	1.34	0.125	1.34	0.125	3.35	0.125	3.35
0.063	0.0854	0.063	0.127	0.063	0.388	0.063	0.388	0.063	0.684	0.063	0.684	0.063	1.63	0.063	1.63



Table B.III: Experimental MPFs of E4 [27]

5 g/m		10 g/m		20 g/m		40 g/m	
Mesh size [mm]	MPF [%]	Mesh size [mm]	MPF [%]	Mesh size [mm]	MPF [%]	Mesh size [mm]	MPF [%]
125	100.00	125	100.00	125	100.00	125	100.00
90	100.00	90	100.00	90	100.00	90	100.00
63	21.87	63	53.26	63	97.00	63	100.00
45	6.50	45	23.49	45	61.88	45	97.13
31.5	4.49	31.5	11.13	31.5	38.74	31.5	85.93
22.4	2.77	22.4	8.13	22.4	24.84	22.4	65.12
16	2.15	16	5.04	16	15.07	16	44.26
11.2	1.91	11.2	4.46	11.2	10.68	11.2	28.65
8	1.71	8	3.67	8	7.82	8	21.93
5.6	1.56	5.6	3.08	5.6	6.12	5.6	16.76
4	1.45	4	2.67	4	4.88	4	12.98
2	1.27	2	2.20	2	3.53	2	8.63
1	1.15	1	1.89	1	2.80	1	6.40
0.5	1.05	0.5	1.72	0.5	2.34	0.5	5.19
0.25	0.982	0.25	1.58	0.25	2.02	0.25	4.27
0.125	0.849	0.125	1.42	0.125	1.76	0.125	3.41
0.063	0.787	0.063	1.26	0.063	1.39	0.063	2.86

Table B.IV: Experimental MPFs of E5 [92]

0.46 kg/m <sup>3</sup>		0.44 kg/m <sup>3</sup>		0.431 kg/m <sup>3</sup>		0.231 kg/m <sup>3</sup>		0.218 kg/m <sup>3</sup>		0.22 kg/m <sup>3</sup>	
Mesh size [mm]	MPF [%]	Mesh size [mm]	MPF [%]	Mesh size [mm]	MPF [%]	Mesh size [mm]	MPF [%]	Mesh size [mm]	MPF [%]	Mesh size [mm]	MPF [%]
406.4	100.00	406.4	100.00	406.40	100.00	406.4	100.00	406.4	100.00	406.4	100.00
203.2	76.11	203.2	77.72	203.2	76.19	203.2	60.55	203.2	59.68	203.2	76.77
101.6	57.51	101.6	48.50	101.6	59.06	101.6	35.43	101.6	37.94	101.6	31.02
50.8	39.29	50.8	31.12	50.8	39.62	50.8	19.30	50.8	19.75	50.8	16.73
25.4	26.05	25.4	24.21	25.4	24.98	25.4	8.77	25.4	7.93	25.4	8.10
12.7	17.52	12.7	20.39	12.7	15.93	12.7	5.97	12.7	4.93	12.7	4.35
6.35	12.90	6.35	10.15	6.35	12.19	6.35	4.23	6.35	3.40	6.35	3.02
1.5875	7.79	1.5875	6.15	1.5875	7.74	1.5875	2.77	1.5875	2.15	1.5875	1.95
0.5	6.40	0.5	5.52	0.5	6.20	0.5	2.12	0.5	1.58	0.5	1.424
0.251	3.94	0.251	3.51	0.251	3.42	0.251	1.19	0.251	0.981	0.251	0.839
0.124	1.51	0.124	1.26	0.124	1.19	0.124	0.429	0.124	0.364	0.124	0.270
0.066	0.670	0.066	0.583	0.066	0.491	0.066	0.192	0.066	0.169	0.066	0.115
0.02	0.228	0.02	0.232	0.02	0.199	0.02	0.0823	0.02	0.066	0.02	0.0401
0.01	0.145	0.01	0.142	0.01	0.131	0.01	0.0514	0.01	0.0399	0.01	0.0222
0.005	0.0790	0.005	0.0754	0.005	0.0663	0.005	0.0234	0.005	0.0197	0.005	0.0131
0.002	0.0283	0.002	0.0289	0.002	0.0167	0.002	0.00580	0.002	0.00710	0.002	0.00470

Table B.V: Experimental MPFs of E6 [3]

6 g/m		12 g/m		20 g/m	
Mesh size [mm]	MPF [%]	Mesh size [mm]	MPF [%]	Mesh size [mm]	MPF [%]
125	58.34	125	100.00	100	100.00
100	58.34	100	73.68	80	93.51
80	44.20	80	73.68	63	54.77
63	10.01	63	28.02	50	22.32
50	8.10	50	12.78	40	15.83
40	4.88	40	8.12	31.5	8.67
31.5	3.57	31.5	5.87	25	7.36
25	1.77	25	4.75	20	4.63
20	1.48	20	3.20	18	4.12
18	1.44	18	3.03	16	3.50
16	1.20	16	2.46	14	3.32
14	1.08	14	2.14	12.5	2.95
12.5	0.979	12.5	1.95	10	2.35
10	0.776	10	1.70	8	2.01
8	0.613	8	1.47	6.3	1.74
6.3	0.532	6.3	1.32	5	1.46
5	0.433	5	1.14	4	1.25
4	0.362	4	1.028	3.15	1.12
3.15	0.320	3.15	0.936	2	0.914
2	0.252	2	0.804	1	0.693
1	0.186	1	0.656	0.5	0.445
0.5	0.118	0.5	0.293	0.25	0.310
0.25	0.0817	0.25	0.196	0.1	0.0674
0.1	0.0158	0.1	0.0440	0.04	0.0189
0.04	0.00363	0.04	0.0135	0.032	0.0145
0.032	0.00261	0.032	0.0109	0.025	0.0109
0.025	0.00183	0.025	0.00856	0.02	0.00844
0.02	0.00133	0.02	0.00692	0.015	0.00624
0.015	0.000941	0.015	0.00536	0.0125	0.00518
0.0125	0.000756	0.0125	0.00456	0.01	0.00416
0.01	0.000577	0.01	0.00376	0.0071	0.00314
0.0071	0.000392	0.0071	0.00289	0.0063	0.00288
0.0063	0.000349	0.0063	0.00265	0.005	0.00247
0.005	0.000285	0.005	0.00229	0.004	0.00214
0.004	0.000231	0.004	0.00199	0.003	0.00175
0.003	0.000181	0.003	0.00164	0.002	0.00126
0.002	0.000137	0.002	0.00121	0.0016	0.00103
0.0016	0.000109	0.0016	0.00100	0.001	0.000542
0.001	0.0000564	0.001	0.000613	0.00071	0.000201
0.00071	0.0000214	0.00071	0.000369	0.00063	0.0000998
0.00063	0.0000119	0.00063	0.000299	0.0005	0.0000025
0.0005	0.0000006	0.0005	0.000233		
		0.0004	0.000230		

Table B.VI: Experimental MPFs of E7 [3]

6 g/m		(bl24) 12 g/m		(bl25) 12 g/m		20 g/m	
Mesh size [mm]	MPF [%]	Mesh size [mm]	MPF [%]	Mesh size [mm]	MPF [%]	Mesh size [mm]	MPF [%]
125	100.00	100	100.00	80	100.00	100	100.00
100	75.56	80	85.70	63	49.23	80	58.44
80	18.57	63	33.66	50	23.79	63	41.86
63	6.40	50	22.96	40	10.45	50	30.32
50	3.09	40	12.83	31.5	8.37	40	24.56
40	1.76	31.5	10.60	25	7.23	31.5	19.07
31.5	1.48	25	7.96	20	5.99	25	14.61
25	1.163	20	6.48	18	5.48	20	11.38
20	0.978	18	5.79	16	5.05	18	10.48
18	0.919	16	5.02	14	4.71	16	9.77
16	0.888	14	4.26	12.5	4.24	14	8.97
14	0.769	12.5	3.79	10	3.52	12.5	8.17
12.5	0.672	10	3.17	8	2.92	10	6.89
10	0.549	8	2.69	6.3	2.49	8	5.85
8	0.443	6.3	2.25	5	2.08	6.3	5.19
6.3	0.304	5	1.90	4	1.76	5	4.43
5	0.264	4	1.61	3.15	1.53	4	3.80
4	0.228	3.15	1.43	2	1.17	3.15	3.34
3.15	0.202	2	1.09	1	0.791	2	2.57
2	0.160	1	0.764	0.5	0.359	1	1.74
1	0.116	0.5	0.373	0.25	0.234	0.5	1.00
0.5	0.0586	0.25	0.244	0.1	0.0645	0.25	0.709
0.25	0.0403	0.1	0.0649	0.04	0.0181	0.1	0.362

Continued on Next Page...

Table B.VI – Continued

6 g/m		(b124) 12 g/m		(b125) 12 g/m		20 g/m	
Mesh size [mm]	MPF [%]	Mesh size [mm]	MPF [%]	Mesh size [mm]	MPF [%]	Mesh size [mm]	MPF [%]
0.1	0.01184	0.04	0.0173	0.032	0.0139	0.04	0.0777
0.04	0.00307	0.032	0.0132	0.025	0.0103	0.032	0.0610
0.032	0.00219	0.025	0.00974	0.02	0.00792	0.025	0.049
0.025	0.00153	0.02	0.00749	0.015	0.00611	0.02	0.0375
0.02	0.00113	0.015	0.00563	0.0125	0.00523	0.015	0.0297
0.015	0.000829	0.0125	0.00485	0.01	0.00436	0.0125	0.0226
0.0125	0.000699	0.01	0.00414	0.0071	0.00338	0.01	0.0195
0.01	0.000580	0.0071	0.00317	0.0063	0.00312	0.0071	0.0166
0.0071	0.000458	0.0063	0.00286	0.005	0.00267	0.0063	0.0131
0.0063	0.000425	0.005	0.00231	0.004	0.00228	0.005	0.0120
0.005	0.000371	0.004	0.00181	0.003	0.00181	0.004	0.0101
0.004	0.000322	0.003	0.00140	0.002	0.00120	0.003	0.00845
0.003	0.000262	0.002	0.000964	0.0016	0.000895	0.002	0.00658
0.002	0.000181	0.0016	0.000744	0.001	0.000349	0.0016	0.00441
0.0016	0.000139	0.001	0.000315	0.00071	0.0000656	0.001	0.00321
0.001	0.0000578	0.00071	0.0000724	0.00063	0.0000184	0.00071	0.00102
0.00071	0.0000103	0.00063	0.0000287			0.00063	0.000249
0.00063	0.0000026	0.0005	0.0000018			0.0005	0.000113
0.0005	8.95E-15					0.0004	0.0000067

## Appendix C: Regression analysis

Tables C.I and C.II list the regression data of the experiments given in Table-I of Paper IV given in Chapter 8, except for E4.

**Table C.I:** Regression analysis of experiments E1, E2 and E3

Fitting Region	Fine-fragments region	Intermediate size fragments region
Equation	$\ln(C_1) + \alpha \ln(s)$	$\ln(C_3) + \alpha \ln(s)$
Parameter		
<hr/> E1: 6 g/m <hr/>		
$\ln(C_1)$	5.67±0.40	-
$\ln(C_3)$	-	4.16 ± 0.43
$\alpha$	-1.695±0.021	-1.669±0.022
R-squared	0.9942	0.9977
Adj. R-squared	0.9922	0.9974
<hr/>		
<hr/> E1: 12 g/m <hr/>		
$\ln(C_1)$	6.64 ± 0.18	-
$\ln(C_3)$	-	4.88 ± 0.65
$\alpha$	-1.643 ± 0.033	-1.651 ± 0.042
R-squared	0.9988	0.9937
Adj. R-squared	0.9984	0.9930
<hr/>		
<hr/> E1: 20 g/m <hr/>		
$\ln(C_1)$	7.11 ± 0.39	-
$\ln(C_3)$	-	5.02 ± 0.62
$\alpha$	-1.711 ± 0.073	-1.630 ± 0.039
R-squared	0.9946	0.9937
Adj. R-squared	0.9927	0.9931
<hr/>		
<hr/> E2: 6 g/m <hr/>		
$\ln(C_1)$	5.18 ± 0.34	-
$\ln(C_3)$	-	4.11 ± 0.66
$\alpha$	-1.677 ± 0.065	-1.674 ± 0.038
R-squared	0.9956	0.9927
Adj. R-squared	0.9941	0.9922
<hr/>		
<hr/> E2: 12 g/m <hr/>		
$\ln(C_1)$	6.95 ± 0.22	-
$\ln(C_3)$	-	6.79 ± 0.27
$\alpha$	-1.659 ± 0.042	-1.727 ± 0.017
R-squared	0.9981	0.9989
Adj. R-squared	0.9975	0.9988
<hr/>		
<hr/> E2: 20 g/m <hr/>		
$\ln(C_1)$	7.85 ± 0.16	-
$\ln(C_3)$	-	6.38 ± 0.36
$\alpha$	-1.683 ± 0.0310	-1.654 ± 0.021
R-squared	0.9990	0.9975
Adj. R-squared	0.9987	0.9973

Continued on Next Page...

Table C.I – Continued

Fitting Region		Fine-fragments region	Intermediate size fragments region
Equation		$\ln(C_1) + \alpha \ln(s)$	$\ln(C_3) + \alpha \ln(s)$
Parameter			
E3: 3 g/m			
$\ln(C_1)$		$7.83 \pm 0.03$	-
$\ln(C_3)$		-	$5.88 \pm 0.42$
$\alpha$		$-1.759 \pm 0.012$	$-1.647 \pm 0.030$
R-squared		0.9999	0.9970
Adj. R-squared		0.9999	0.9966
E3: 5 g/m			
$\ln(C_1)$		$8.28 \pm 0.01$	-
$\ln(C_3)$		-	$6.34 \pm 0.51$
$\alpha$		$-1.707 \pm 0.006$	$-1.617 \pm 0.0335$
R-squared		0.9999	0.9953
Adj. R-squared		0.9999	0.9949
E3: 10 g/m			
$\ln(C_1)$		$9.35 \pm 0.07$	-
$\ln(C_3)$		-	$7.87 \pm 0.25$
$\alpha$		$-1.707 \pm 0.029$	$-1.644 \pm 0.0176$
R-squared		0.9997	0.9990
Adj. R-squared		0.9994	0.9989
E3: 20 g/m			
$\ln(C_1)$		$10.04 \pm 0.03$	-
$\ln(C_3)$		-	$9.16 \pm 0.18$
$\alpha$		$-1.652 \pm 0.014$	$-1.701 \pm 0.013$
R-squared		0.9999	0.9995
Adj. R-squared		0.9999	0.9994
E3: 40 g/m			
$\ln(C_1)$		$10.96 \pm 0.24$	-
$\ln(C_3)$		-	$10.92 \pm 0.24$
$\alpha$		$-1.713 \pm 0.075$	$-1.812 \pm 0.017$
R-squared		0.9962	0.9994
Adj. R-squared		0.9943	0.9993

Table C.II: Regression analysis of experiments E5, E6 and E7

Fitting Region		Fine-fragments region	Intermediate size fragments region
Equation		$\ln(C_1) + \alpha \ln(s)$	$\ln(C_3) + \alpha \ln(s)$
Parameter			
E5: 0.46 kg/m <sup>3</sup>			

Continued on Next Page...

Table C.II – Continued

Fitting Region	Fine-fragments region	Intermediate size fragments region
Equation	$\ln(C_1) + \alpha \ln(s)$	$\ln(C_3) + \alpha \ln(s)$
Parameter		
<hr/>		
$\ln(C_1)$	$6.81 \pm 0.19$	-
$\ln(C_3)$	-	$6.82 \pm 0.48$
$\alpha$	$-1.675 \pm 0.020$	$-1.785 \pm 0.0176$
R-squared	0.9999	0.9953
Adj. R-squared	0.9990	0.9994
<hr/>		
E5: 0.444 kg/m <sup>3</sup>		
$\ln(C_1)$	$6.80 \pm 0.19$	-
$\ln(C_3)$	-	$5.49 \pm 1.24$
$\alpha$	$-1.687 \pm 0.020$	$-1.742 \pm 0.045$
R-squared	0.9991	0.9966
Adj. R-squared	0.9989	0.9959
<hr/>		
E5: 0.431 kg/m <sup>3</sup>		
$\ln(C_1)$	$6.56 \pm 0.22$	-
$\ln(C_3)$	-	$6.78 \pm 0.60$
$\alpha$	$-1.661 \pm 0.024$	$-1.784 \pm 0.022$
R-squared	0.9987	0.9992
Adj. R-squared	0.9985	0.9991
<hr/>		
E5: 0.231 kg/m <sup>3</sup>		
$\ln(C_1)$	$5.61 \pm 0.20$	-
$\ln(C_3)$	-	$4.03 \pm 0.64$
$\alpha$	$-1.669 \pm 0.022$	$-1.703 \pm 0.023$
R-squared	0.9990	0.9991
Adj. R-squared	0.9988	0.9989
<hr/>		
E5: 0.218 kg/m <sup>3</sup>		
$\ln(C_1)$	$5.56 \pm 0.17$	-
$\ln(C_3)$	-	$3.69 \pm 0.76$
$\alpha$	$-1.689 \pm 0.0185$	$-1.691 \pm 0.028$
R-squared	0.9993	0.9987
Adj. R-squared	0.9992	0.9984
<hr/>		
E5: 0.22 kg/m <sup>3</sup>		
$\ln(C_1)$	$3.87 \pm 0.66$	-
$\ln(C_3)$	-	$5.77 \pm 0.16$
$\alpha$	$-1.663 \pm 0.027$	$-1.633 \pm 0.022$
R-squared	0.9987	0.9991
Adj. R-squared	0.9984	0.9990
<hr/>		
E6: 6 g/m		
$\ln(C_1)$	$0.093 \pm 0.19$	-
$\ln(C_3)$	-	$0.78 \pm 2.39$
$\alpha$	$-1.634 \pm 0.016$	$-1.693 \pm 0.082$
R-squared	0.9980	0.9793

Continued on Next Page...



Table C.II – Continued

Fitting Region	Fine-fragments region	Intermediate size fragments region
Equation		
Parameter	$\ln(C_1) + \alpha \ln(s)$	$\ln(C_3) + \alpha \ln(s)$
Adj. R-squared	0.9980	0.9770
E6: 12 g/m		
$\ln(C_1)$	$0.40 \pm 0.23$	-
$\ln(C_3)$	-	$1.62 \pm 0.31$
$\alpha$	$-1.765 \pm 0.069$	$-1.676 \pm 0.020$
R-squared	0.9940	0.9978
Adj. R-squared	0.9925	0.9976
E6: 20 g/m		
$\ln(C_1)$	$2.03 \pm 0.29$	-
$\ln(C_3)$	-	$2.07 \pm 2.45$
$\alpha$	$-1.671 \pm 0.020$	$-1.701 \pm 0.084$
R-squared	0.9978	0.9854
Adj. R-squared	0.9977	0.9830
E7: 6 g/m		
$\ln(C_1)$	$0.05 \pm 0.21$	-
$\ln(C_3)$	-	$-1.76 \pm 1.61$
$\alpha$	$-1.651 \pm 0.018$	$-1.619 \pm 0.053$
R-squared	0.9976	0.9863
Adj. R-squared	0.9975	0.9852
E7(bl24): 12 g/m		
$\ln(C_1)$	$1.95 \pm 0.15$	-
$\ln(C_3)$	-	$-0.07 \pm 0.61$
$\alpha$	$-1.653 \pm 0.013$	$-1.610 \pm 0.020$
R-squared	0.9987	0.9982
Adj. R-squared	0.9987	0.9981
E7(bl25): 12 g/m		
$\ln(C_1)$	$2.4156 \pm 0.15695$	-
$\ln(C_3)$	-	$3.51168 \pm 0.62946$
$\alpha$	$-1.668 \pm 0.014$	$-1.729 \pm 0.022$
R-squared	0.9987	0.9983
Adj. R-squared	0.9986	0.9981
E7: 20 g/m		
$\ln(C_1)$	$3.59 \pm 0.25$	-
$\ln(C_3)$	-	$2.04 \pm 0.69$
$\alpha$	$-1.695 \pm 0.021$	$-1.669 \pm 0.022$
R-squared	0.9969	0.9977
Adj. R-squared	0.9967	0.9975

## Appendix D: Statistical significance analysis

Tables D.I and D.II list the statistical significance analysis of the experiments given in Table-I of Paper IV given in Chapter 8, except for E4. Among all 24 data sets, two of them, i.e. E5 : 0.46 kg/m<sup>3</sup> and E5 : 0.431 kg/m<sup>3</sup>, do not have two parallel lines. However, the exponent of fine-fragments size distribution is  $-5/3$ .

**Table D.I:** Statistical significance analysis for experiments E1, E2 and E3

Test Parameter	Equation	
	Fine-fragments region $\ln(C_1) + \alpha \ln(s)$	Intermediate size fragments region $\ln(C_3) + \alpha \ln(s)$
E1: 6 g/m		
No. of data points	5	10
R	-0.997	-0.999
p(R)	1.90E-4	8.34E-12
Residual variance	F= 10.568	p(F)= 0.00371
Gradient	F= 0.377	p(F)= 0.552
Intercept	F= 6.550	p(F)= 0.0250
E1: 12 g/m		
No. of data points	5	13
R	-0.999	-0.997
p(R)	1.83E-05	1.92E-13
Residual variance	F= 1.525	p(F)= 0.404
Gradient	F= 0.215	p(F)= 0.650
Intercept	F= 23.796	p(F)= 0.000201
E1: 20 g/m		
No. of data points	5	12
R	-0.997	-0.997
p(R)	1.71E-4	2.17E-12
Residual variance	F= 3.400	0.062
Gradient	F= 0.656	0.433
Intercept	F= 6.470	0.023
E2: 6 g/m		
No. of data points	5	15
R	-0.998	-0.996
p(R)	1.25E-4	2.77E-15
Residual variance	F= 1.723	p(F)= 0.211
Gradient	F= 0.00125	p(F)= 0.972
Intercept	F= 5.221	p(F)= 0.0354
E2: 12 g/m		
No. of data points	5	13

Continued on Next Page...

Table D.I – Continued

Fitting Region		Fine-fragments region	Intermediate size fragments region
Equation		$\ln(C_1) + \alpha \ln(s)$	$\ln(C_3) + \alpha \ln(s)$
Parameter			
R		-0.999	-0.999
p(R)		3.50E-05	1.61E-17
Residual variance		F= 5.185	p(F)= 0.0178
Gradient		F= 2.826	p(F)= 0.115
Intercept		F= 11.447	p(F)= 0.00410
E2: 20 g/m			
No. of data points		5	18
R		-0.999	-0.999
p(R)		1.37E-05	3.05E-22
Residual variance		F= 1.151	p(F)= 0.522
Gradient		F= 0.555	p(F)= 0.465
Intercept		F= 21.473	p(F)= 0.00016
E3: 3 g/m			
No. of data points		3	11
R		-0.999	-0.999
p(R)		4.43E-3	1.23E-12
Residual variance		F= 92.996	p(F)= 0.080
Gradient		F= 0.942	p(F)= 0.355
Intercept		F= 16.420	p(F)= 0.00191
E3: 5 g/m			
No. of data points		3	13
R		-0.999	-0.998
p(R)		2.27E-3	3.65E-14
Residual variance		F= 672.673	p(F)= 0.030
Gradient		F= 0.345	p(F)= 0.568
Intercept		F= 11.247	p(F)= 0.00519
E3: 10 g/m			
No. of data points		3	11
R		-0.999	-0.999
p(R)		1.10E-2	9.43E-15
Residual variance		F= 5.535	p(F)= 0.319
Gradient		F= 0.859	p(F)= 0.376
Intercept		F= 29.344	p(F)= 0.000211
E3: 20 g/m			
No. of data points		3	10
R		-0.999	-0.999
p(R)		5.5E-3	1.63E-14

Continued on Next Page...

Table D.I – Continued

Fitting Region		Fine-fragments region	Intermediate size fragments region
Equation		$\ln(C_1) + \alpha \ln(s)$	$\ln(C_3) + \alpha \ln(s)$
Parameter			
Residual variance		F= 10.626	p(F)= 0.233
Gradient		F= 1.151	p(F)= 0.311
Intercept		F= 27.608	p(F)= 0.000371
E3: 40 g/m			
No. of data points		4	8
R		-0.998	-0.999
p(R)		1.92E-3	1.83E-12
Residual variance		F= 20.909	p(F)= 0.00198
Gradient		F= 2.737	p(F)= 0.137
Intercept		F= 5.215	p(F)= 0.0483

Table D.II: Statistical significance analysis for experiments E5, E6, and E7

Test		Fine-fragments region	Intermediate size fragments region
Equation		$\ln(C_1) + \alpha \ln(s)$	$\ln(C_3) + \alpha \ln(s)$
Parameter			
E5: 0.46 kg/m <sup>3</sup>			
No. of data points		8	7
R		-0.999	-0.999
p(R)		1.99E-10	1.78E-09
Residual variance		F= 1.987	p(F)= 0.234
Gradient		F= 15.164	p(F)= 0.00250
Intercept		F= 21.181	p(F)= 0.000608
E5: 0.444 kg/m <sup>3</sup>			
No. of data points		8	7
R		-0.999	-0.998
p(R)		2.03E-10	2.28E-07
Residual variance		F= 3.277	p(F)= 0.0903
Gradient		F= 1.439	p(F)= 0.255
Intercept		F= 21.451	p(F)= 0.000579
E5: 0.431 kg/m <sup>3</sup>			
No. of data points		8	7
R		-0.999	-0.999
p(R)		6.49E-10	5.51E-09
Residual variance		F= 1.846	p(F)= 0.259

Continued on Next Page...

Table D.II – Continued

Fitting Region	Fine-fragments region	Intermediate size fragments region
Equation	$\ln(C_1) + \alpha \ln(s)$	$\ln(C_3) + \alpha \ln(s)$
Parameter		
Gradient	F= 12.723	p(F)= 0.00442
Intercept	F= 16.079	p(F)= 0.00173
E5: 0.231 kg/m <sup>3</sup>		
No. of data points	8	7
R	-0.999	-0.999
p(R)	3.54E-10	9.19E-09
Residual variance	F= 1.36	p(F)= 0.38
Gradient	F= 1.033	p(F)= 0.331
Intercept	F= 38.112	p(F)= 4.774E-05
E5: 0.218 kg/m <sup>3</sup>		
No. of data points	8	7
R	-0.999	-0.999
p(R)	1.15E-10	2.27E-08
Residual variance	F=1.483	p(F)= 0.320
Gradient	F=0.0184	p(F)= 0.894
Intercept	F=33.476	p(F)= 8.663E-05
E5: 0.22 kg/m <sup>3</sup>		
No. of data points	7	7
R	-0.999	-0.999
p(R)	7.58E-09	2.10E-08
Residual variance	F= 1.543	p(F)= 0.323
Gradient	F= 0.772	p(F)= 0.400
Intercept	F= 43.888	p(F)= 3.736E-05
E6: 6 g/m		
No. of data points	22	12
R	-0.999	-0.991
p(R)	1.59E-28	3.86E-10
Residual variance	F= 1.012	p(F)= 0.516
Gradient	F= 0.577	p(F)= 0.453
Intercept	F= 7.562	p(F)= 0.00986
E6: 12 g/m		
No. of data points	16	8
R	-0.999	-0.999
p(R)	7.93E-20	1.83E-09
Residual variance	F= 9.422	p(F)= 0.00568
Gradient	F= 0.0529	p(F)= 0.820
Intercept	F= 19.083	p(F)= 0.000269

Continued on Next Page...

Table D.II – Continued

Fitting Region		Fine-fragments region	Intermediate size fragments region
Equation		$\ln(C_1) + \alpha \ln(s)$	$\ln(C_3) + \alpha \ln(s)$
Parameter			
E6: 20 g/m			
No. of data points		17	8
R		-0.999	-0.993
p(R)		2.39E-21	9.74E-07
Residual variance		F= 2.098	p(F)= 0.185
Gradient		F= 0.0694	p(F)= 0.795
Intercept		F= 5.646	p(F)= 0.0266
E7: 6 g/m			
No. of data points		22	15
R		-0.999	-0.993
p(R)		1.19E-27	1.73E-13
Residual variance		F= 1.216	p(F)= 0.366
Gradient		F= 0.300	p(F)= 0.587
Intercept		F= 5.367	p(F)= 0.0267
E7 (bl24): 12 g/m			
No. of data points		21	13
R		-0.999	-0.999
p(R)		1.55E-28	1.71E-16
Residual variance		F= 5.902	p(F)= 0.00222
Gradient		F= 0.546	p(F)= 0.466
Intercept		F= 16.477	p(F)= 0.00031
E7 (bl25): 12 g/m			
No. of data points		21	13
R		-0.999	-0.999
p(R)		7.10E-29	1.52E-16
Residual variance		F= 5.800	p(F)= 0.00240
Gradient		F= 1.849	p(F)= 0.184
Intercept		F= 5.651	p(F)= 0.0238
E7: 20 g/m			
No. of data points		23	17
R		-0.998	-0.999
p(R)		8.42E-28	1.09E-20
Residual variance		F= 6.818	p(F)= 0.000208
Gradient		F= 1.691	p(F)= 0.202
Intercept		F= 4.557	p(F)= 0.0395

This page intentionally left blank.

**Appendix E: Fine- and intermediate fragment size range**

Table E.I lists the fine- and the intermediate fragment size limits and the lower size limit of the boulders region of the experiments given in Table-I of Paper IV given in Chapter 8. Sandstone grain size 1/16 mm – 2 mm. Granite (quartz, K-feldspar, mica) with  $x_{50} = 1$  mm [99].



**Table E.1:** FSDs size limits of the fine-fragments, the intermediate size fragments and the boulders of the experiments given in Table-I of Paper IV

Test ID	Material	Charge density [g/m <sup>3</sup> ] [kg/m <sup>3</sup> ]	Minimum mesh size [mm]	Fine region lower limit [mm]	Fine region upper limit [mm]	Offset location [mm]	Intermediate size lower limit [mm]	Intermediate size upper limit [mm]	Lower limit of boulders [mm]	Max. sieve size [mm]	
E1	Mortar	6	0.04	$x_{min}$	1	0.5-2.0	2.0	20	50	125	
		12						20		125	
		20						40		100	
E2	Granite	6	0.04	$x_{min}$	1	0.5-2.0	2.0	50	50	125	
		12						50		80	
		20						80		100	
E3	MM <sup>1</sup>	3	0.063	$x_{min}$	0.25	0.25-0.5	0.5	45	45	90	
		5								90	
		10								63	
		20								63	
		40								45	
E4	MM	5	0.063	$x_{min}$	0.5	0.25-1	1	31.5	31.5	90	
		10								90	
		20								63	
		40								45	
E5	Sandstone	0.46	0.002	$x_{min}$	0.5	0.5-1.5875	1.5875	406.4	NIB	406.4	
		0.44									
		0.431									
		0.231									
		0.218									
0.22											
E6	Mortar	6	5E-4	$x_{min}$	0.5	0.5-2.0	1	31.5	50	125	
		12	4E-4							16	125
		20	5E-4							16	100
E7	Granite	6	5E-4	$x_{min}$	1	0.5-1	2	50	50	125	
		12 (bl24)	5E-4							40	100
		12 (bl25)	6.3E-4							50	80
		20	4E-4							80	100

<sup>a</sup>Magnetite mortar<sup>b</sup>No identified boulders.